Excited State Dynamics
in
Nanostructured Polymer Systems

Yasunari TAMAI

2013

Contents

Chapter 3

Dynamical Excimer Formation in Rigid Carbazolophane via Charge Transfer State

Chapter 4

Triplet Exciton Dynamics in Fluorene–Amine Copolymer Films

Part II

Chapter 5

Singlet Fission in Poly(9,9'-di-*n*-octylfluorene) Films

Chapter 6

Selective Observation of Singlet Exciton Diffusion in Poly(3-hexylthiophene) Crystalline Domains

Chapter 1

General Introduction

1.1. Historical Background and Motivation

Excited state properties and transport are the key to optoelectronic devices such as polymer solar cells[1–3] and polymer light-emitting diodes (PLEDs).[4,5] They are strongly dependent on interchromophore interactions and hence relative configuration of chromophores. On a molecular scale, the excited state properties are governed by the interchromophore interaction between neighboring chromophores. For example, when the distance between two identical chromophores is short enough to interact electronically, the excitation energy is delocalized over the two chromophores, resulting in the excimer (excited dimer) formation.[6–10] Thus, the excimer properties and formation dynamics vary with the relative configurations of chromophores. When two chromophoric groups are covalently linked with π conjugation, the excited state wavefunction is delocalized over the two chromophoric groups, resulting in the formation of a new chromophoric system whose optoelectronic properties would differ from those of each individual chromophoric group. Thus, optoelectronic properties of conjugated polymers can be easily tuned by copolymerization of different conjugation units. On a macroscopic scale, on the other hand, the excited state transport is strongly dependent on the structural regularity of the alignment of chromophores such as crystalline, β phase, and amorphous structures. In condensed chromophoric systems such as π-conjugated thin films, the excited state can diffuse freely as an exciton, which is a coulombically bound electron–hole pair. In amorphous films, excitons would diffuse randomly in all the directions with an isotropic diffusion coefficient because of random orientation of the chromophohres in the film. In ordered condensed systems such as crystalline films, on the other

hand, excitons would diffuse anisotropically in the film because of regular alignment of the chromophores. When the exciton concentration is enough high, an exciton can meet with another exciton during the exciton diffusion, resulting in exciton–exciton annihilation either in the singlet or triplet state. Thus, the dynamics of the singlet or triplet exciton–exciton annihilation is also governed by the film morphology. In polymer systems, such relative configuration of chromophores is dependent on polymer configurations, conformations, and higher order nanostructures formed by assembly of individual polymer chains such as microphase-separated structures and crystalline structures. In this thesis, therefore, the photophysical dynamics relating to the excited state properties and transport in nanostructured polymer systems is discussed in terms of the first, second, and higher order structures. The aim of this thesis is to study the relationship between macroscopic optoelectronic properties and microscopic polymer nanostructures and to provide molecular guideline for the creation of excellent optoelectronic functions.

In the first half of this thesis, the author focuses his attention on the interchromophore interaction on a molecular scale to discuss the relationship between the excited state properties and the first/second order structures. The excited state properties in polymers labeled with functional chromophores in the side chains such as poly(*N*-vinylcarbazole) (PVCz, **7** in Figure 1-1) is governed by relative configuration of neighboring chromophores. For PVCz, it has been reported that fully overlapped excimer and partially overlapped excimer are formed depending on the main chain configuration, conformation and motions.[11–17] In order to understand the relationship between the conformation and excimer formation dynamics in details, the properties and formation dynamics of excimers have been studied by using bischromophoric intramolecular model compounds such as cyclophanes. The excited state properties in conjugated polymers are different from those of vinyl aromatic polymers that are labeled with functional chromophores in the side chains, because the polymer backbone itself consists of covalently linked π conjugated chromophores. As a result of the main chain π conjugation, the excited state properties of conjugated polymers significantly depend on the polymer chain conformation: chemical structures, sequences, and molar fractions of the

chromophores. In other words, the excited properties of conjugated polymers can be easily modified by copolymerizing two or more different chromophoric units. In this thesis, the excited state properties in conjugated copolymers are studied in terms of the first and second order structures.

In the latter half of this thesis, the author focuses his attention on the interchromophore interaction on a macroscopic scale to discuss the relationship between the excited state transport and the higher order nanostructures. Because of the large interchain interaction, many conjugated polymers have been reported to form ordered structures in thin films. Poly(9,9'-di-*n*-octylfluorene) (PFO, **15**) forms β phase (β-PFO) in solid films, which is a characteristic phase of PFO, in which conjugated main chains are planarly extended and aligned.[18,19] Regioregular poly(3-hexylthiophene) (P3HT, **23**) self-organizes into two-dimensional π-stacked lamellar structures to form crystalline fibrils.[20–23] As a result, β-PFO and crystalline P3HT films exhibit a red-shifted absorption band and a high charge carrier mobility, and thus optoelectronic properties of PFO and P3HT films are strongly dependent on the film morphology. However, even fundamental excited state dynamics such as exciton diffusion is not fully understood for ordered conjugated polymer films. As a reverse process of the triplet–triplet annihilation (TTA), one singlet excited state would convert into two triplet excited state in the film state, which is called singlet fission. This multiple exciton generation has attracted increasing attention particularly in the field of polymer solar cells. However, the mechanism is still an open question. In this thesis, singlet exciton diffusion dynamics in crystalline P3HT films and multiple exciton generation from one photon via singlet fission in PFO films are studied in terms of the film morphology.

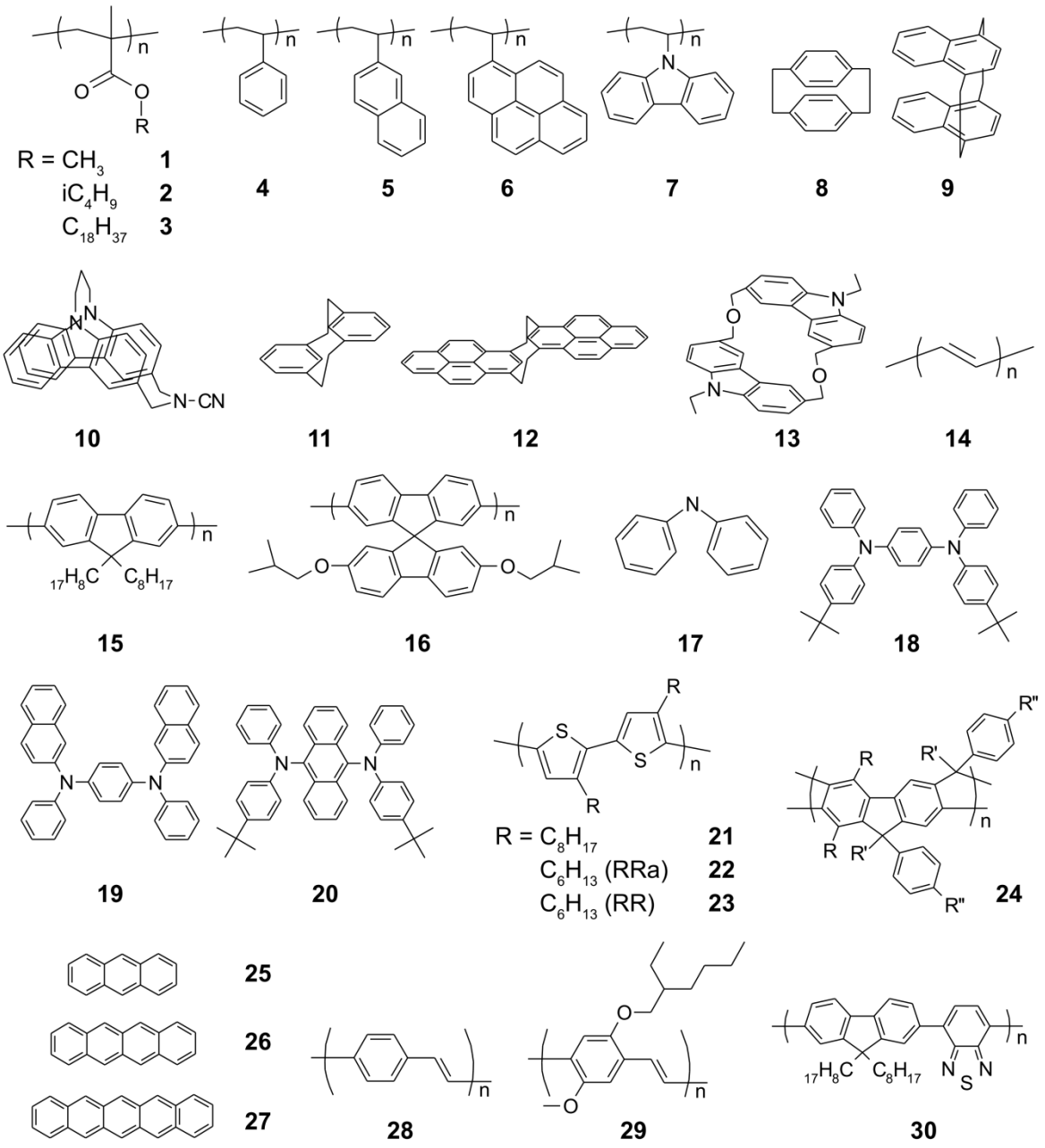

Figure 1-1. Chemical structures reviewed in this chapter.

1.1.1. Chain Conformation in Nanostructured Thin Films

A. Langmuir–Blodgett Film

Bottom-up chemistry has attracted much attention as a means of obtaining polymeric nanomaterials controlled with nanometer size scale. One of the ways for designing nanometric materials by bottom-up chemistry is the use of ultrathin polymer films. The multi-layered structure composed of extremely thin polymer films allows us to control the distance of separation, sequence of layers, and orientation of molecules with a precision of nanometer scale in the direction of the film thickness.[24–28] Furthermore, each layer can be modified with functional chromophores, and electrochemically active donors and acceptors.[29–32]

Langmuir–Blodgett (LB) technique is the most reliable method for controlling the film structures. This technique was already established by the pioneering work of Langmuir and Blodgett, and then refined as an advanced molecular technology by Kuhn et al. in the 1960s. Furthermore, polymeric LB films were developed by several research groups in the 1980s.[33–36] Using amphiphilic polymers such as poly(alkyl methacrylate)s (e.g. **1**–**3**), a stable monolayer is formed at the air/water interface under the balance of hydrophobic main chain and hydrophilic side chains. The monolayer can be transferred onto a solid substrate in a layer-by-layer fashion. Consequently, extremely thin polymer films can be built-up in the desired order and also with an arbitrary number of layers, by the easy operation under moderate conditions.

B. Polymer Chain in Restricted Dimensions

Conformation of a single polymer chain in the ultrathin film is one of the most important aspects to discuss the properties of polymeric monolayers. The film thickness of a single layer LB film is typically 1–2 nm,[28] which corresponds to the monomer size, indicating that an LB film has a thickness of only one molecule, and hence can be assumed to quasi two-dimensional (2D) systems. In the 2D system, two possible chain conformations are proposed as shown in Figure 1-2: (b) a

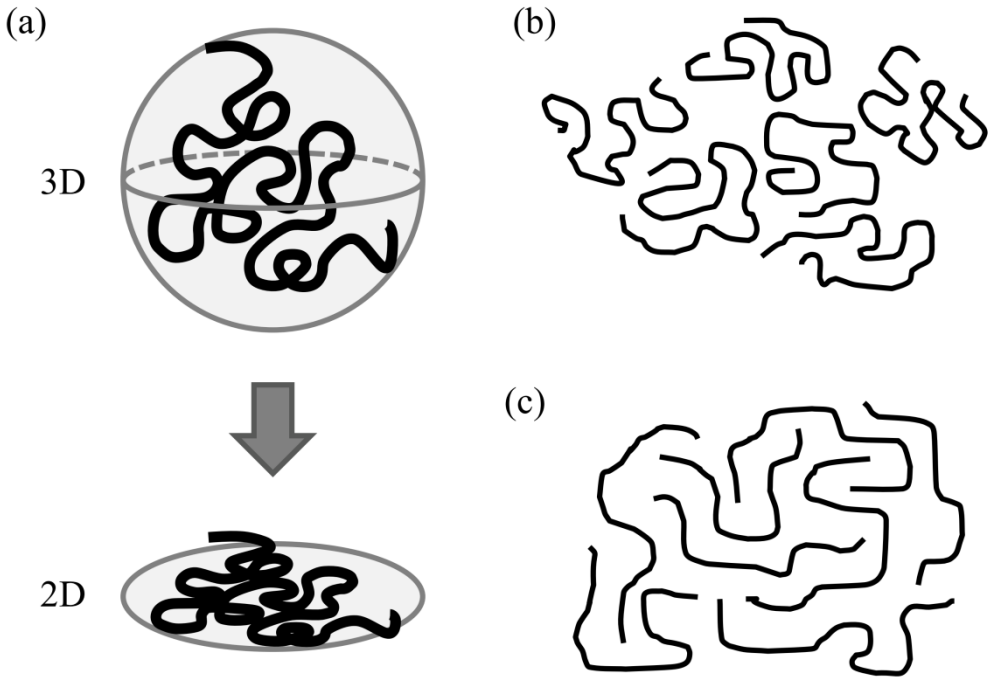

Figure 1-2. (a) Schematic illustration of chain conformation in two-dimensional (2D) monolayers: (b) segregated, and (c) interlaced model.

single chain is contracted and segregated each other, and (c) the chains are interlaced with each other and expanded.

A theoretical prediction for the chain conformation in the 2D system was provided by de Gennes with his scaling concept.[37] The volume occupied by the single polymer chain in the 3D melts is scaled as $\sim(N^{1/2}l)^3$ where N is the number of the segments and l is the segment length. Thus, the local concentration of a segment is $\sim((N^{1/2}l)^3/N)^{-1} = N^{-1/2}l^{-3}$, indicating that the polymer chains are overlapped each other to maintain a total concentration of $\sim l^{-3}$. On the other hand, in the 2D melts, the local concentration is $\sim((N^{1/2}l)^2/N)^{-1} = l^{-2}$, indicating that the local concentration of a segment is equivalent to the total concentration, and hence polymer chains are segregated each other (Figure 1-2a). However, no experimental evidence has been reported for the chain conformation in the 2D system determining whether a single chain is segregated or interlaced. Ito and his co-workers have studied this problem by using various experimental techniques such as surface viscosity measurement,[38] energy transfer method,[39] and microscopic methods.[40,41] Among them, one of the most reliable ways is a direct observation of single polymer chains by using high spatial resolution

microscopy. They performed a direct observation of single polymer chains by scanning near-field optical microscopy (SNOM), which is one of high spatial resolution optical microscopies based on fluorescence labeling technique.[40,41] In Ref. 41, single chains of poly(methyl methacrylate) (PMMA, **1**) labeled with dyes in non-labeled PMMA films was observed for different film thicknesses from the 3D thick film to the 2D LB film by SNOM with a spatial resolution of about 80 nm. As is discussed in Ref. 41, a radius of gyration of single polymer chains in the direction parallel to the film plane is not dependent on the film thickness, suggesting that single polymer chains are segregated in the 2D monolayer (Figure 1-2a).

C. Microphase Separation in Restricted Dimensions

Block copolymers consist of two or more homopolymer chains linked by covalent bonds.[42] The incompatibility between A and B segments in a block copolymer is dependent on the product of the Flory–Huggins interaction parameter χ and the degree of polymerization N. When the product χN is sufficiently large, the two segments segregate into A- and B-rich domains forming periodically ordered microstructures.[43–46] Depending on the volume fraction of each component, block copolymers self-assemble into various microphase-separated structures such as lamellae, cylinders, and spheres. Therefore, a lot of studies have been devoted to the bottom-up nanostructure formation by using microphase separation. Phase-separated structures in the 2D system also exhibit many interesting behaviors. Kumaki et al. observed the microphase-separated monolayer of poly(methyl methacrylate)-*block*-poly(octadecyl methacrylate) (PMMA-*b*-PODMA, **1**-*b*-**3**) by atomic force microscopy (AFM).[47] Interestingly, they found that the domain size of each segment is one order of magnitude larger than that expected from their molecular weights, and hence they concluded that polymer chains in the microphase-separated domains in the 2D system are highly elongated in the direction perpendicular to the domain interface and interlaced with neighboring chains. This finding is in contrast to the single chain conformation of homopolymers as mentioned above. As is discussed in Ref. 47, this unique chain elongation and interpenetration may be driven by repulsive

interaction between PMMA and PODMA domains and prohibition of chain overlapping because of no degree of freedom in the direction perpendicular to the film surface. The microphase-separated structures can be tuned by additionally blending homopolymers into the block copolymer. For 3D microphase-separated structures, the location and conformation of homopolymer chains blended additionally have been studied both theoretically[48,49] and experimentally.[50–57] However, there have been no investigations for the 2D system. This is an interesting issue whether a single homopolymer chain blended on 2D microphase-separated structures is segregated or interlaced. In this thesis, therefore, the author describes his direct observation of single homopolymer chains blended in 2D microphase-separated structures by using SNOM.

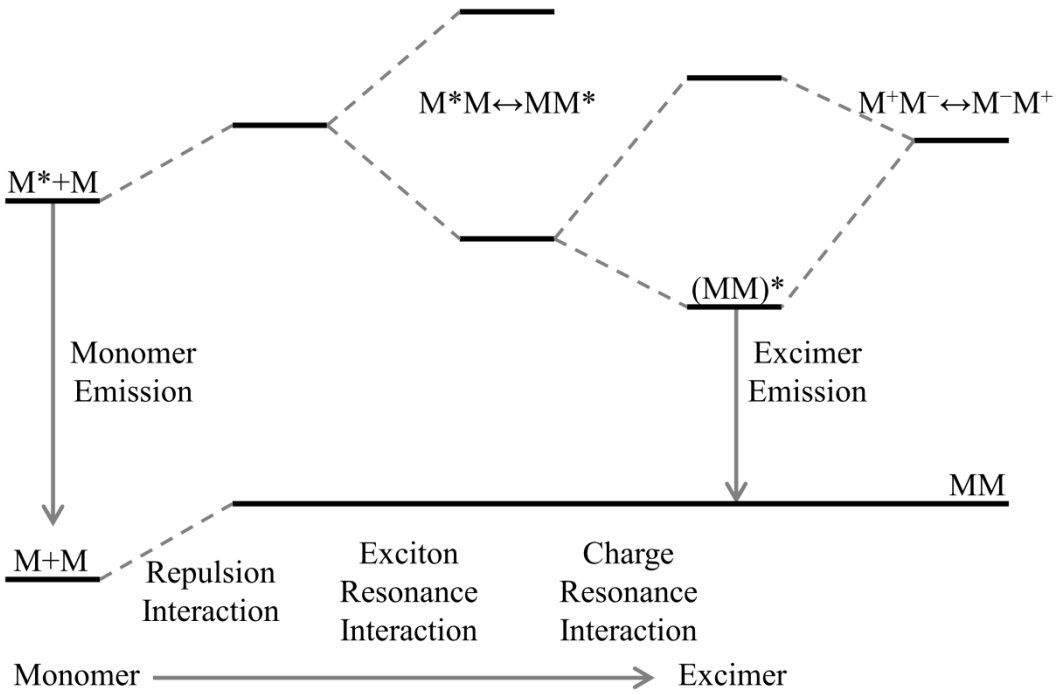

Figure 1-3. Schematic energy diagram of excimer formation in an aromatic molecule M. M* and (MM)* represent the monomer fluorescent state and the excimer fluorescent state, respectively. M*M ↔ MM* and M^+M^- ↔ M^-M^+ represent the exciton resonance state and the charge resonance state, respectively.

1.1.2. Interchromophore Interaction on Molecular Scale

A.1. Excimer

Since the first report of the pyrene excimer in solution by Förster and Kasper in 1954,[6] excimers have been studied by many researchers in the fields of photophysics and photochemistry.[7–10] Excimers are molecular dimers of two identical aromatic molecules, which are thermodynamically stable only in electronically excited states. Such complexes are formed in a reaction of one molecule in the excited state and the other in the ground state stabilized by two types of interactions as shown in Figure 1-3.[8,10,58–61] Primary excitation on one molecule (M* + M) is delocalized among two molecules and the energy level splits into two exciton states by exciton resonance interaction between two electronic configurations, M*M and MM*. Such a resonant excited state is further stabilized by charge resonance interaction between the excited state and a charge transfer (CT) state. Excimers can be formed when these stabilization energies exceed the repulsion energy between the

two chromophores. The most prominent feature of the excimer is a broad fluorescence band without a vibrational structure, which is red-shifted compared to that of the monomer fluorescence.

A.2. Intramolecular Excimer Formation in Polymer Systems

Intramolecular excimer has attracted much attention from the view point of the relationship between the molecular structure and the formation dynamics. Yanari et al. first reported intramolecular excimers in a study of the fluorescence spectra of polystyrene **4** in 1963.[62] Almost at the same time, Hirayama studied the fluorescence spectra of a variety of diphenyl and triphenyl alkanes in solution and found that intramolecular excimers can be formed only in those compounds in which two phenyl groups along a main alkyl chain are separated by the three carbon atoms (n = 3 rule).[63] Subsequent studies have shown that the n = 3 rule is widely applicable to other bischromophoric molecules,[64–68] indicating that vinyl aromatic polymers such as poly(vinylnaphtharene) **5**, poly(vinylpyrene) **6**, and poly(*N*-vinylcarbazole) (PVCz, **7**) always satisfy the configurational requirement for efficient excimer formation.[69–76]

Among vinyl aromatic compounds, PVCz has been extensively studied because it is one of the most sensitive photoconductive organic polymers.[77,78] Klöpffer first reported the intramolecular excimer of 1,3-bis(*N*-carbazolyl)propane as a model compound for PVCz, which exhibited the excimer fluorescence both in a dilute solution and in solid states.[65,66] Later, it was found that there are at least two types of excimers in PVCz: the fully overlapped excimer (sandwich excimer) and the partially overlapped excimer with only one eclipsed aromatic ring from two carbazolyl chromophores in the *tt* conformation of the syndiotactic sequence in PVCz.[11,12] However, it is difficult to study the intramolecular excimer formation in vinyl aromatic polymers. This is because vinyl aromatic polymers can take various conformations in either a solution or solid. In other words, macroscopic photophysical properties we can measure are just a statistical average of various configurations of aromatic rings. Therefore, bischromophoric dimer model compounds have been studied to clarify the relationship between the molecular structure and the formation dynamics. For

PVCz, extensive kinetic studies have been carried out to address the origin of the two kinds of excimer emissions by using various dimer model compounds.[11–17]

A.3. Cyclophane Chemistry

Cyclophanes are one of the most reliable molecules for studying the interchromophore interactions between two chromophoric groups not only in the ground state but also in the excited state, because they have a rigid structure where the relative configuration of two chromophoric groups is clearly defined.[79] In particular, various *syn*-cyclophanes (e.g. **8**–**10**) have been studied to examine excimer properties in terms of their structures.[80-93] Historically, the absorption spectra of [*m.n*]paracyclophanes **8** have been studied by Cram systematically.[80] The emission spectra of [*m.n*]paracyclophanes have been experimentally and theoretically studied by many researchers.[81–83] The photophysical properties of carbazole excimer have been studied various carbazole cyclophanes (carbazolophanes, e.g. **10**). On the other hand, *anti*-cyclophanes have a structure where two chromophores are bridged in anti-parallel orientation (e.g. **11**–**13**). Thus, the *anti*–*syn* isomerization in *anti*-cyclopahnes is difficult in the ground state because of the large activation energy.[94–99] There are only a few studies reporting intramolecular excimer formation in *anti*-cyclophanes.[96–98] From the view point of the relationship between the molecular structure and the excimer formation dynamics, the intramolecular excimer formation is more interesting in *anti*-cyclophanes than in *syn*-cyclophanes. In this thesis, therefore, the author performs a spectroscopic and theoretical analysis of the intramolecular excimer formation in a rigid *anti*-cyclophane by conformational flipping.

B.1. Excited States in Conjugated Polymers

Since the discovery of the conductive properties of doped polyacetylene **14** in 1977 by Shirakawa, Heeger, and MacDiarmid,[100] who were awarded the Nobel Prize in Chemistry in 2000, conjugated polymers have attracted much interest in both academic and industrial communities because of their potential to optoelectronic applications such as polymer solar cells,[1–3] PLEDs,[4,5] and field-effect transistors (FETs).[101,102] Owing to the extensive investigation over the past few decades, the device performance has been rapidly improved, and now is reaching that of inorganic devices. However, many basic questions for optoelectronic properties of conjugated polymers have still remained unclear.

Upon photoexcitation of conjugated polymers, an electron is excited from the highest occupied molecular orbital (HOMO) into the lowest unoccupied molecular orbital (LUMO).[103] This leads to the formation of a coulombically bound electron–hole pair, called "exciton", instead of free electron and hole carriers because of the small dielectric constant ($\varepsilon_r \approx 3$–4).[2,3] Considering electron spin, there are four eigenstates of the two electron system.[103–105] The full wavefunction is given by the product of a spatial and spin wavefunctions. The spin wavefunction with $S = 0$ has only a single possible value of z-component of the spin wavefunction, and hence termed as singlet state. On the other hand, other three spin wavefunctions with $S = 1$ only differ in the z-component of the spin wavefunction that has an eigenvalue of $M_s = 1, 0, -1$. These states are therefore termed as triplet state.

The energy levels of these states are identified as the summation of a zero order (one-electron orbital) energy plus electron repulsion energies

$$E_{1,3} = E(\psi_1) + E(\psi_2) + J(1,2) \pm K(1,2) \qquad (1\text{-}1)$$

where J and K are the coulomb and exchange integral, respectively.[104,105] The coulomb integral J increases the energy of both singlet and triplet states, while the exchange integral K increases the singlet energy and decreases the triplet energy. Therefore, the energy difference between the singlet and triplet state ΔE_{ST} is twice the exchange integral $2K$. In a first order approximation, the exchange

interaction scales exponentially with the overlap of the respective electron wavefunctions, which roughly corresponds to the overlap of the HOMO and LUMO.[104,105] For example, the ΔE_{ST} in conjugated polymers has been reported to be about 0.7 – 0.9 eV for amorphous conjugated polymers.[105] Because of the Pauli exclusion principle, singlet excitons are the primary photoexcitation in most cases. The lifetime of the lowest singlet excited state S_1 in conjugated polymers is typically ~ns. As summarized in Figure 1-4, singlet excitons deactivate to the ground state radiatively (fluorescence) or non-radiatively, or are converted into triplet excitons through intersystem crossing (ISC).

The radiative decay rate k_r of singlet excitons in conjugated polymers tends to be larger than that of small molecules. For example, k_r of polyfluorenes (e.g. **15, 16**) has been reported to be 0.5–2 × 10^9 s^{-1} depending on their side chain,[14] while that of the fluorene monomer is as small as 6.6 × 10^7 s^{-1}.[106] Such a large enhancement in k_r originates from delocalization of wavefunctions over polymer backbone. Whereas in small molecules the excited state wavefunction is localized at a single molecule, that of conjugated polymers is delocalized over several repeating units owing to the main chain π-conjugation, resulting in enhancement in oscillator strength. Conformational disorders in conjugated polymers have impact on the degree of delocalization and hence their optoelectronic properties. In general, conjugated polymers take coiled conformations except for some rigid polymers, because they have conformational freedom. As twisted segments in the backbone increase, effective conjugation length decreases.[107] When there are various twisted segments and kink sites along the backbone, the effective conjugation length is distributed inhomogeneously. In such an inhomogeneous polymer, the density of states (DOS) is widely distributed in energy.

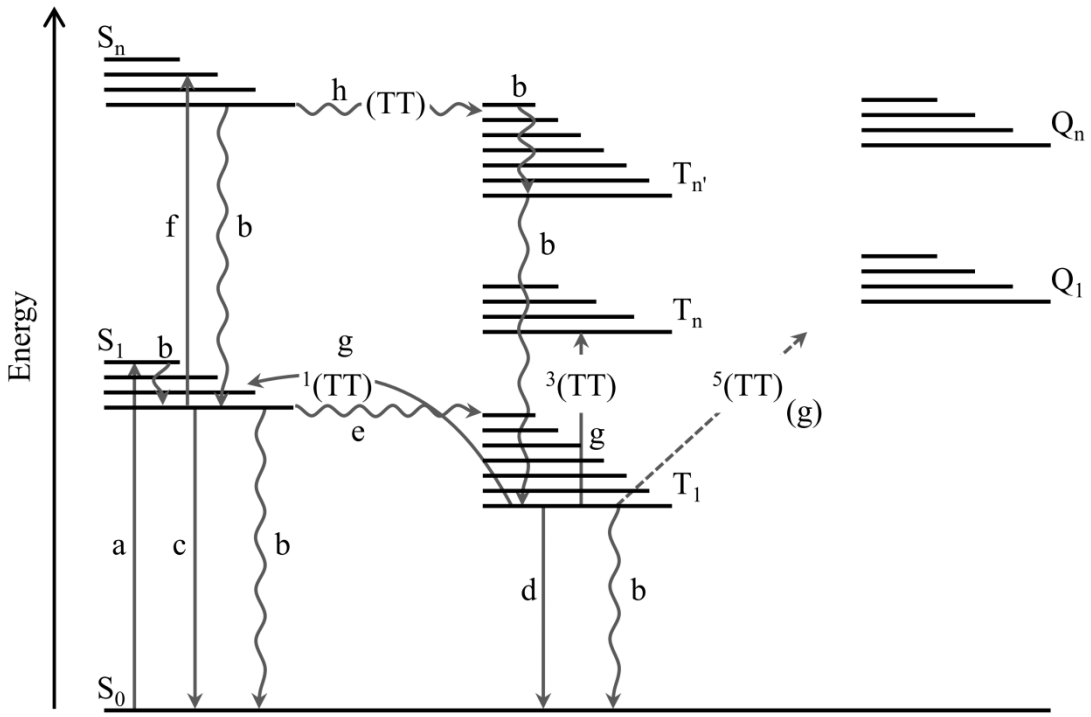

Figure 1-4. Expanded Jablonski diagram: (a) photon absorption, (b) vibrational relaxation, (c) fluorescence, (d) phosphorescence, (e) intersystem crossing (ISC), (f) singlet–singlet annihilation (SSA), (g) triplet–triplet annihilation (TTA), and (h) hot singlet fission. S, T, and Q represent singlet, triplet, and quintet states, respectively.

B.2. Triplet Exciton Generation through Intersystem Crossing

Triplet excitons cannot be formed directly after the photoexcitation, but can be generated through the ISC from singlet excitons.[104,105] The ISC rate depends on the strength of the spin–orbit coupling and the overlap between the vibrational wavefunctions of the S_1 and triplet states. The spin–orbit coupling plays an important role in the ISC because the sum of spin and orbital angular momentum should be conserved: a spin momentum change should be compensated by an orbital momentum change. In a *p* orbital, for example, a spin flip of an electron is accompanied by a change in the associated angular momentum from l_y to l_x. In other words, the strength of the spin–orbit coupling is significantly dependent on molecular conformation.[108–113] For example, the ISC rate increases significantly in going from a planar carbazole (3.7×10^7 s^{-1}) to a non-planar diphenylamine **17** (3.6

$\times 10^8$ s^{-1}) while the radiative decay rates remain almost the same ($3.0 – 4.4 \times 10^7$ s^{-1}). As a result, the ISC quantum efficiency increases from ~0.4 for the carbazole to ~0.9 for the diphenylamine.[108] The vibrational wavefunction overlap term depends exponentially on the energy difference between the two states, and hence the ISC is more efficient when the ΔE_{ST} is smaller. In Ref. 113, the phosphorescence intensity is compared between *N*,*N*'-bis(4-*n*-butylphenyl)-*N*,*N*'-diphenyl-1,4-benzenediamine (PDA, **18**) and *N*,*N*'-dinaphtyl-*N*,*N*'-diphenyl-1,4-benzenediamine (NNP, **19**): both molecules have twisted aromatic amine units and hence would have a large spin–orbit coupling. In a dilute frozen solution, phosphorescence is dominant for PDA while strong fluorescence is observed for NNP. This is attributed to the difference in ΔE_{ST}; 0.4 eV for PDA and 0.7 eV for NNP.

Unfortunately, little is known about the ISC in conjugated polymers.[114–120] A direct observation of the ISC in a conjugated polymer was first reported by Heeger et al. in 1995.[114] They performed subpicosecond transient absorption measurement for poly(3-octylthiophene) (P3OT, **21**), and found that the ISC rate k_{ISC} is 8.3×10^8 s^{-1} for P3OT. According to their estimation, the quantum efficiency of the ISC Φ_{ISC} was estimated to be ~0.4 for P3OT. As is discussed in Ref. 114, the efficient ISC in P3OT is attributed to heavy atom effect of sulfur atom in the thiophene ring. In contrast, King et al. evaluated k_{ISC} to be 5.6×10^6 s^{-1} for polyspirofluorene **16** in a dilute solution.[117] From a fluorescence lifetime of 2.3 ns, the Φ_{ISC} is estimated to be as small as ~0.01. Such a small k_{ISC} value is attributable to the small spin–orbit coupling because of π–π* transition nature in both the lowest singlet and triplet excited states and the absence of heavy atoms. Furthermore, an even smaller Φ_{ISC} has been reported to be only 0.002 for fully planar methyl substituted poly(*p*-phenylene) (MeLPPP, **24**).[118] Brédas et al. pointed out the importance of twisting of conjugated chains for the ISC in their theoretical studies.[111] However, the limited experimental studies reported previously are insufficient to provide an unambiguous conclusion.

1.1.3. Interchromophore Interaction on Macroscopic Scale

A. Triplet Exciton Generation through Singlet Fission

Singlet fission is another way to generate triplet excitons in solid films. In this process, one singlet excited state delocalized over neighboring two chromophore units is converted into two triplet excited states as shown in Figure 1-5.[103,121] The overall reaction from singlet to triplet exciton in the singlet fission is spin-conserving and thus spin-allowed, therefore triplet formation through the singlet fission proceeds even in the femto- to picosecond time domain.

$$S^* + S_0 \rightarrow T_1 + T_1 \qquad (1\text{-}2)$$

Singlet fission was first proposed in 1965 to explain the excited state dynamics in anthracene **25** crystals,[122] and then has been observed in various materials, especially in molecular crystals such as larger polyacenes (tetracene, **26**; pentacene, **27**).[121,123–130] For efficient singlet fission, the energy level of the lowest singlet excited state should be higher than twice the lowest triplet excited state energy $E(S_1) > 2E(T_1)$. Among many molecular crystals, tetracene and pentacene crystals have been widely investigated both experimentally and theoretically because of their significantly high fission efficiency reaching nearly 100%. For pentacene crystals, the energetic requirement for efficient singlet fission ($E(S_1) \geq 2E(T_1)$) is satisfied because of a low $E(S_1)$ (~1.83 eV) and a large ΔE_{ST} (~0.97 eV). Indeed, ultrafast singlet fission into two triplets is observed on a time scale of ~80 fs, which is independent of the excitation wavelength.[124] For tetracene crystals, singlet fission is thermally activated because $E(S_1)$ is slightly lower than $2E(T_1)$. At room temperature, the singlet fission takes place on a time scale of ~50 ps from relaxed singlet state even though it takes place on a time scale of ~0.3 ps from hot singlet state.[124]

Singlet fission is possible even in conjugated polymer films, but only limited reports have been published so far.[131–138] The triplet yield action spectra of MeLPPP and poly(*p*-phenylene vinylene) (PPV, **28**) have been measured.[135–137] Upon the photoexcitation at long wavelengths, triplet excitons are only formed by the ISC. Upon the photoexcitation at short wavelengths, additional triplet photogeneration is observed at an onset of 3.2 eV for MeLPPP and 3.1 eV for PPV, both of which

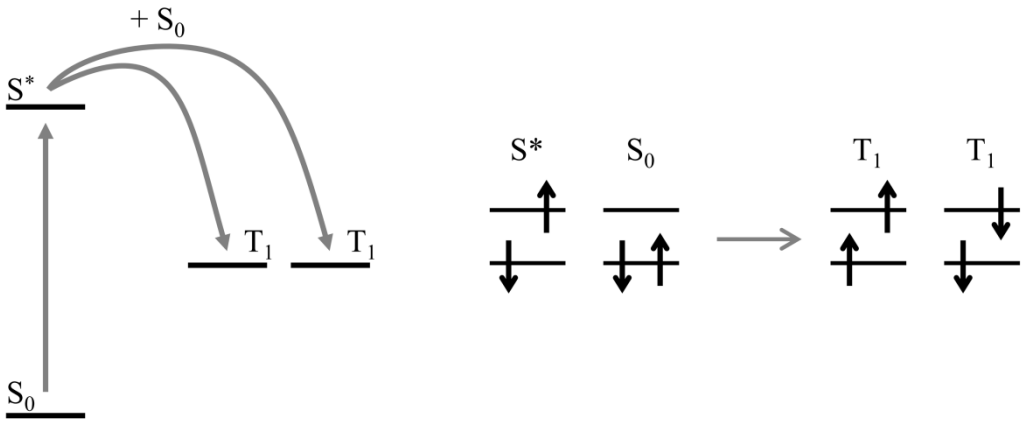

Figure 1-5. Schematic illustration of the singlet fission. The overall reaction from singlet excited state (left) to two triplet excitons (right) is spin-conserving.

correspond to twice the triplet energy $E(T_1)$ of 1.6 eV for MeLPPP and 1.55 eV for PPV. Thus, this additional triplet photogeneation is attributed to singlet fission from a higher singlet excited state before the vibrational relaxation. A clear morphology dependence of singlet fission has been reported for poly(3-hexylthiophene) (P3HT) films previously.[138] Guo et al. observed singlet fission in regiorandom poly(3-hexylthiophene) (RRa-P3HT, **22**) amorphous film by using transient absorption spectroscopy. In RRa-P3HT, $2E(T_1)$ is slightly higher than $E(S_1)$, and hence triplet excitons are only formed through the singlet fission from a higher singlet excited state produced by singlet–singlet annihilation (SSA). Interestingly, no triplet excitons are observed in regioregular P3HT (RR-P3HT **23**) crystalline films.[138] This is in sharp contrast with small molecules, in which the singlet fission is usually more efficient in molecular crystals rather than in less ordered films.[139,140] The absence of singlet fission in RR-P3HT crystalline films is attributed to preference polaron pair formation because of the large interchain interaction in π-stacked crystalline domains. On the other hand, both singlet fission and polaron pair formation have been reported for MeLPPP.[135,136,141] However, the limited data reported so far are insufficient to understand the relationship between the film morphology and the efficiency of the singlet fission in conjugated polymers, and hence further investigations have been desired.

B.1. Exciton Diffusion

Excitons can diffuse as a bound electron–hole pair before they deactivate to the ground state. Exciton diffusion can be considered to be a series of energy migration among identical chromophores. The rate for the energy migration can be derived from the time-dependent perturbation theory and the Fermi golden rule as follows.

$$k_{\mathrm{DA}} = \frac{2\pi}{\hbar}|V_{\mathrm{DA}}|^2 \mathrm{FCWD} \qquad (1\text{-}3)$$

where V_{DA} is the electronic coupling matrix element for the energy migration and FCWD stands for the Franck–Condon weighted density of states factor, which corresponds to the product of the density of vibrational states in the initial and final states and their spectral overlap. The energy migration takes place on the basis of Förster or Dexter mechanisms as summarized in Figure 1-6.[103,104,142]

The Förster mechanism (Figure 1-6a) is a resonance energy transfer mediated by long-range dipole–dipole interaction between donor and acceptor. In this model, the electronic coupling matrix element V_{DA} is dependent on the oscillator strength of related transition for both donor and acceptor, indicating that the Förster mechanism is much more important for singlet exciton diffusion rather than triplet exciton diffusion because of the spin-forbidden transition between the ground and triplet states.

The Dexter mechanism (Figure 1-6b) is known as an energy transfer based on electron exchange. Since the Dexter energy transfer is based on quantum mechanical exchange interactions, it requires spatial overlap of the donor and acceptor wavefunctions. Thus, the separation distance between neighboring chromophores has a critical impact on the diffusion coefficient. The absence of the oscillator strength term indicates that the Dexter energy transfer is important for the triplet exciton diffusion. The Dexter energy transfer occurs only when the donor and acceptor are close enough; the Dexter energy transfer rate immediately becomes slow with increasing separation between the donor and acceptor. This indicates that the diffusion coefficient of singlet excitons is usually larger than that of triplet excitons.

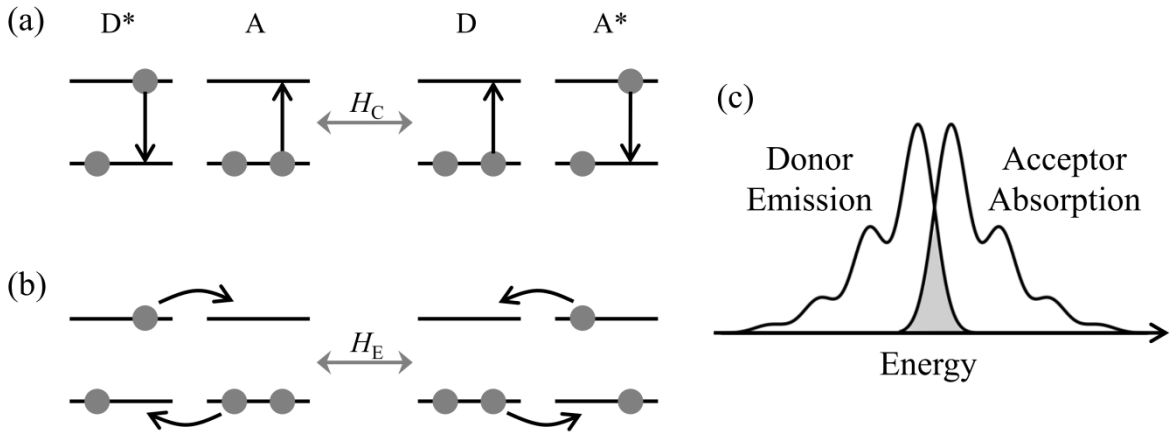

Figure 1-6. Schematic illustration of (a) Förster, and (b) Dexter energy transfer. Efficiency of the energy transfer is dependent on both coupling strength between the initial and final states (H_C and H_E) and spectral overlap between donor emission and acceptor absorption spectra (c).

Singlet exciton diffusion plays a central role in the photocurrent conversion in polymer solar cells. Therefore, the exciton diffusion length is one of the most important photophysical properties of organic films. Singlet exciton dynamics has been studied for many organic molecular crystals,[103,143–152] but is not fully understood for conjugated polymers, in particular, crystalline polymers. For example, there is not much difference in the diffusion length of singlet exciton reported for side-chain derivatives of PPV **29** amorphous films, which is typically as small as 5–7 nm.[153–158] In contrast, there is a significant difference in the diffusion length of singlet exciton reported for RR-P3HT crystalline films (2.6–27 nm).[159–163] This large difference is probably because that previous studies paid less attention to semicrystalline nature of RR-P3HT films. In crystalline polymer films like RR-P3HT, there should be crystalline and disordered amorphous domains at the same time. This is in sharp contrast with molecular single crystals, in which no disordered amorphous domains are involved. Therefore, the in-depth understanding of the singlet exciton dynamics in crystalline domains of RR-P3HT is desired.

Triplet exciton diffusion plays a central role in the improvement in the PLEDs efficiency. The most remarkable point of the triplet exciton diffusion is its potential for longer diffusion length than

that of singlet excitons. Owing to their long lifetime, triplet exciton diffusion length in some molecular crystals reaches up to μm order,[164,165] even though the diffusion coefficient is smaller than that of singlet excitons. For polymer systems, Friend et al. reported that the triplet exciton diffusion length of poly(9,9'-dioctylfluorene-*co*-benzothiadiazole) (F8BT, **30**) is as large as ~180 nm and triplet excitons contribute to the improvement in the PLEDs efficiency.[166] Unexpectedly, few values have been measured for the triplet exciton diffusion length in conjugated polymers. In this thesis, therefore, the author reports his measurements of the triplet exciton diffusion length and discusses the relevance of the triplet exciton diffusion dynamics to the PLEDs efficiency.

B.2. Exciton–Exciton Annihilation

The diffusion dynamics of excitons can be discussed by analyzing "exciton–exciton annihilation". At a high exciton density, an exciton can meet with another exciton during the exciton diffusion. As summarized in Figure 1-7, one exciton loses its energy while the other obtains the sum of the energy of the initial two excited states.[103] As a result, singlet–singlet annihilation (SSA) produces one higher singlet excited state S_n from two the lowest singlet excited states (arrow f in Figure 1-4).

$$S_1 + S_1 \rightarrow S_n + S_0 \rightarrow S_1 + S_0 + phonon \qquad (1\text{-}4)$$

The higher singlet excited state formed after the annihilation usually converts its excess energy to multi phonons, and relaxes to the lowest vibrational level in the lowest singlet excited state (arrow b in Figure 1-4). Therefore one singlet exciton is lost in SSA. Note that the higher singlet excited state occasionally takes place some photophysical reactions such as the singlet fission before the vibrational relaxation (arrow h in Figure 1-4).

$$S_1 + S_1 \rightarrow S_n + S_0 \rightarrow T_1 + T_1 + phonon \qquad (1\text{-}5)$$

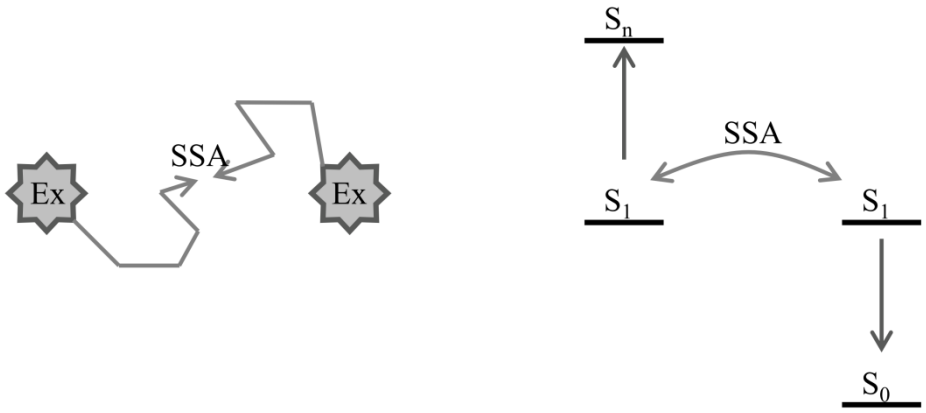

Figure 1-7. Schematic illustration and energy diagram of SSA. When an exciton can meet with another exciton during the exciton diffusion, one exciton loses its energy while the other obtains the sum of the energy of the initial two excited states.

TTA is slightly more complicated than SSA. Since triplet excited state is degenerated in three spin states, triplet exciton collision produces nine possible intermediate pair states: one singlet state ^{1}(TT), three triplet states ^{3}(TT), and five quintet states ^{5}(TT).[103,105,121] Since the quintet states are usually energetically inaccessible, it dissociates into two triplet excitons. Therefore, TTA only arises from the singlet and triplet pair states. It should be noted that TTA produces not only the higher triplet excited state but also the higher singlet excited state. The singlet excitons formed via TTA can emit fluorescence, which is called delayed fluorescence because the delayed fluorescence is limited by TTA slow dynamics, and hence is much slower than the prompt fluorescence because of the long lifetime of triplet excitons.

$$T_1 + T_1 \rightarrow \begin{cases} \overset{1/9}{\rightarrow} & {}^1(TT) \rightarrow S_n + S_0 \rightarrow S_1 + S_0 + \text{phonon} \\ \overset{3/9}{\rightarrow} & {}^3(TT) \rightarrow T_n + S_0 \rightarrow T_1 + S_0 + \text{phonon} \\ \overset{5/9}{\rightarrow} & {}^5(TT) \rightarrow T_1 + T_1 \end{cases} \quad (1\text{-}6)$$

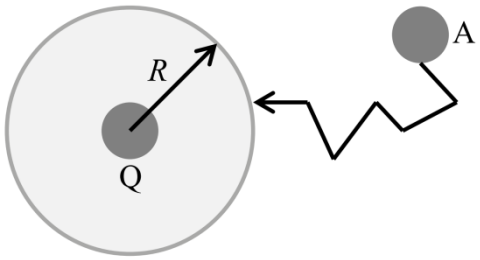

Figure 1-8. The flux through a spherical surface of a molecule A on its approach to an immobile quencher Q. Reaction occurs when the molecule A is at a distance *R*.

The exciton–exciton annihilation in conjugated polymers is usually diffusion-limited process. Therefore, the diffusion coefficient of excitons can be evaluated by analyzing the rate of the exciton–exciton annihilation. Here, the author briefly sketches the derivation of the annihilation rate. The derivation is based on the related issue of particle capture by an immobile quenching center as schematically shown in Figure 1-8.[167] Here, the author describes only the 3D isotropic diffusion model. Assuming a quencher shape as a sphere with an interaction radius *R*, and an initially uniform exciton density N_0, the diffusion problem around the quenching sphere of a single trap can be exactly solved to give the exciton flux into the trap. The number of excitons passing through the surface of the sphere in the unit time is given by

$$-4\pi R^2 J_r(R,t) = 4\pi R^2 D \left|\frac{\partial N(r,t)}{\partial r}\right|_{r=R} \tag{1-7}$$

where J_r is a radial component of flux vector, and $N(r,t)$ is the number density of excitons N at position r and time t. In the 3D isotropic diffusion model, the number density of excitons $N(r,t)$ is given by Eq. 1-8

$$N(r,t) = N_0\left[1 - \frac{R}{r}\,\mathrm{erfc}\left(\frac{r-R}{\sqrt{4Dt}}\right)\right] \tag{1-8}$$

where "erfc" denotes the complementary error function, which is defined as $\mathrm{erfc}(t) = \frac{2}{\sqrt{\pi}}\int_x^\infty \exp(-x^2)\,\mathrm{d}x$. Therefore, the reaction rate is given by

$$\gamma(t) = \frac{4\pi R^2 D}{N_0}\left|\frac{\partial N(r,t)}{\partial x}\right|_{r=R} = 4\pi DR\left(1 + \frac{R}{\sqrt{\pi Dt}}\right) \tag{1-9}$$

Taking into account that quenchers in the exciton–exciton annihilation are also mobile excitons, the diffusion coefficient should be replaced by an effective diffusion coefficient $D_{\mathrm{eff}} = D + D$, resulting in Eq. 1-10.

$$\gamma(t) = 8\pi DR\left(1 + \frac{R}{\sqrt{2\pi Dt}}\right) \qquad (1\text{-}10)$$

For a late time stage after $t >> R^2/(2\pi D)$, the annihilation rate can be expressed as the time-independent formula $\gamma_{3\mathrm{D}} = 8\pi DR$ because the second term in Eq. 1-10 is negligible. Therefore, the diffusion coefficient D is obtained from the annihilation rate $\gamma(t)$.

1.2. Outline of This Thesis

The aim of this thesis is to discuss photophysical dynamics in the excited state in nanostructured polymer systems from the view point of the first, second, and higher order nanostructures of polymer materials, and the relationship between macroscopic optoelectronic properties and microscopic polymer nanostructures. This thesis consists of six chapters. The first chapter describes the historical background and motivation of each chapter. The following chapters are divided into two parts.

In Part I (Chapter 2–4), the author focuses his attention on the interchromophore interaction on a molecular scale to discuss the relationship between the excited state properties and the first/second order structures.

In Chapter 2, the author focuses his attention on the chain conformation in ultrathin polymer films before moving on discussing photophysics in polymer systems. The conformation of a single poly(isobutyl methacrylate) (PiBMA, **2**) chain dispersed in microphase-separated structure of poly(isobutyl methacrylate)-*block*-poly(octadecyl methacrylate) (PiBMA-*b*-PODMA, **2**-*b*-**3**) monolayer is studied by SNOM. The location and orientation of single PiBMA chains are discussed on the basis of quantitative fluorescence image analysis.

In Chapter 3, solvent-polarity-induced formation dynamics of intramolecular excimer in dioxa[3.3](3,6)carbazolophane (CzOCz **13**) is studied by time-resolved spectroscopic methods and

computational calculations. As mentioned above, the *anti–syn* isomerization is very difficult in the ground state in CzOCz, but CzOCz exhibited a clear excimer emission in polar solvents. The solvent-polarity-induced excimer formation is discussed in terms of the conformation of CzOCz.

In Chapter 4, triplet exciton dynamics is studied for two conjugated copolymers of fluorene with aromatic amines, poly(9,9'-di-*n*-octylfluorene-*ran*-*N*,*N*'-bis(4-*n*-butylphenyl)-*N*,*N*'-diphenyl-1,4-benzenediamine) (F8-PDA, **15**-*ran*-**18**) and poly(9,9'-di-*n*-octylfluorene-*ran*-*N*,*N*'-bis(4-*t*-butylphenyl)-*N*,*N*'-diphenyl-9,10-anthracenediamine) (F8-ADA, **15**-*ran*-**20**) by transient absorption spectroscopy. The ISC efficiency is discussed in terms of planarity of the chain conformation and energy difference between singlet and triplet excited states. The triplet exciton diffusion efficiency is discussed in terms of the energy level arraignment of triplet excited state of the fluorene and aromatic amines.

In Part II (Chapter 5, 6), the author focuses his attention on the interchromophore interaction on a macroscopic scale to discuss the relationship between the excited state transport and the higher order nanostructures.

In Chapter 5, the dynamics of singlet fission in poly(9,9'-di-*n*-octylfluorene) (PFO, **15**) films is studied by transient absorption spectroscopy. Under a high excitation intensity, triplet excitons are rapidly interconverted from singlet excitons on a picosecond time stage. From the excitation intensity dependence of the generation yield, the rapid triplet excitons formation in PFO films is attributed to singlet fission from a higher singlet excited state S_n formed by the singlet exciton–exciton annihilation (singlet fusion). The dependence of the film morphology on the singlet fission efficiency is discussed in terms of interchain interaction.

In Chapter 6, singlet exciton dynamics in crystalline domains of RR-P3HT films is observed by transient absorption spectroscopy. The exciton diffusion coefficient is evaluated from the singlet exciton–exciton annihilation rate. The diffusion parameters evaluated are compared with the literature values reported previously. The origin of the time-dependent exciton dynamics is discussed in terms of dimensionality.

References

(1) Dennler, G.; Scharber, M. C.; Brabec, C. J. *Adv. Mater.* **2009**, *21*, 1323–1338.

(2) Kippelen, B.; Brédas, J.-L. *Energy Environ. Sci.* **2009**, *2*, 251–261.

(3) Deibel, C.; Dyakonov, V. *Rep. Prog. Phys.* **2010**, *73*, 096401.

(4) Friend, R. H.; Gymer, R. W.; Holmes, A. B.; Burroughes, J. H.; Marks, R. N.; Taliani, C.; Bradley, D. D. C.; Dos Santos, D. A.; Brédas, J. L.; Lögdlund, M.; Salanech, W. R. *Nature* **1999**, *397*, 121–128.

(5) So, F.; Kido, J.; Burrows, P. *MRS Bull.* **2008**, *33*, 663–669.

(6) Förster, T.; Kasper, K. *Z. Phys. Chem. NF* **1954**, *1*, 275–277.

(7) Förster, T. *Angew. Chem. Int. Ed.* **1969**, *8*, 333–343.

(8) Birks, J. B. *Photophysics of Aromatic Molecules*; Wiley-Interscience: London, 1970; Chapter 7.

(9) Klöpffer, W. In *Organic Molecular Photophysics*; Birks, J. B., Ed.; Wiley-Interscience: New York, 1973; Chapter 9.

(10) Birks J. B. *Rep. Prog. Phys*. **1975**, *38*, 903–974.

(11) Johnson, G. E. *J. Phys. Chem.* **1975**, *62*, 4697–4709.

(12) Itaya, A.; Okamoto, K.; Kusabayashi, S. *Bull. Chem. Soc. Jpn.* **1976**, *49*, 2082.

(13) De Schryver, F. C.; Vandendriessche, J.; Toppet, S.; Demeyer, K.; Boens, N. *Macromolecules* **1982**, *15*, 406−408.

(14) Evers, F.; Kobs, K.; Memming, R.; Terrell, D. R. *J. Am. Chem. Soc.* **1983**, *105*, 5988−5995.

(15) Vandendriessche, J.; Palmans, P.; Toppet, S.; Boens, N.; De Schryver, F. C.; Masuhara, H. *J. Am. Chem. Soc.* **1984**, *106*, 8057−8064.

(16) De Schryver, F. C.; Collart, P.; Vandendriessche, J.; Goedeweeck, R.; Swinnen, A.; Van der Auweraer, M. *Acc. Chem. Res.* **1987**, *20*, 159−166.

(17) Ito, S.; Takami, K.; Tsujii, Y.; Yamamoto, M. *Macromolecules* **1990**, *23*, 2666−2673.

(18) Monkman, A.; Rothe, C.; King, S.; Dias, F. *Adv. Polym. Sci.* **2008**, *212*, 187–225.

(19) Knaapila, M.; Winokur, M. J. *Adv. Polym. Sci.* **2008**, *212*, 227–272.

(20) Grévin, B.; Rannou, R.; Payerne, R.; Pron, A.; Travers, J. P. *J. Chem. Phys.* **2003**, *118*, 7097–7102.

(21) Kim, Y.; Cook, S.; Tuladhar, S. M.; Choulis, S. A.; Nelson, J.; Durrant, J. R.; Bradley, D. D. C.; Giles, M.; Mcculloch, I.; Ha, C.-S.; Ree, M. *Nat. Mater.* **2006**, *5*, 197–203.

(22) Lim, J. A.; Liu, F.; Ferdous, S.; Muthukumar, M.; Briseno, A. L. *Mater. Today* **2010**, *13*, 14–24.

(23) Salleo, A.; Kline, R. J.; DeLongchamp, D. M.; Chabinyc, M. L. *Adv. Mater.* **2010**, *22*, 3812–3838.

(24) Ringsdorf, H.; Schmidt, G.; Schneider, J. *Thin Solid Films* **1987**, *152*, 207–222.

(25) Tredgold, R. H. *Thin Solid Films* **1987**, *152*, 223–230.

(26) Wegner, G. *Thin Solid Films* **1992**, *216*, 105–116.

(27) Miyashita, T. *Prog. Polym. Sci.* **1993**, *18*, 263–294.

(28) Ito, S.; Mabuchi, M.; Sato, N.; Aoki, H. *Bull. Chem. Soc. Jpn.* **2005**, *78*, 371–382.

(29) Ito, S.; Okubo, H.; Ohmori, S.;Yamamoto, M. *Thin Solid Films* **1989**, *179*, 445–449.

(30) Ohmori, S.; Ito, S.; Yamamoto, M. *Macromolecules* **1990**, *23*, 4047–4053.

(31) Ito, S.; Ohmori, S.; Yamamoto, M. *Macromolecules* **1992**, *25*, 185–191.

(32) Ohkita, H.; Ogi, T.; Kinoshita, R.; Ito, S.; Yamamoto, M. *Polymer* **2002**, *43*, 3571–3577.

(33) Mumby, S. J.; Swalen, J. D.; Rabolt, J. F. *Macromolecules* **1986**, *19*, 1054–1059.

(34) Watanabe, M.; Kosaka, Y.; Oguchi, K.; Sanui, K.; Ogata, N. *Macromolecules* **1988**, *21*, 2997–3003.

(35) Naito, K. *J. Colloid Interface Sci.* **1989**, *131*, 218–225.

(36) Brinkhuis, R. H. G.; Schouten, A. J. *Macromolecules* **1991**, *24*, 1487–1495.

(37) de Gennes, P. G. *Scaling Concepts in Polymer Physics*; Cornell University: Ithaca, N.Y., 1979.

(38) Sato, N.; Ito, S.; Yamamoto, M. *Macromolecules* **1998**, *31*, 2673–2675.

(39) Sato, N.; Osawa, Y.; Ito, S.; Yamamoto, M. *Polym. J.* **1999**, *31*, 488–493.

(40) Aoki, H.; Anryu, M.; Ito, S. *Polymer* **2005**, *46*, 5896–5902.

(41) Aoki, H.; Morita, S.; Sekine, R.; Ito, S. *Polym. J.* **2008**, *40*, 274–280.

(42) Hadjichristidis, N.; Pitsikais, M.; Iatrou, H. *Adv. Polym. Sci.* **2005**, *189*, 1–124.

(43) Leibler, L. *Macromolecules* **1980**, *13*, 1602–1617.

(44) Bates, F. S.; Fredricson, G. H. *Annu. Rev. Phys. Chem.* **1990**, *41*, 525–557.

(45) Matsen, M. W. *J. Phys.: Condens. Matter* **2002**, *14*, R21–R47.

(46) Abetz, V.; Simon, P. F. *Adv. Polym. Sci.* **2005**, *189*, 125–212.

(47) Kumaki, J.; Hashimoto, T. *J. Am. Chem. Sci.* **1998**, *120*, 423–424.

(48) Shull, K. R.; Winey, K. I. *Macromolecules* **1992**, *25*, 2637–2644.

(49) Vavasour, J. D.; Whitemore, M. D. *Macromolecules* **2001**, *34*, 3471–3483.

(50) Winey, K. I.; Thomas, E. L.; Fetters, L. J. *Macromolecules* **1992**, *25*, 2645–2650.

(51) Matsushita, Y.; Torikai, N.; Mogi, Y.; Noda, I.; Han, C. C. *Macromolecules* **1993**, *26*, 6346–6349.

(52) Koizumi, S.; Hasegawa, H.; Hashimoto, T. *Macromolecules* **1994**, *27*, 7893–7906.

(53) Matsushita, Y.; Torikai, N.; Mogi, Y.; Noda, I.; Han, C. C. *Macromolecules* **1994**, *27*, 4313–4569.

(54) Orso, K. A.; Green, P. F. *Macromolecules* **1999**, *32*, 1087–1092.

(55) Mayes, A. M.; Russell, T. P.; Satija, S. K.; Majkrzak, C. F. *Macromolecules* **1992**, *25*, 6523–6531.

(56) Shull, K. R.; Mayes, A. M.; Russell, T. P. *Macromolecules* **1993**, *26*, 3929–3936.

(57) Yang, J.; Sekine, R.; Aoki, H.; Ito, S. *Macromolecules* **2007**, *40*, 7573–7580.

(58) Azumi, T.; Armstrong, A. T.; McGlynn, S. P. *J. Chem. Phys.* **1964**, *41*, 3839–33852.

(59) Katoh, R.; Sinha, S.; Murata, S.; Tachiya, M. *J. Photochem. Photobiol. A* **2001**, *145*, 23–34.

(60) Amicangelo, J. C. *J. Phys. Chem. A* **2005**, *109*, 9174–39182.

(61) Shirai, S.; Iwata, S.; Tani, T.; Inagaki, S. *J. Phys. Chem. A* **2011**, *115*, 7687–7699.

(62) Yanari, S. S.; Bovey, F. A.; Lumry, R. *Nature* **1963**, *200*, 242–244.

(63) Hirayama, F. *J. Chem. Phys.* **1965**, *42*, 3163–3171.

(64) Chandross, E. A.; Dempster, C. J. *J. Am. Chem. Soc.* **1970**, *92*, 3586−3593.

(65) Klöpffer, W. *Chem. Phys. Lett.* **1969**, *4*, 193−194.

(66) Klöpffer, W. *J. Chem. Phys.* **1969**, *50*, 2337−2343.

(67) Ito, S.; Yamamoto, M.; Nishijima, Y. *Bull. Chem. Soc. Jpn.* **1981**, *54*, 35−40.

(68) Ito, S.; Yamamoto, M.; Nishijima, Y. *Bull. Chem. Soc. Jpn.* **1982**, *55*, 363−368.

(69) David, C.; Demarteau, W.; Geuskens, G. *Eur. Polym. J.* **1969**, *6*, 1397−1403.

(70) David, C.; Piens, M.; Geuskens, G. *Eur. Polym. J.* **1972**, *8*, 1019−1031.

(71) Yokoyama, M.; Tamamura, T.; Nakano, T.; Mikawa, H. *Chem. Lett.* **1972**, 499−502.

(72) Fox, R. B.; Price, T. R.; Cozzens, R. F.; McDonald, J. R. *J. Chem. Phys.* **1972**, *57*, 534−541.

(73) McDonald, J. R.; Echols, W. E.; Price, T. R.; Fox, R. B. *J. Chem. Phys.* **1972**, *57*, 1746−1752.

(74) Johnson, G. E.; Offen, H. W. *J. Chem. Phys.* **1971**, *55*, 2945–2949.

(75) Harrah, L. A. *J. Chem. Phys.* **1972**, *56*, 385−389.

(76) Yokoyama, M.; Tamamura, T.; Atsumi, M.; Yoshimura, M.; Shirota, Y.; Mikawa, H. *Macromolecules* **1975**, *8*, 101−104.

(77) Hoegl, H. *J. Phys. Chem.* **1965**, *69*, 755−766.

(78) Pearson, J. M.; Stolka, M. *Poly*(*N-vinylcarbazole*); Gordon and Breach: New York, 1981.

(79) Cram, D. J.; Cram, J. M. *Acc. Chem. Res.* **1971**, *4*, 204–213.

(80) Cram, D. J.; Allinger, N. L.; Steinberg, H. *J. Am. Chem. Soc.* **1954**, *76*, 6132–6141.

(81) Vala, M. T.; Hillier, I. H.; Rice, S. A.; Jortner, J. *J. Chem. Phys.* **1966**, *44*, 23–35.

(82) Hillier, I. H.; Glass, L.; Rice, S. A. *J. Chem. Phys.* **1966**, *45*, 3015–3021.

(83) Longworth, J. L.; Bovey, F. A. *Biopolymers* **1966**, *4*, 1115–1129.

(84) Froines, J. R.; Hagerman, P. J. *Chem. Phys. Lett.* **1969**, *4*, 135–138.

(85) Yanagidate, M.; Takayama, K.; Takeuchi, M.; Nishimura, J.; Shizuka, H. *J. Phys. Chem.* **1993**, *97*, 8881–8888.

(86) Morita, M.; Kishi, T.; Tanaka, M.; Tanaka, J.; Ferguson, J.; Sakata, Y.; Misumi, S.; Hayashi, T.; Mataga, N. *Bull. Chem. Soc. Jpn.* **1978**, *51*, 3449–3457.

(87) Nakamura, Y.; Tsuihiji, T.; Mita, T.; Minowa, T.; Tobita, S.; Shizuka, H.; Nishimura, J. *J. Am. Chem. Soc.* **1996**, *118*, 1006–1012.

(88) Nakamura, Y.; Kaneko, M.; Yamanaka, N.; Tani, K.; Nishimura, J. *Tetrahedron Lett.* **1999**, *40*, 4693–4696.

(89) Tani, K.; Tohda, Y.; Takemura, H.; Ohkita, H.; Ito, S.; Yamamoto, M. *Chem. Commun.* **2001**, 1914–1915.

(90) Ohkita, H.; Ito, S.; Yamamoto, M.; Tohda, Y.; Tani, K. *J. Phys. Chem. A* **2002**, *106*, 2140–2145.

(91) Benten, H.; Ohkita, H.; Ito, S.; Yamamoto, M.; Sakumoto, N.; Hori, K.; Tohda, Y.; Tani, K.; Nakamura, Y.; Nishimura, J. *J. Phys. Chem. B* **2005**, *109*, 19681–19687.

(92) Benten, H.; Guo, J.; Ohkita, H.; Ito, S.; Yamamoto, M.; Sakumoto, N.; Hori, K.; Tohda, Y.; Tani, K. *J. Phys. Chem. B* **2007**, *111*, 10905–10914.

(93) Tani, K.; Sakumoto, N.; Kubono, K.; Hori, K.; Tohda, Y.; Benten, H.; Ohkita, H.; Ito, S.; Yamamoto, M. *Chem. Lett.* **2009**, 140–141.

(94) Griffin Jr., R. W.; Coburn, R. A. *J. Am. Chem. Soc.* **1967**, *89*, 4638–4641.

(95) Sorimachi, K.; Morita, T.; Shizuka, H. *Bull. Chem. Soc. Jpn.* **1974**, *47*, 987–990.

(96) Shizuka, H.; Ogiwara, T.; Morita, T. *Bull. Chem. Soc. Jpn.* **1975**, *48*, 3385–3386.

(97) Hayashi, T.; Mataga, N.; Sakata, Y.; Misumi, S. *Chem. Phys. Lett.* **1976**, *41*, 325–328.

(98) Hayashi, T.; Mataga, N.; Umemoto, T.; Sakata, Y.; Misumi, S. *J. Phys. Chem.* **1977**, *81*, 424–429.

(99) Tani, K.; Tohda, Y.; Hisada, K.; Yamamoto, M. *Chem. Lett.* **1996**, 145–146.

(100) Chiang, C. K.; Fincher, C. R., Jr.; Park, Y. W.; Heeger, A. J.; Shirakawa, H.; Louis, E. J.; Gau, S. C.; MacDiarmid, A. G. *Phys. Rev. Lett.* **1977**, *39*, 1098–1101.

(101) Chabinyc, M. L.; Jimison, L. H.; Rivnay, J.; Salleo, A. *MRS Bull.* **2008**, *33*, 683–689.

(102) Braga, D.; Horowitz, G. *Adv. Mater.* **2009**, *21*, 1473–1486.

(103) Pope, M.; Swenberg, C. E. *Electronic Processes in Organic Crystals and Polymers*; Oxford University Press: Oxford, U.K., 1999.

(104) Turro, N. J. *Modern Molecular Photochemistry*; University Science Books: Sausalito, CA, 1978.

(105) Köhler, A.; Bässler, H. *Mater. Sci. Eng. R* **2009**, *66*, 71–109.

(106) Murov, S. L. *Handbook of Photochemistry*; Marcel Dekker, Inc.: N.Y., 1973.

(107) Scholes, G. D.; Rumbles, G. *Nat. Mater.* **2006**, *5*, 683–696.

(108) Adams, J. E.; Mantulin, W. W.; Huber, J. R. *J. Am. Chem. Soc.* **1973**, *95*, 5477–5481.

(109) Haink, H. J.; Huber, J. R. *Chem. Phys. Lett.* **1976**, *44*, 117–120.

(110) Sarkar, A.; Chakravorti, S. *J. Lumin.* **1998**, *78*, 205–211.

(111) Beljonne, D.; Shuai, Z.; Pourtois, G.; Brédas, J. L. *J. Phys. Chem. A* **2001**, *105*, 3899–3907.

(112) Scmidt, K.; Brovelli, S.; Coropceanu, V.; Beljonne, D.; Cornil, J.; Bazzini, C.; Caronna, T.; Tubino, R.; Meinardi, F.; Shuai, Z.; Brédas, J. L. *J. Phys. Chem. A* **2007**, *111*, 10490–10499.

(113) Wu, C.; Djurovich, P. I.; Thompson, M. E. *Adv. Funct. Mater.* **2009**, *19*, 3157–3164.

(114) Kraabel, B.; Moses, D.; Heeger, A. J. *J. Chem. Phys.* **1995**, *103*, 5102–5108.

(115) Burrows, H. D.; de Melo, J. S.; Serpa, C.; Arnaut, L. G.; Monkman, A. P.; Hamblett, I.; Navaratnam, S. *J. Chem. Phys.* **2001**, *115*, 9601–9606.

(116) Huang, Y.-F.; Chen, H.-L.; Ting, J. W.; Liao, C.-S.; Larsen, R. W.; Fann, W. *J. Phys. Chem. B* **2004**, *108*, 9619–9622.

(117) King, S.; Rothe, C.; Monkman, A. *J. Chem. Phys.* **2004**, *121*, 10803.

(118) Piok, T.; Gadermaier, C.; Wenzl, F. P.; Patil, S.; Montenegro, R.; Landfester, K.; Lanzani, G.; Cerullo, G.; Scherf, U.; List, E. J. W. *Chem. Phys. Lett.* **2004**, *389*, 7–13.

(119) King, S. M.; Matheson, R.; Dias, F. B.; Monkman, A. P. *J. Phys. Chem B* **2008**, *112*, 8010–8016.

(120) Petrozza, A.; Fazzi, D.; Avilov, I.; Beljonne, D.; Friend, R. H.; Kim, J.-S. *J. Phys. Chem C* **2012**, *116*, 11298–11305.

(121) Smith, M. B.; Michl, J. *Chem. Rev.* **2010**, *110*, 6891–6936.

(122) Singh, S.; Jones, W. J.; Siebrand, W.; Stoicheff, B. P.;Schneider, W. G. *J. Chem. Phys.* **1965**, *42*, 330–342.

(123) Thorsmølle, V. K.; Averitt, R. D.; Demsar, J.; Smith, D. L.; Tretiak, S.; Martin, R. L.; Chi, X.; Crone, B. K.; Ramirez, A. P.; Taylor, A. J. *Phys. Rev. Lett.* **2009**, *102*, 017401.

(124) Johnson, J. C.; Nozik, A. J.; Michl, J. *J. Am. Chem. Soc.* **2010**, *132*, 16302–16303.

(125) Burdett, J. J.; Müller, A. M.; Gosztola, D.; Bardeen, C. J. *J. Chem. Phys.* **2010**, *133*, 144506.

(126) Rao, A.; Wilson, M. W. B.; Albert-Seifried, S.; Di Pietro, R.; Friend, R. H. *Phys. Rev. B* **2011**, *84*, 195411.

(127) Burdett, J. J.; Gosztila, D.; Bardeen, C. J. *J. Chem. Phys.* **2011**, *135*, 214508.

(128) Wilson, M. W. B.; Rao, A.; Clark, J.; Kumar, R. S. S.; Brida, D.; Cerullo, G.; Friend, R. H. *J. Am. Chem. Soc.* **2011**, *133*, 11830–11833.

(129) Zimmerman, P. M.; Bell, F.; Casanova, D.; Head-Gordon, M. *J. Am. Chem. Soc.* **2011**, *133*, 19944–19952.

(130) Ma, L.; Zhang, K.; Kloc, C.; Sun, H.; Michel-Beyerle, M. E.; Gurzadyan, G. G. *Phys. Chem. Chem. Phys.* **2012**, *14*, 8307–8312.

(131) Austin, R. H.; Barker, G. L.; Etemad, S.; Thompson, R. *J. Chem. Phys.* **1989**, *90*, 6642–6646.

(132) Kraabel, B.; Hulin, D.; Aslangul, C.; Lapersonne-Meyer, C.; Schott, M. *Chem. Phys.* **1998**, *227*, 83–98.

(133) Lanzani, G.; Stagira, S.; Cerullo, G.; De Silvertri, S.; Comoretto, D.; Moggio, I.; Cuniberti, C.; Musso, G. F.; Dellepiane, G. *Chem. Phys. Lett.* **1999**, *313*, 525–532.

(134) Lanzani, G.; Cerullo, G.; Zavelani-Rossi, M.; De Silvestri, S. *Phys. Rev. Lett.* **2001**, *87*, 187402.

(135) Wohlgenannt, M.; Graupner, W.; Österbacka, R.; Leising, G.; Comoretto, D.; Vardeny, Z. V. *Synth. Met.* **1999**, *101*, 267–268.

(136) Wohlgenannt, M.; Graupner, W.; Leising, G.; Vardeny, Z. V. *Phys. Rev. B* **1999**, *60*, 5321–5330.

(137) Österbacka, R.; Wohlgenannt, M.; Shkunov, M.; Chinn, D.; Vardeny, Z. V. *J. Chem. Phys.* **2003**, *118*, 8905–8916.

(138) Guo, J.; Ohkita, H.; Benten, H.; Ito, S. *J. Am. Chem. Soc.* **2009**, *131*, 16869–16880.

(139) Marciniak, H.; Fiebig, M.; Huth, M.; Schiefer, S.; Nickel, B.; Selmaier, F.; Lochbrunner, S. *Phys. Rev. Lett.* **2007**, *99*, 176402.

(140) Marciniak, H.; Pugliesi, I.; Nickel, B.; Lochbrunner, S. *Phys. Rev. B* **2009**, *79*, 235318.

(141) Gulbinas, V.; Zaushitsyn, Y.; Bässler, H.; Yartsev, A.; Sundström, V. *Phys. Rev. B* **2004**, *70*, 035215

(142) Laquai, F.; Park, Y.-S.; Kim, J.-J.; Basché, T. *Macromol. Rapid Commum.* **2009**, *30*, 1203–1231.

(143) Powell, R. C.; Soos, Z. D. *J. Lumin.* **1975**, *11*, 1–45.

(144) Gulbinas, V.; Chachisvilis, M.; Valkunas, L.; Sundström, V. *J. Phys. Chem.* **1996**, *100*, 2213–2219.

(145) Donker, H.; van Hoek, A.; van Schaik, W.; Koehorst, R. B. M.; Yatskou, M. M.; Schaafsma, T. J. *J. Phys. Chem. B* **2005**, *109*, 17038–17046.

(146) Mani, A.; Schoonman, J.; Goossens, A. *J. Phys. Chem. B* **2005**, *109*, 4829–4836.

(147) Engel, E.; Leo, K.; Hoffmann, M. *Chem. Phys.* **2006**, *325*, 170–177.

(148) Kurrle, D.; Pflaum, J. *Appl. Phys. Lett.* **2008**, *92*, 133306.

(149) Huijser, A.; Savenije, T. J.; Meskers, S. C. J.; Vermeulen, M. J. W.; Siebbeles, L. D. A. *J. Am. Chem. Soc.* **2008**, *130*, 12496–12500.

(150) Yago, T.; Tamaki, Y.; Furube, A.; Katoh, R. *Phys. Chem. Chem. Phys.* **2008**, *10*, 4435–4441.

(151) Lunt, R. R.; Benziger, J. B.; Forrest, S. R. *Adv. Mater.* **2010**, *22*, 1233–1236.

(152) Marciniak, H.; Li, X.-Q.; Würthner, F.; Lochbrunner, S. *J. Phys. Chem. A* **2011**, *115*, 648–654.

(153) Markov, D. E.; Hummelen, J. C.; Blom, P. W. M. *Phys. Rev. B* **2005**, *72*, 045216.

(154) Markov, D. E.; Blom, P. W. M. *Phys. Rev. B* **2005**, *72*, 161401.

(155) Markov, D. E.; Blom, P. W. M. *Phys. Rev. B* **2006**, *74*, 085206.

(156) Scully, S. R.; McGehee, M. D. *J. Appl. Phys.* **2006**, *100*, 034907.

(157) Lewis, A. J.; Ruseckas, A.; Gaudin, O. P. M.; Webster, G. R.; Burn, P. L.; Samuel, I. D. W. *Org. Electron.* **2006**, *7*, 452–456.

(158) Mikhnenko, O. V.; Cordella, F.; Sieval, A. B.; Hummelen, J. C.; Blom, P. W. M.; Loi, M. A. *J. Phys. Chem. B* **2008**, *112*, 11601–11604.

(159) Kroeze, J. E.; Savenije, T. J.; Vermeulen, M. J. W.; Warman, J. M. *J. Phys. Chem. B* **2003**, *107*, 7696–7705.

(160) Goh, C.; Scully, S. R.; McGehee, M. D. *J. Appl. Phys.* **2007**, *101*, 114503.

(161) Huijser, A.; Savenije, T. J.; Shalav, A.; Siebbeles, L. D. A. *J. Appl. Phys.* **2008**, *104*, 034505.

(162) Shaw, P. E.; Ruseckas, A.; Samuel, I. D. W. *Adv. Mater.* **2008**, *20*, 3516–3520.

(163) Cook, S.; Liyuan, H.; Furube, A.; Katoh, R. *J. Phys. Chem. C* **2010**, *114*, 10962–10968.

(164) Najafov, H.; Lee, B.; Zhou, Q.; Feldman, L. C.; Podzorov, V. *Nat. Mater.* **2010**, *9*, 938–943.

(165) Silva, C. *Nat. Mater.* **2010**, *9*, 884–885.

(166) Wallikewitz, B. H.; Kabra, D.; Gélinas, S.; Friend, R. H. *Phys. Rev. B* **2012**, *85*, 045209.

(167) Chandrasekhar, S. *Rev. Mod. Phys.* **1943**, *15*, 1–89.

Part I

Chapter 2

Conformation of Single Homopolymer Chain in Microphase-Separated Block Copolymer Monolayer Studied by Scanning Near-Field Optical Microscopy

2.1. Introduction

Block copolymers are known to form microphase-separated structures such as lamellae, cylinders, and spheres.[1] Studies have been conducted on the variation of morphology with the composition,[2] the molecular weight dependence of domain size,[3–5] and the conformation of a block copolymer chain.[6,7] In the microphase-separated structures, the conformation of the block chain is distorted anisotropically: the block chain is elongated in the direction perpendicular to the interface between the two microdomains, whereas it shrinks in a parallel direction. The mixed system of the block copolymer and the corresponding homopolymers has been gathering interest. When a homopolymer A dissolves in a block copolymer A-*b*-B, the homopolymer is confined to the A domain formed by A-*b*-B. The location and conformation of the homopolymer chain in the block copolymer lamella have been extensively studied both theoretically[8,9] and experimentally.[10–18] Hasegawa et al. investigated the single chain conformation of a polystyrene homopolymer dissolved in a lamellar microdomain of polystyrene-*b*-polyisoprene diblock copolymer in bulk by small-angle neutron scattering (SANS).[13] They found that the homopolymer chains with molecular weights one order of magnitude smaller than that of the block copolymer are extended and contracted in the perpendicular and parallel directions, respectively, like the block chain. On the other hand, Matsushita et al. investigated polystyrene homopolymers with various molecular weights in polystyrene-*b*-poly(2-

vinylpyridine) in bulk by SANS.[16] Although the radii of gyration of the homopolymers in the direction perpendicular to the interface could not be evaluated due to the experimental difficulty, they found that the homopolymer chains are unperturbed at least in the direction parallel to the interface.

The behavior of the block copolymer in restricted dimensions (e.g., thin films and colloidal particles) differs from that of the bulk system.[18–22] Because the polymer chain in a monolayer is restricted in quasi two-dimensions,[23–26] the monolayer of diblock copolymer can be regarded as a good model system to study the phase separation in a restricted geometry. Previous studies indicated that the polymer chain restricted in such a quasi two-dimensional plane is not allowed to entangle with the intra- and intermolecular chains and forced to take a contracted conformation.[27–29] Therefore, the phase separation behavior in the two-dimensional system show anomalous features.[21–24,30,31] For example, because the polymer chain has no degree of freedom in the height direction and is not allowed to have cross-over on the other chains, the block chain in microphase-separated structures would be expected to be highly elongated in the direction perpendicular to the interface.[21,22] Thus, it is interesting to investigate the features of the mixtures of the block copolymer with the corresponding homopolymers in a two-dimensional system; however, it has not been explored due to the lack of suitable experimental techniques.

Characterization of the chain conformations in a bulk medium requires the technique that has both high spatial resolution and the capability to distinguish a single polymer chain from the bulk of the entangled chains. The fluorescence labeling technique is an established method for the selective imaging of such a single chain from its surroundings. However, conventional fluorescence microscopy suffers from the diffraction-limited resolution of a half of the wavelength of the incident light. Therefore, the application of the optical microscopy to single macromolecular imaging has been limited to the observation of huge biomacromolecules such as DNA.[32,33] Scanning near-field optical microscopy (SNOM) has been developed to provide the optical information with the high spatial resolution beyond the diffraction limit of light.[34] SNOM is a scanning probe microscopy

technique, which employs the probe tip having an aperture smaller than the wavelength of light. The incident light to the aperture generates an optical near-field restricted in the space of the aperture size, which enables us to illuminate the specimen and to obtain the optical response from the nanometric area. Therefore, the fluorescence imaging by SNOM is a promising technique for the direct observation of a single polymer chain in a bulk medium.[10,29,35,36] Yang et al. investigated the location and orientation of a single homopolymer chain embedded in a block copolymer lamella in the three-dimensional system by using SNOM.[10] A homopolymer with a molecular weight larger than that of a block copolymer tends to be located at the center of the corresponding block domain and orients itself depending on its location in the block domain. In this chapter, the conformation of a single dye-labeled poly(isobutyl methacrylate) (PiBMA:PDI) chain dispersed in the microphase-separated structure of poly(isobutyl methacrylate)-*block*-poly(octadecyl methacrylate) (PiBMA-*b*-PODMA) monolayer is studied by SNOM. The location and orientation of single PiBMA:PDI chains are discussed on the basis of quantitative fluorescence image analysis (chemical structures of PiBMA-*b*-PODMA and PiBMA:PDI are shown in Figure 2-1).

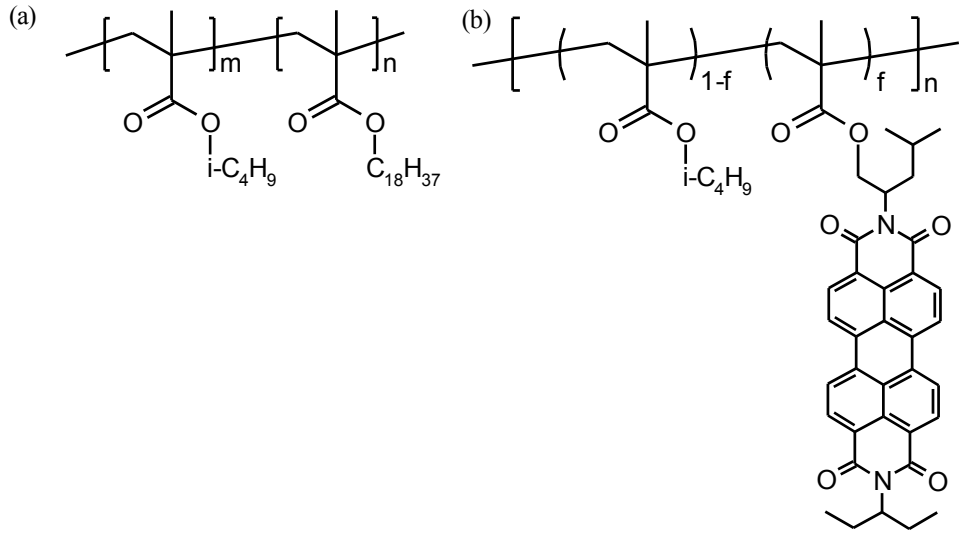

Figure 2-1. Chemical structures of (a) PiBMA-*b*-PODMA and (b) dye-labeled homopolymer PiBMA:PDI. The molar fraction of dye-labeled unit *f* is evaluated to be only 0.005.

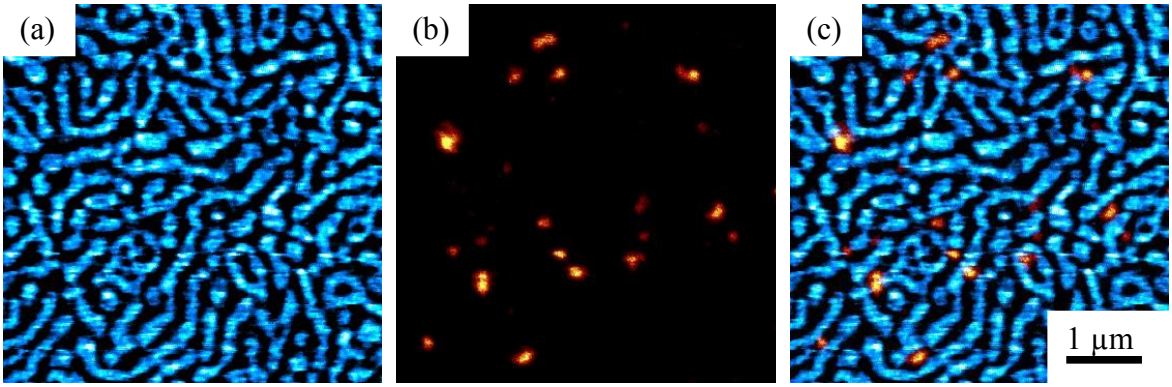

Figure 2-2. SNOM images of the PiBMA-*b*-PODMA/PiBMA:PDI monolayer: (a) surface topography (TP), (b) fluorescence (FL) images, and (c) superimposition of the panels (a) and (b). The blue and dark parts in panel (a) correspond to the PODMA and PiBMA domain, respectively. The bright spot in panel (b) corresponds to a single PiBMA:PDI chain.

2.2. Results and Discussion

Figure 2-2 shows a set of SNOM images of a blend monolayer of PiBMA-*b*-PODMA and PiBMA:PDI, in which the fraction of the PiBMA:PDI is 0.25%, was obtained simultaneously from an area of 5 μm × 5 μm. The microphase-separated structure of the PiBMA-*b*-PODMA with the regular spacings was clearly observed in the surface topography of Figure 2-2a. The blue area indicates the region higher than the dark part. Because PODMA has a long alkyl side chain, the thickness of the PODMA monolayer is 2 nm thicker than that of the PiBMA monolayer.[25,26] Therefore, the blue and dark areas in Figure 2-2a correspond to the PODMA and PiBMA domains, respectively. The FFT pattern of the surface topography (TP) image showed the peak at 2.9 μm^{-1}, indicating that the average width of the PiBMA domain was 180 nm. For a symmetric block copolymer, the most stable phase-separated structure is expected to be a lamellar structure with the parallel orientation. However, partially constructed lamellar structures were observed instead of the long-range ordered lamellar structure as shown in Figure 2-2a. To obtain a long-range ordered structure, further annealing was carried out, but little change could be seen after 30 h. On the other hand, in the case of PiBMA-*b*-PODMA with the low degree of polymerization (DP) of 1600, the long-range ordered lamellar structure was observed within 1 h (data is not shown). The rather

disordered structure of the high molecular weight PiBMA-*b*-PODMA is explained both by the molecular weight dependence of the surface viscosity[28] and the effect that polymer chains are restricted in the two-dimensional plane. Because overlapping among the polymer chains is not allowed in two-dimensions, it is difficult for a high molecular weight polymer to rearrange the location and conformation of the polymer chain. Therefore a long-range ordered lamella cannot be obtained. The bright spot in the fluorescence (FL) image of Figure 2-2b corresponds to the single homo-PiBMA chain dispersed in the block copolymer monolayer.[37] From a superimposed image of the TP and FL images (Figure 2-2c), it was found that the homo-PiBMA chains were located at the PiBMA domain of the microphase-separated structure of the PiBMA-*b*-PODMA lamella.

The conformation of the single PiBMA chain was quantitatively evaluated from the fluorescence intensity distribution.[33] The fluorescence intensity is proportional to the number of fluorescence dye molecules randomly introduced along the PiBMA:PDI main chain; therefore, the intensity at each pixel corresponds to the number of chain segments therein. The first moment of the fluorescence intensity distribution denotes the position of the center of mass (CM)

$$x_{\mathrm{CM}} = \frac{1}{I_0}\sum_i x_i I_i$$
$$y_{\mathrm{CM}} = \frac{1}{I_0}\sum_i y_i I_i \qquad (2\text{-}1)$$

where I_i is the fluorescence intensity at the i-th pixel, (x_i, y_i) is the Cartesian coordinate of the i-th pixel, and I_0 is the total fluorescence intensity from the single chain. The second moments of the fluorescence intensity distribution are expressed as Eq. 2-2.

$$R_{xx}^2 = \frac{1}{I_0}\sum_i (x_i - x_{\mathrm{CM}})^2 I_i$$
$$R_{yy}^2 = \frac{1}{I_0}\sum_i (y_i - y_{\mathrm{CM}})^2 I_i \qquad (2\text{-}2)$$
$$R_{xy}^2 = R_{yx}^2 = \frac{1}{I_0}\sum_i (x_i - x_{\mathrm{CM}})(y_i - y_{\mathrm{CM}}) I_i$$

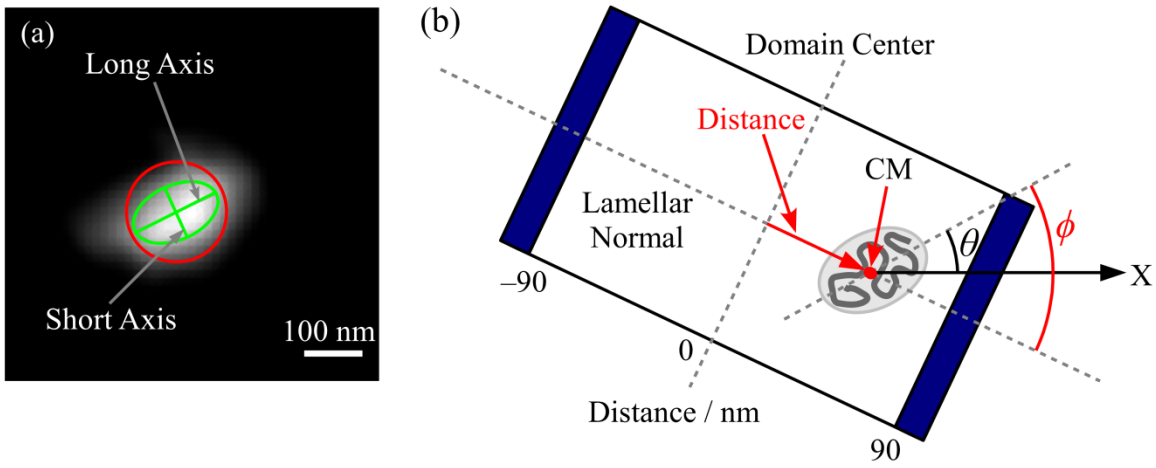

Figure 2-3. (a) Enlarged FL image of a single PiBMA chain. The radius of the red circle is the calculated R_{2D} of the homo-PiBMA chain. The green ellipse is drawn with the square roots of the two eigenvalues (λ_l and λs) as the long and short axes. The scale bar is 100 nm. (b) Schematic image shows the determination of the distance and orientational angle, ϕ; the origin of the distance coordinate is set at the center of the PiBMA domain and the positive direction to the right-hand side of the image.

The tensor **R** is a parameter related to the polymer chain conformation.

$$\mathbf{R} = \begin{pmatrix} R_{xx}^2 & R_{xy}^2 \\ R_{yx}^2 & R_{yy}^2 \end{pmatrix} \tag{2-3}$$

In this way, the investigated polymer chain spot can be represented as an ellipse with long and short principal axes.[32,33] The eigenvalues of the **R**, λ_l and λ_s ($\lambda_l > \lambda_s$), correspond to the squared lengths of the long and short axes of the most appropriate ellipsoid. The trace of **R** is the square radius of gyration in the XY plane, R_{2D}. The angle, θ, between the long principal axis and the X-axis are given by Eq. 2-4.

$$\theta = \arctan\left(\frac{\lambda_l - R_{xx}^2}{R_{xy}^2}\right) \tag{2-4}$$

Then, the orientational angle, ϕ, of the long principal axis relative to the direction perpendicular to the domain interface (lamellar normal) was evaluated from the angle, θ. The above descriptions are summarized in Figure 2-3. Using the above methodology of the SNOM image analysis, about 80 PiBMA:PDI chains located at different areas in the lamellar domains were analyzed.

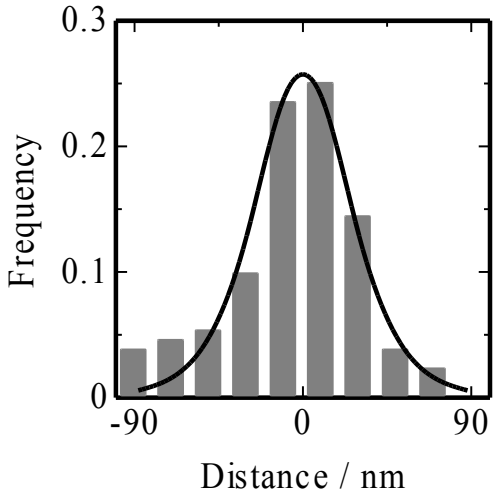

Figure 2-4. Histogram of the distribution of the homo-PiBMA chain in the PiBMA-*b*-PODMA lamellar domain. The normalized population of the homo-PiBMA chains is plotted against the distance between the CM of a homo-PiBMA chain and the center of the PiBMA domain. The interface corresponds to ±90 nm in the distance coordinate. The solid line indicates the fitted homopolymer distribution.

The homo-PiBMA chains show the preferred location due to the energetic contribution. Therefore, the distribution of the homo-PiBMA chain in the PiBMA-*b*-PODMA lamellar domains is discussed from the distance between the CM of the homo-PiBMA chain and the center of the PiBMA domain in the direction of the lamellar normal as shown in Figure 2-3b; the origin of the distance coordinate was set at the center of the PiBMA domain and the positive direction to the right-hand side of the image. Because the width of the PiBMA domain was evaluated to be 180 nm as mentioned above, the interface between the two microdomains correspond to ± 90 nm in the distance coordinate. Figure 2-4 shows the histogram of the distribution of the CM of the homo-PiBMA chains in the PiBMA-*b*-PODMA lamella.

It is easily seen that the homo-PiBMA chains are almost localized at the center of the PiBMA domain. In order to discuss the distribution of the homopolymer in the lamellar domain, the histogram of Figure 2-4 was fitted with a simple hyperbolic tangent form[8,18]

$$\Psi_h(x) = a\left[\tanh\left(\frac{b+2x}{c}\right) + \tanh\left(\frac{b-2x}{c}\right)\right] \qquad (2\text{-}5)$$

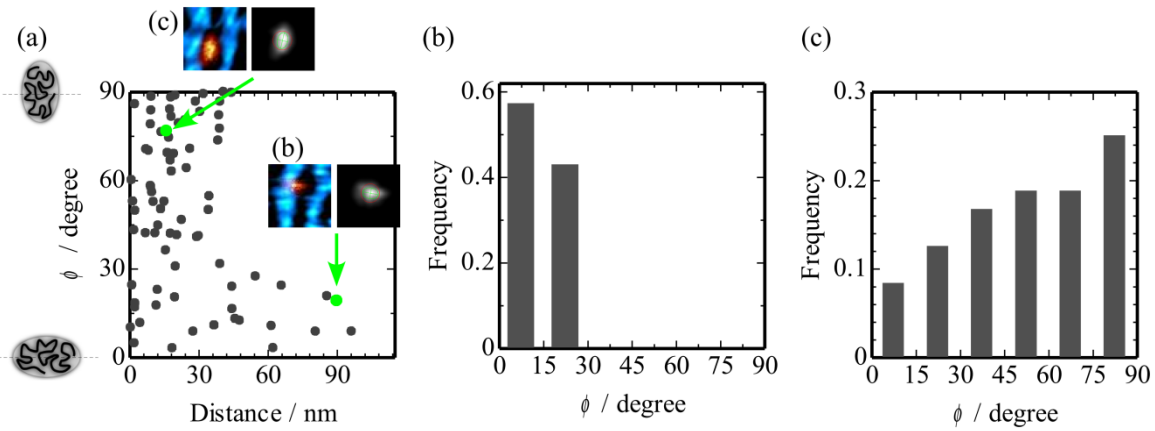

Figure 2-5. (a) Plot of the chain orientation of the homo-PiBMA chains against the CM location in the PiBMA domain. (b), (c) Histograms of the angle, ϕ, of the homo-PiBMA located near the interface (panel b) and at the center of the PiBMA domain (panel c). X-axis in the panel a shows the absolute value of the distance between the CM of a homo-PiBMA chain and the center of the PiBMA domain. Each point indicates a single PiBMA chain.

where a, b, and c are the floating parameters used in the fitting. The solid line in Figure 2-4 indicates the fitting result. From the full width at a half maximum (FWHM) of 60 nm, the ratio of FWHM to the domain width (FWHM/D) was evaluated to be 0.33. On the other hand, the FWHM/D of the previous work for a three-dimensional system of polystyrene-*block*-poly(methyl methacrylate)[10] was 0.56 (see the Appendix), suggesting that the homopolymer in two dimentions is more concentrated at the domain center compared to the three-dimensional bulk system. The conformation of the block chains in the microdomain would be different from the unperturbed homopolymer chain.[1,6,7,21,22] Thus, it is interesting to investigate the conformation of the homopolymer chain in the microdomain.[10,13,16] The in-plane radius of gyration, R_{2D}, of the homo-PiBMA chain was evaluated as a trace of **R** as mentioned above. The homo-PiBMA chains dispersed in the PiBMA-*b*-PODMA lamella have an average R_{2D} of 72 ± 18 nm, which is almost the same as the R_{2D} of the PiBMA chains in the neat PiBMA monolayer (68 ± 19 nm),[38] indicating that R_{2D} of the homopolymer is not significantly altered in the microphase-separated structure.

Now the author discusses the conformational orientation of the PiBMA chain embedded in the lamellar domain. The orientational angle between the long axis of the ellipsoid and the lamellar normal for each individual homo-PiBMA chain, ϕ, was plotted against the absolute distance in the lamellar domain in Figure 2-5a. It was found that the homo-PiBMA chains showed the orientation depending on the location of the homo-PiBMA chain in the PiBMA domain.[39] Most of the PiBMA chains at the location of >60 nm showed the orientational angle of <30°. Figure 2-5b shows the histogram of the orientational angle at distance of >60 nm. Figure 2-5b clearly indicates that the homo-PiBMA chain has the preferential orientation in the direction perpendicular to the interface. On the other hand, around the center of the lamellar domain, it seems that the chain orientation shows random distribution. Figure 2-5c shows the histogram of the orientational angle for the chains located at the domain center (distance <25 nm), indicating that the homo-PiBMA chain shows a weak tendency to orient itself parallel to the interface. Figure 2-5a also show the superimposed (TP and FL) images of two homo-PiBMA chains located at different positions in the PiBMA domain. From these images, one can easily see the tendency of the conformational orientation dependence on the location in the PiBMA domain.

A schematic image of the homo-PiBMA chain orientation in the PiBMA-*b*-PODMA lamella is shown in Figure 2-6. It is well known that the structure of a phase-separated block copolymer system is determined by the balance of the enthalpic gain by the separation of the incompatible block chains and the loss of the entropy due to the restricted conformation at the interface. When an ordered structure is formed, the block chains take a brush-like conformation with the loss of conformational entropy so as to reduce the unfavorable contact.[1,6,7] Especially, in the case of the two-dimensional system, because the polymer chains are not allowed to cross-over with other chains, the block chains would have to take highly stretched conformation in the direction perpendicular to the interface.[21,22] If the homo-PiBMA chain is sparsely located in a matrix of the PiBMA-*b*-PODMA lamella, the individual chain is confined to the PiBMA domain due to the repulsive interaction with PODMA. Because the investigated homo-PiBMA chain has a relatively large

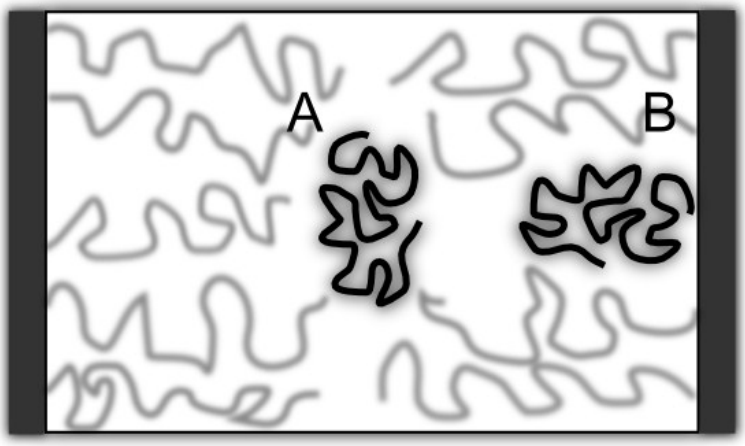

Figure 2-6. Schematic image of the relationship between the orientation and location of the homo-PiBMA chains. The gray coils represent the PiBMA block chains. The black coils represent homo-PiBMA chains.

molecular weight, it occupies a large area in the monolayer. If the homo-PiBMA chain existed in the copolymer brushes, it would disturb the brush conformation, resulting in the large entropic loss for the block chain. Therefore, the homo-PiBMA chain is expected to be excluded from the brushes and localized in the center of the PiBMA domain with narrower distribution than three-dimensional system due to the no degree of the cross-over and entanglement.

The homo-PiBMA chain is anisotropically confined by the brushes. The homo-PiBMA chain located at the center of the PiBMA domain is restricted not to expand in the direction perpendicular to the interface due to the no degree of the cross-over and entanglement with the brushes. Consequently, the homo-PiBMA chain were contracted in the direction perpendicular to the interface, and extended in a parallel direction as shown in chain A in Figure 2-6. On the other hand, some homo-PiBMA chains were located near the interface and showed elongated conformations perpendicular to the interface as shown in chain B in Figure 2-6. The homopolymer chain located near the interface would take a conformation along the block chain, which takes a stretched conformation perpendicular to the interface not to distort the brush conformation. A similar result was reported in the previous work for a three-dimensional system.[10] While only a weak tendency could be seen for in three-dimensional system (see the Appendix), a strong correlation between the

location and orientation of a homo-PiBMA chain was found in the two-dimensional system. Almost all the homo-PiBMA chains located near the interface were oriented in a direction perpendicular to the interface (Figure 2-5b). This is due to the confinement effect in a two-dimensional systems. Because the cross-over and entanglement among the polymer chain are not allowed in two-dimensions, the homopolymer chain dispersed in the microphase-separated monolayer is strongly affected by the block chain organization.

2.3. Conclusions

In this chapter, the phase-separated structure of poly(isobutyl methacrylate)-*block*-poly(octadecyl methacrylate) (PiBMA-*b*-PODMA) monolayer and single poly(isobutyl methacrylate) (PiBMA) chain dispersed therein was investigated by SNOM. The individual dye-labeled PiBMA chains dispersed in the microphase-separated block copolymer monolayer was directly observed by SNOM. It was found that the homo-PiBMA chains were almost located at the center of the PiBMA domain. The homopolymer chain was oriented depending on its location in the block domain. The homo-PiBMA chain located at the center of the PiBMA domain tended to be oriented in a direction parallel to the interface. The homo-PiBMA chain located near the interface was oriented in a direction perpendicular to the interface. This is because the effect of the anisotropic confinement from the block chain organization.

2.4. Experimental Section

Table 2-1. Characterizations of PiBMA-*b*-PODMA and PiBMA:PDI

	$DP_n / 10^{-3}$ [a]			
	PiBMA	PODMA	M_w/M_n	f [b]
PiBMA-*b*-PODMA	2.02	1.98	1.10	
PiBMA:PDI	11.0		1.21	0.005

[a] The number-averaged degree of polymerization. [b] The molar fraction of the dye unit.

PiBMA-*b*-PODMA was synthesized by the atom transfer radical polymerization.[22] The PiBMA homopolymer randomly labeled by perylene diimide (PDI) (PiBMA:PDI) was synthesized by radical copolymerization of isobutyl methacrylate and PDI-containing methacrylate. The obtained PiBMA:PDI was purified by the fractional precipitation in methanol from toluene to achieve a relatively narrow molecular weight distribution. The weight- and number-averaged molecular weights, M_w and M_n, were determined by gel permeation chromatography (D-7000G, Hitachi) with the eluent THF, which was calibrated by PS standards (Scientific Polymer Products) and a PiBMA secondary standard (Aldrich), and ^{1}H-NMR (JNM-EX400, JEOL). The fraction of the dye-labeled unit f was evaluated to be 0.5% from UV-Vis absorption (U3500, Hitachi). The properties of the PiBMA would not be affected by the introduction of the PDI moiety because of the low dye content. The average distance between the adjacent dye molecules was estimated to be 7.3 nm, which is larger than the Förster radius of the PDI (ca. 4 nm), resulting in monomer-like emission properties. The characterization of these polymers is summarized in Table 2-1. The monolayer was prepared by the Langmuir-Blodgett technique. A mixed solution of the PiBMA-*b*-PODMA and PiBMA:PDI in benzene was prepared at a concentration of 0.1 g L^{-1}, in which the fraction of the PiBMA:PDI was 0.25% to PiBMA-*b*-PODMA. The polymer solution was spread on pure water (NANOpure II, Barnstead) at 20 °C. The surface pressure was measured with a Wilhelmy plate.

Annealing was carried out by raising the water subphase temperature to 40 °C and keeping it constant for 2 h. Annealing was carried out in a constant area condition without surface pressure

control. After cooling the subphase temperature to 20 °C the monolayer was compressed to a surface pressure of 5 mN m^{-1} and transferred onto a glass cover slip by the vertical dipping method at a rate of 1.0 mm min^{-1}. In order to avoid the fluorescence quenching of the dye moiety, the monolayer was overcoated by a thin layer (10 nm) of poly(vinyl alcohol) (PVA) by the spincoating method. The SNOM measurement confirmed that the surface morphology of the monolayer was not altered by the PVA overcoating and it can be observed through the thin layer of PVA (see the Appendix).

The SNOM measurement was performed with a commercially available instrument (α-SNOM, WITec) with a hollow cantilever probe with a sub-wavelength aperture of 60 nm. The laser beam at a wavelength of 532 nm was focused onto the backside of the aperture to generate the optical near-field. The PDI fluorescence was collected with a microscope objective (0.80 NA, 60 × , Nikon) from the backside of the substrate and guided to an avalanche photo diode (SPCM-AQR-14, Perkin Elmer). The SNOM measurement was carried out at contact mode and in anambient condition. With the above experimental setup, TP and FL images can be simultaneously obtained from the scanning area.

2.5. Appendix

2.5.1. Surface Morphology after Overcoating.

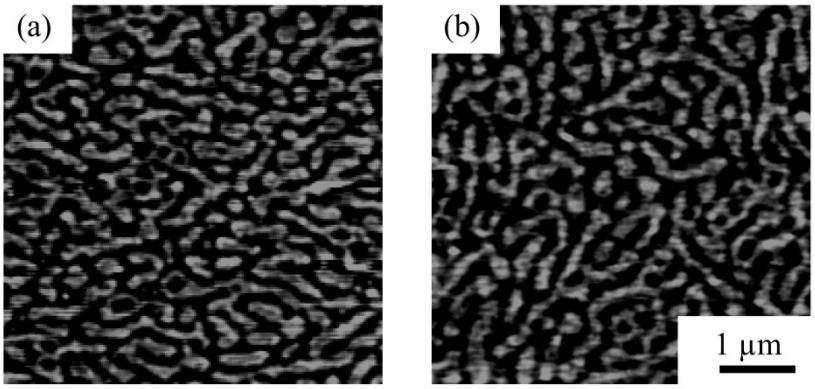

Figure 2-A1. Surface topography of the (a) before and (b) after overcoating.

The monolayer was overcoated with a PVA thin film to prevent quenching. It was confirmed that the surface morphology of the monolayer was not altered by the PVA overcoating. Figure 2-A1 shows AFM images of a monolayer before and after overcoating (not the same scanning area). The domain structures for them appear the same, and the FFT analysis showed that the domain width was not altered by the overcoating. The height difference between the PiBMA and PODMA domains in Figure 2-A1b was about 2 nm as well as Figure 2-A1a. These results indicate that the overcoating with PVA does not affect the microphase-separated structure of PiBMA-*b*-PODMA.

A dye-labeled symmetric PiBMA-*b*-PODMA (PiBMA-*b*-PODMA:Pe), in which the whole contour of the PODMA sub-chain was labeled by perylene dye, was prepared to confirm that the bright part in Figure 2-1b corresponds to the PODMA domain. When the PiBMA-*b*-PODMA forms a phase-separated structure, the PODMA domain can be identified from the perylene fluorescence in the FL image. The PVA-protected PiBMA-*b*-PODMA:Pe monolayer was prepared in the same procedure as mentioned in the Experimental Section. A 438 nm laser was used as the light source to excite the perylene dyes inside the film. All the SNOM experiments were performed in the same conditions as those for the PiBMA-*b*-PODMA/PiBMA system.

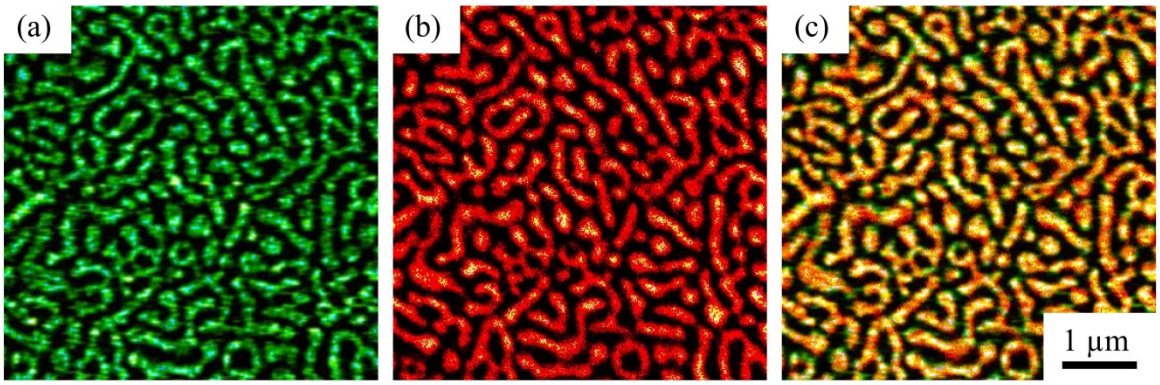

Figure 2-A2. SNOM images of PiBMA-*b*-PODMA:Pe monolayer (a) surface topography (b) fluorescence image, and (c) superimposition of the panels (a) and (b). The bright areas in (b) correspond to the perylene-labeled PODMA domain.

Figure 2-A2 shows a set of SNOM images obtained simultaneously from an area of 5 μm × 5 μm. The bright domain in the FL image of Figure 2-A2b indicates the PODMA domain. Figure 2-A2a and Figure 2-A2b shows almost the same structure. For the quantitative comparison of these images, they were superimposed in Figure 2-A2c. For the superimposition of these images, the FL image was shifted 110 nm according to the X-axis and 14 nm to the Y-axis. This image shift is probably due to the different positions of the topographic and optical probes, which correspond to a physical protrusion and an aperture at the tip end, respectively. The superimposed image shows that the TP and FL images are completely overlapped, indicating that the bright part in the TP image of Figure 2-A2a corresponds to the PODMA domain. Thus, the monolayer was expected to be unaffected by the overcoating method.

2.5.2. Distribution of the Homo-PMMA Chain in a Three-Dimensional Microphase-Separated Structure of PS-*b*-PMMA Lamella. Yang et al. reported that the homo-PMMA chains embedded in the PS-*b*-PMMA thick film were distributed through the PMMA domain (Figure 2-A3).[10] The solid line in Figure 2-A3 indicate the fitting result with Eq. 2-5. The full width at half maximum (FWHM) is estimated to be 44 nm, which corresponds to FWHM/D of 0.56.

2.5.3. Distributions of the Orientation of PMMA in a Three-Dimensional Microphase-Separated Structure of PS-*b*-PMMA Lamella. Yang et al. also reported that the homo-PMMA chains embedded in the PS-*b*-PMMA lamella were oriented depending on their locations in the PMMA domain in three dimensional bulk.[10] Figure 2-A4 shows the distribution of the orientational angle, ϕ, of the homo-PMMA chains located at the domain center and near the interface, respectively. The orientational angle of the PMMA chain located near the interface is randomly distributed from 0° in 50°, while most of the chains located near the interface showed the orientational angle of <30° in two-dimensional system (Figure 2-A4b). This weak tendency in the three-dimensional system is attributed to the increase in the conformational freedom. Since the polymer chain in the three-dimensional system is allowed to entangle with other chains, the polymer chains can rotate more freely than in a two-dimensional system.

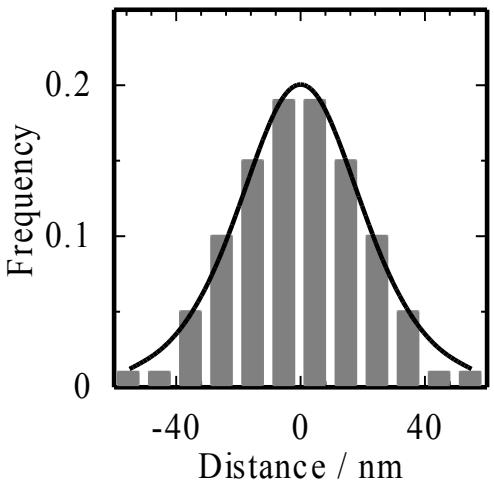

Figure 2-A3. Histogram of the distribution of the homo-PMMA chain in the PS-*b*-PMMA lamellar domain. The normalized population of the homo-PMMA chains is plotted against the distance between the CM of a homo-PMMA chain and the center of the PMMA domain. The interface corresponds to ± 41 nm in the distance coordinate. The solid line indicates the fitting result. The figure was reproduced from the data in the literature: Yang et al. *Macromolecules*, **2007**, *40*, 7573–7580.

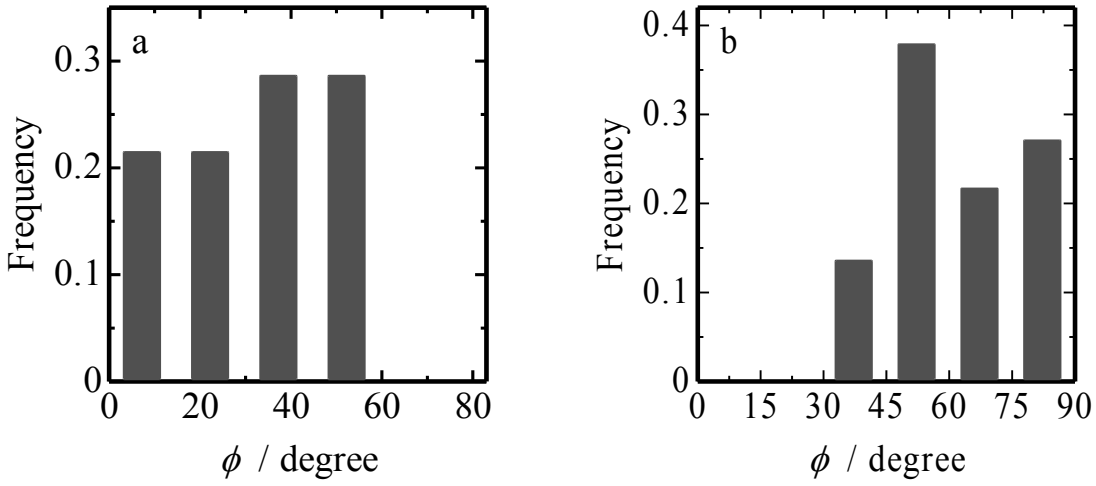

Figure 2-A4. Histograms of the orientational angle, ϕ, of the homo-PMMA located near the interface (a) and at the domain center (b), respectively. The figure was reproduced from the data in the literature: Yang et al. *Macromolecules*, **2007**, *40*, 7573–7580.

References and Notes

(1) Bates, F. S.; Fredrickson, G. H. *Annu. Rev. Phys. Chem.* **1990**, *41*, 525–557.

(2) Inoue, T.; Soen, T.; Hashimoto, T.; Kawai, H. *J. Polym. Sci., Part A2* **1969**, *7*, 1283–1301.

(3) Helfand, E.; Wasserman, Z. R. *Macromolecules* **1976**, *9*, 879–888.

(4) Hashimoto, T.; Shibayama, M.; Kawai, H. *Macromolecules* **1980**, *13*, 1237–1247.

(5) Matsushita, Y.; Mori, K.; Saguchi, R.; Nakao, Y.; Noda, I.; Nagasawa, M. *Macromolecules* **1990**, *23*, 4313–4316.

(6) Hasegawa, H.; Hashimoto, T.; Kawai, H.; Lodge, T. P.; Amis, E. J.; Glinka, C. J.; Han, C. C. *Macromolecules* **1985**, *18*, 67–78.

(7) Matsushita, Y.; Mori, K.; Mogi, Y.; Saguchi, R.; Noda, I.; Nagasawa, M.; Chang, T.; Glinka, C. J.; Han, C. C. *Macromolecules* **1990**, *23*, 4317–4321.

(8) Shull, K. R.; Winey, K. I. *Macromolecules* **1992**, *25*, 2637–2644.

(9) Vavasour, J. D.; Whitmore, M. D. *Macromolecules* **2001**, *34*, 3471–3483.

(10) Yang, J.; Sekine, R.; Aoki, H.; Ito, S. *Macromolecules* **2007**, *40*, 7573–7580.

(11) Hashimoto, T.; Tanaka, H.; Hasegawa, H. *Macromolecules* **1990**, *23*, 4378–4386.

(12) Tanaka, H.; Hasegawa, H.; Hashimoto, T. *Macromolecules* **1991**, *24*, 240–251.

(13) Hasegawa, H.; Tanaka, H.; Hashimoto, T.; Han, C. C. *J. Appl. Crystallogr.* **1991**, *24*, 672–678.

(14) Koizumi, S.; Hasegawa, H.; Hashimoto, T. *Macromolecules* **1994**, *27*, 7893–7906.

(15) Matsushita, Y.; Torikai, N.; Mogi, Y.; Noda, I.; Han, C. C. *Macromolecules* **1993**, *26*, 6346–6349.

(16) Matsushita, Y.; Torikai, N.; Mogi, Y.; Noda, I.; Han, C. C. *Macromolecules* **1994**, *27*, 4566–4569.

(17) Torikai, N.; Takabayashi, N.; Noda, I.; Koizumi, S.; Morii, Y.; Matsushita, Y. *Macromolecules* **1997**, *30*, 5698–5703.

(18) Mayes, A. M.; Russell, T. P.; Satija, S. K.; Majkrzak, C. F. *Macromolecules* **1992**, *25*, 6523–6531.

(19) Orso, K. A.; Green, P. F. *Macromolecules* **1999**, *32*, 1087–1092.

(20) Okubo, M.; Saito, N.; Takekoh, R.; Kobayashi, H. *Polymer* **2005**, *46*, 1151–1156.

(21) Kumaki, J.; Hashimoto, T. *J. Am. Chem. Soc.* **1998**, *120*, 423–424.

(22) Aoki, H.; Kunai, Y.; Ito, S.; Yamada, H.; Matsushige, K. *Appl. Surf. Sci.* **2002**, *188*, 534–538.

(23) Gabrielli, G.; Puggelli, M.; Baglioni, P. *J. Colloid Interface Sci.* **1982**, *86*, 485–500.

(24) Wu, S.; Huntsber, Jr *J. Colloid Interface Sci.* **1969**, *29*, 138–147.

(25) Naito, K. *J. Colloid Interface Sci.* **1989**, *131*, 218–225.

(26) Mumby, S. J.; Swalen, J. D.; Rabolt, J. F. *Macromolecules* **1986**, *19*, 1054–1059.

(27) de Gennes, P. G. *Scaling Concepts in Polymer Physics*; Cornell University Press: Ithaca, NY, **1979**.

(28) Sato, N.; Ito, S.; Yamamoto, M. *Macromolecules* **1998**, *31*, 2673–2675.

(29) Aoki, H.; Anryu, M.; Ito, S. *Polymer* **2005**, *46*, 5896–5902.

(30) Aoki, H.; Sakurai, Y.; Ito, S.; Nakagawa, T. *J. Phys. Chem. B* **1999**, *103*, 10553–10556.

(31) Aoki, H.; Ito, S. *J. Phys. Chem. B* **2001**, *105*, 4558–4564.

(32) Maier, B.; Radler, J. O. *Phys. Rev. Lett.* **1999**, *82*, 1911–1914.

(33) Maier, B.; Radler, J. O. *Macromolecules* **2001**, *34*, 5723–5724.

(34) Betzig, E.; Trautman, J. K. *Science* **1992**, *257*, 189–195.

(35) Ube, T.; Aoki, H.; Ito, S.; Horinaka, J.; Takigawa, T. *Polymer* **2007**, *48*, 6221–6225.

(36) Aoki, H.; Morita, S.; Sekine, R.; Ito, S. *Polym. J.* **2008**, *40*, 274–280.

(37) The PiBMA-*b*-PODMA with different trace amounts of PiBMA:PDI was measured by SNOM for each sample. The FL images show that all fluorescent spots are homogeneously distributed throughout the monolayer. For each FL image, the number density of the fluorescence spots was calculated. The number density of the fluorescent spots is in good agreement with the number density of the PiBMA:PDI chains in the PiBMA-*b*-PODMA, based on the molar ratio, indicating that homo-PiBMA chains did not aggregate and one

fluorescent spot in the FL images corresponds to a single PiBMA:PDI chain dispersed in the PiBMA-*b*-PODMA.

(38) The R_{2D} of the homo-PiBMA chains dispersed in the PiBMA monolayer matrix was evaluated by the same method as mentioned above. The DP_n of the matrix PiBMA is 2200, which is almost the same as the DP_n of the PiBMA block of the PiBMA-*b*-PODMA.

(39) The orientational angle of the homo-PiBMA chains in the neat PiBMA monolayer was estimated by the same method mentioned above. FL images show that the homo-PiBMA chains have no preferred orientation in the PiBMA monolayer matrix.

Chapter 3

Dynamical Excimer Formation in Rigid Carbazolophane via Charge Transfer State

3.1. Introduction

Intramolecular excimer has attracted much attention from the view point of the relationship between the molecular structure and the formation dynamics.[1–8] The intramolecular excimers can be formed when the stabilization energy due to exciton and charge resonance interactions exceeds the conformational instability.[9–14] Previous studies have shown that the intramolecular singlet excimer is the most stable when the two chromophores can overlap in a symmetric sandwich or totally eclipsed geometry. On the other hand, Lim et al. proposed the L-shaped structure of the triplet excimers of naphthalene, which is stabilized mostly by charge transfer (CT) interaction.[15–17] In other words, the intramolecular excimer formation is strongly dependent on conformational rearrangement in the excited state. Solvent-polarity-induced intramolecular excimer was first observed for 1,2-di(1-anthryl)ethane where the excimer formation was promoted in polar solvents.[18–20] The solvent-polarity dependence is a clear indication of an intermediate CT state in the excimer formation process. Their result suggests that the activation energy of the conformational rearrangement is reduced in the CT state, and hence the excimer is formed more easily.

Cyclophanes are one of the most reliable molecules for studying the interchromophoric interactions between two chromophoric groups not only in the ground state but also in the excited state,[21–25] because they have a rigid structure where the relative geometry of two chromophoric groups is clearly defined. In particular, various *syn*-cyclophanes have been studied to examine

excimer properties in terms of their structures.[26–35] On the other hand, the *anti*-cyclophanes have a structure where two chromophores are bridged in anti-parallel geometry. Thus, the *anti–syn* isomerization in the *anti*-cyclophanes is difficult in the ground state because of large activation energy.[36–44] Nonetheless, the intramolecular excimer formation in the *anti*-cyclophanes has been reported by several groups.[38–40] Mataga et al. reported the intramolecular excimer formation in metapyrenophane (mePy).[39,40] Interestingly, the intramolecular excimer in mePy is formed only in polar solvents, suggesting that conformational change in mePy would be favorable in the CT state similarly to the case of 1,2-di(1-anthryl)ethane.[40] However, the direct observation of intramolecular excimer formation dynamics in rigid *anti*-cyclophanes have not been reported so far and the relationship between the CT state and the excimer formation dynamics is not fully understood.

In this chapter, the intramolecular excimer formation dynamics in a carbazolophane, dioxa[3.3](3,6)carbazolophane (CzOCz, the chemical structure is shown in Figure 3-1) in which two *N*-ethylcarbazole rings are linked at 3 and 6 positions with CH_2OCH_2 bridges is studied.[44] Previously, it was showed that the stacking mode of two carbazole rings in CzOCz is the *anti*-conformation in the ground state as shown in Figure 3-1, and hence no excimer emission is observed for CzOCz in a 2-methyltetrahydrofuran solution. In this study, it was found that CzOCz exhibits a clear excimer emission in polar solvents such as acetonitrile (MeCN). This result suggests that the conformational rearrangement in CzOCz would be promoted by the CT state. Here, solvent-polarity-induced intramolecular excimer formation dynamics is studied experimentally by using time-resolved spectroscopic methods, and computationally by using molecular mechanics and density functional theory (DFT). The solvent-polarity dependence of the intramolecular excimer formation is discussed in terms of the conformation of CzOCz.

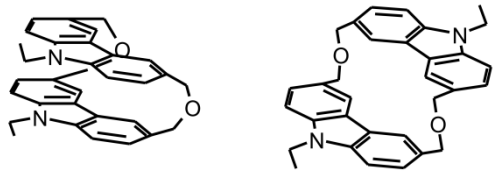

syn-CzOCz *anti*-CzOCz

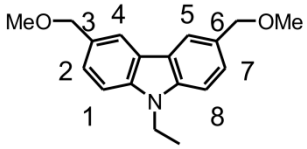

CzOMe

Figure 3-1. Chemical structures of dioxa[3.3](3,6)carbazolophane (CzOCz) in *syn*- and *anti*-conformation and 3,6-bis(methoxymethyl)-*N*-ethylcarbazole (CzOMe) as a reference.

Table 3-1. ^{1}H-NMR Chemical Shifts of Aromatic Protons in CzOCz and CzOMe.

	H1/H8	H2/H7	H4/H5
CzOCz	7.48	7.64	8.15
CzOMe	7.41	7.58	8.10

3.2. Results

3.2.1. ^{1}H-NMR of CzOCz in Solution. As shown in Figure 3-1, there are at least two possible isomers in CzOCz: one is *syn*-conformer (*syn*-CzOCz) where two carbazole rings are fully overlapped, and the other is *anti*-conformer (*anti*-CzOCz) where two carbazole rings are aligned in anti-parallel geometry. To identify the isomeric structure in the ground state, ^{1}H-NMR spectra of CzOCz and CzOMe (a reference monomer) in DMSO-d_6 solution was measured at room temperature. As summarized in Table 3-1, the chemical shifts of the aromatic protons in CzOCz are almost the same as CzOMe.[44] The difference between them is as small as <0.1 ppm, indicating that two carbazole rings in CzOCz are far apart and little overlapped in the *anti*-conformation as reported previously.[44] No distinct difference in the chemical shift was observed even at 150 °C. This finding

suggests that the isomerization from *anti*- to *syn*-conformation is negligible in the ground state because of large activation energy.

3.2.2. Absorption and Fluorescence Spectra. Figure 3-2a shows the absorption spectra of CzOCz and CzOMe in an MeCN solution at room temperature. There is no distinct difference in the absorption spectra between CzOCz and CzOMe, which is consistent with the *anti*-conformation of CzOCz in the ground state. The absorption bands at 300 and 350 nm are assigned to the $^1L_a \leftarrow {}^1A$ and $^1L_b \leftarrow {}^1A$ transitions, respectively.[45–47] On the other hand, as shown in Figure 3-2b, there is a clear difference in the fluorescence spectra between CzOCz and CzOMe in an MeCN solution at room temperature. In the fluorescence spectrum of CzOCz, a strong vibronic emission band was observed at around 360 nm and a weak and broad emission band was additionally observed at around 430 nm. The emission band at 360 nm is in good agreement with that of CzOMe and hence is ascribed to the monomer emission band. The structureless shoulder peak around 430 nm disappeared after O_2 bubbling, suggesting that this band is due to a long-lived excited species. As shown by the broken line in the figure, the differential spectrum before and after O_2 bubbling exhibits a broad emission band without vibrational structures, which is in good agreement with the carbazole excimer emission reported previously.[30–35,46] Note that no excimer emission was observed for the CzOMe solution under the same concentration. Thus, the broad emission at 430 nm is ascribed to the intramolecular excimer of CzOCz in MeCN. In summary, the interchromophoric interaction in CzOCz is negligible in the ground state but considerable in the excited state.

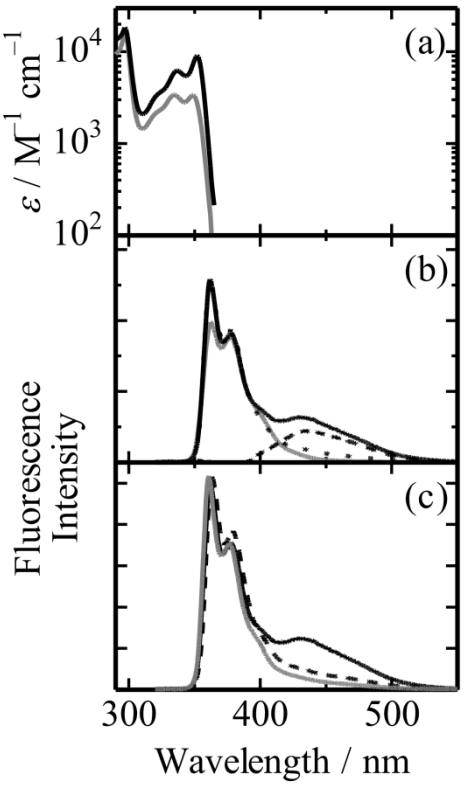

Figure 3-2. (a) Absorption spectra of CzOCz (black solid), and CzOMe (gray solid) in an MeCN solution at room temperature. (b) Fluorescence spectra of CzOCz (black solid) and CzOMe (gray solid) in an MeCN solution at room temperature: after Ar (black solid) and O_2 (black dotted) bubbling; the subtracted spectrum (black broken). (c) Fluorescence spectra of CzOCz in MeCN (black solid), DMF (black broken), and THF (gray solid) solutions at room temperature.

Figure 3-2c shows the fluorescence spectra of CzOCz in different solutions: MeCN (dielectric constant $\varepsilon_r = 37.5$, solvent viscosity $\eta = 0.35$ cP), *N*,*N*-dimethyl formamide (DMF; $\varepsilon_r = 36.7$, $\eta = 0.92$ cP), and tetrahydrofuran (THF; $\varepsilon_r = 7.58$, $\eta = 0.55$ cP). The excimer emission intensity was much stronger in the more polar MeCN than in the less polar THF solution, suggesting that the excimer formation is more efficient in polar solvents with higher dielectric constants. It is noteworthy that the peak wavelength of the excimer band was independent of the dielectric constant of solvents as described below. On the other hand, the excimer emission intensity was much stronger in the less viscous MeCN than in the more viscous DMF solution, indicating that the excimer formation is accompanied by some conformational changes, most probably *anti–syn* isomerization in the excited

state as will be discussed later. In summary, the excimer formation in CzOCz is favorable in solvents with a higher dielectric constant and lower viscosity.

3.2.3. Time-Resolved Emission. To examine the excimer formation dynamics, the time-resolved emission spectra and decay of CzOCz in MeCN, DMF, and THF solutions was measured. As shown in Figure 3-3a, a sharp monomer band was observed at 360 nm immediately after the laser excitation and then decayed in a few nanoseconds. Subsequently, a broad excimer band was observed at 430 nm after several ten nanoseconds. This temporal change in the emission spectra clearly shows the dynamic formation of the intramolecular excimer from the monomer state. The peak wavelength of the excimer band was neither shifted with time nor dependent on the solvent polarity. Figure 3-3b shows the time evolution of the monomer band at 360 nm and the excimer band at 450 nm. The decay of the monomer band was fitted by a single exponential function, and the rise and decay of the excimer band was fitted by double exponential functions. As summarized in Table 3-2, the decay constant of the monomer band (τ_{mono}) is shorter than that of the reference emission of CzOMe (τ_f^0) and is in good agreement with the rise constant of the excimer band. The coincidence in the rise and decay constants is kinetic evidence for the dynamic formation of the intramolecular excimer in CzOCz. The apparent excimer formation rate constant $k_{ex} = 1/\tau_{mono} - 1/\tau_f^0$ was estimated to be 5.6×10^8 s^{-1} in an MeCN solution, 2.1×10^8 s^{-1} in a DMF solution, and 1.3×10^8 s^{-1} in a THF solution. This trend in k_{ex} is consistent with that in the excimer intensity as mentioned above, and thus again indicates that the excimer formation in CzOCz is accompanied by some conformational changes in the excited state and is more rapid in polar solvents. As listed in Table 3-2, the decay constant of the excimer emission was longer than that of CzOMe monomer emission, indicating that the excimer emission is symmetrically forbidden as reported previously.[32–34,46] Furthermore, the decay constant was independent of solvents, suggesting that conformation of the excimer state is independent of solvent polarity and viscosity and that CT character of the excimer state is negligibly small. In

summary, these findings indicate that the CzOCz excimer is *syn*-conformation rather than *anti*-conformation.

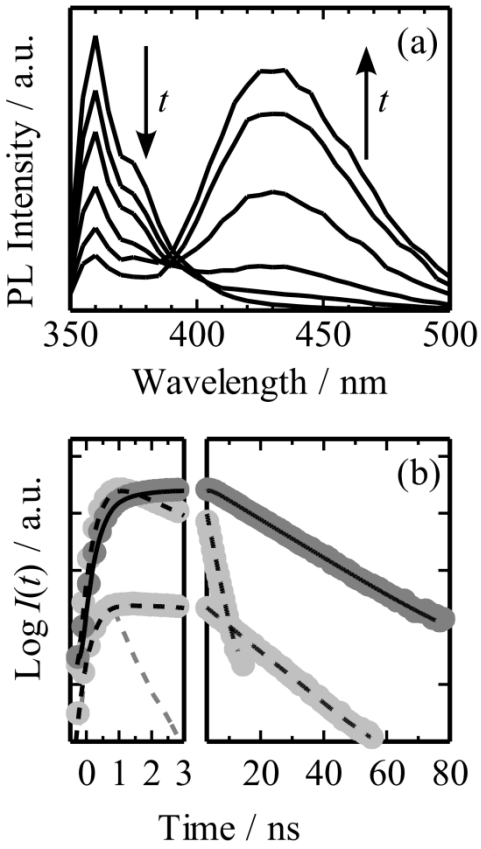

Figure 3-3. (a) Time-resolved emission spectra of CzOCz in an MeCN solution at room temperature measured at 0.5, 3, 5, 7.5, 10, and 20 ns after the laser excitation. (b) Fluorescence decay curves of (upper) CzOCz and (lower) CzOMe in an MeCN solution at room temperature. The excitation wavelength was 296 nm for all the samples. The detection wavelengths were 360 nm for monomer emission and 450 nm for excimer emission. The gray broken line represents an instrument response function. The black solid and broken lines represent fitting curves with two and one exponential functions, respectively.

Table 3-2. Fitting Parameters for Fluorescence Decay and Apparent Excimer Formation Rate.

	360 nm (decay, ns)	450 nm (rise, ns)	450 nm (decay, ns)	k_{ex} [a] (10^8 s^{-1})
in MeCN	1.6	1.5	12.9	5.6
in DMF	3.1	3.1	12.9	2.1
in THF	4.4	4.2	12.6	1.3
CzOMe	9.5	—	—	—

[a] The apparent excimer formation rate constant k_{ex} was estimated as $k_{ex} = 1/\tau_{mono} - 1/\tau_f^0$.

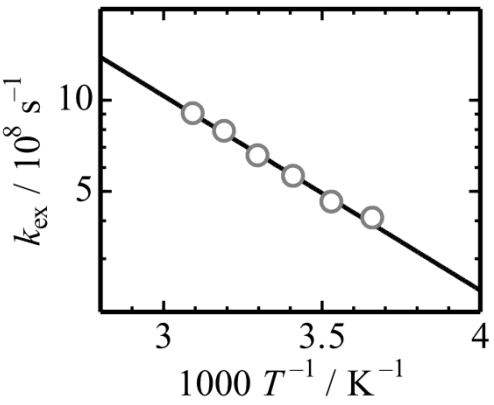

Figure 3-4. Arrhenius plots of the apparent excimer formation rate constant k_{ex} of CzOCz in an MeCN solution against the temperature from 273 to 323 K. The apparent excimer formation rate constant k_{ex} was estimated as $k_{ex} = 1/\tau_{mono} - 1/\tau_f^0$. The solid line represents the fitting curve with the Arrhenius equation: $\ln k_{ex} = \ln A - E_a/RT$. From the best fitting result, the pre-exponential factor A was estimated to be 8.6×10^{10} s^{-1} for all the solvents employed (data for THF solution is not shown). The apparent activation energy E_a was estimated to be 12.3 kJ mol^{-1} for an MeCN solution and 16.1 kJ mol^{-1} for a THF solution.

Figure 3-4 shows the Arrhenius plots of k_{ex} of CzOCz in an MeCN solution against the temperature ranging from 273 to 323 K. The solid line represents a fitting curve by the Arrhenius equation: $k_{ex} = A \exp(-E_a/RT)$ where A is the pre-exponential factor and E_a is the apparent activation energy for the excimer formation. The pre-exponential factor A was estimated to be 8.6×10^{10} s^{-1} for all the solvents employed. Thus, the difference in the excimer formation efficiency is attributed to the activation energy difference. The apparent activation energy E_a was estimated to be 12.3 kJ

mol^{-1} in an MeCN solution and 16.1 kJ mol^{-1} in a THF solution. Because the activation energy due to solvent viscosity E_η has been reported to be about 7.1 kJ mol^{-1} (MeCN) and 7.5 kJ mol^{-1} (THF),[48, 49] the activation energy for the isomerization E_{iso} was estimated to be as low as 5.2 kJ mol^{-1} (MeCN) and 8.6 kJ mol^{-1} (THF). This finding indicates that the potential barrier for the isomerization is much lower than that in the ground state and becomes lower in polar solutions as will be discussed later.

3.2.4. Transient Absorption. Figure 3-5 shows the transient absorption spectra of CzOCz and CzOMe in various solutions measured from 1 ps to 3 ns after the laser excitation at 350 nm. Immediately after the laser excitation at 1 ps, two absorption bands were observed at 650 and 1100 nm for all the solutions. These bands are ascribed to the $S_n \leftarrow S_1$ absorption of the carbazole monomer as reported previously.[34,50] In other words, the primary photoexcitation in CzOCz is localized onto one carbazole ring because CzOCz takes *anti*-conformation in the ground state. On a time scale of nanoseconds, a new absorption band gradually increased at around 900 nm. The rise time of this band was estimated to be 1.2 ns for CzOCz in an MeCN solution, which is in good agreement with the excimer rise time mentioned above (see the Appendix). At 3 ns after the laser excitation (red solid), the new band was observed for all three solutions. As reported previously, this band is ascribed to the charge transfer (CT) band of carbazole excimer, which is sensitive to the relative configuration of two carbazole rings.[34] As shown in Figure 3-5, the peak wavelength was independent of the solvent employed, which is consistent with the time-resolved emission spectra. Thus, these findings suggest that the conformation of CzOCz excimer is almost the same for all the solvents employed. Note that no remarkable absorption change was observed for the band at 650 nm. This is because the $S_n \leftarrow S_1$ absorption of the carbazole monomer is almost the same as the local excitation (LE) band of the carbazole excimer.[34] It is also noted that other transients such as radical ion or ion pair were not observed under this experimental conditions.

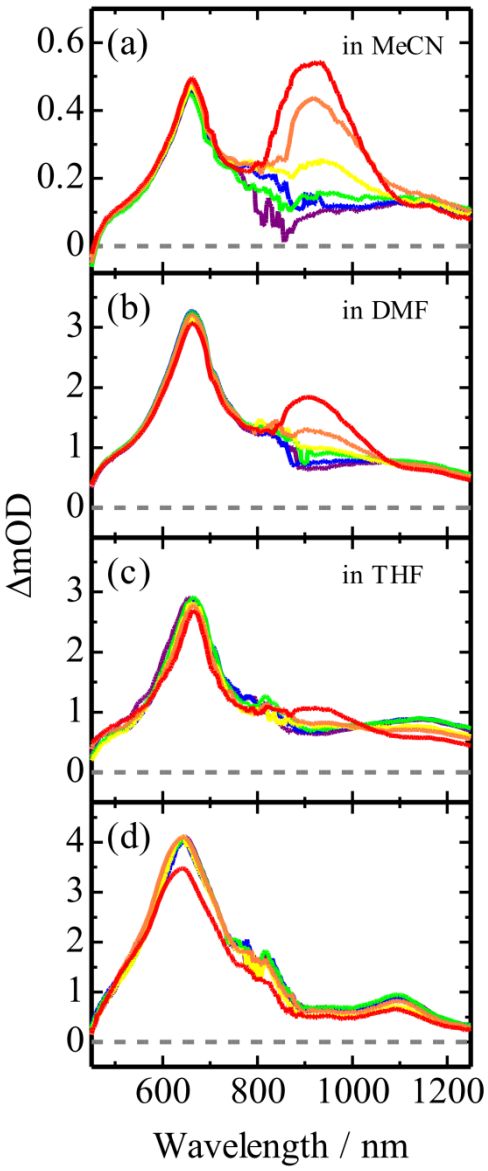

Figure 3-5. Transient absorption spectra of (a–c) CzOCz and (d) CzOMe solutions measured at (purple) 1, (blue) 10, (green) 100, (yellow) 500, (orange) 1000, and (red) 3000 ps after the laser excitation at 350 nm (~30 μJ cm^{-2}). Solvents were (a) MeCN, (b,d) DMF, and (c) THF.

3.2.5. Molecular Mechanics and Quantum Chemical Calculations. To find the most stable conformation, the potential energy surface of CzOCz in the ground state was calculated by using the AMBER force field[51] where the dihedral angles φ_1 and φ_2 are defined as shown in Figure 3-6a. As a result, three local potential minima were found as shown in Figure 3-6b. The first one is the *anti*-conformer with $\varphi_1 \approx \varphi_2 \approx -50$ ° where two carbazole rings are aligned in anti-parallel. The second one is the *syn*-conformer with $\varphi_1 \approx -75$ ° and $\varphi_2 \approx 75$ ° where two carbazole rings are aligned in parallel. The third one is an intermediate conformation with $\varphi_1 \approx -150$ ° and $\varphi_2 \approx 70$ ° where two carbazole rings are rather stacked in an edge-to-face geometry (hereafter abbreviated as *int*-conformation). As shown in Figure 3-6b, the direct *anti–syn* isomerization is impossible because of the high potential barrier (~150 kJ mol^{-1}). Furthermore, the potential barrier in the *anti–int* isomerization is also as high as 60 kJ mol^{-1}, which is consistent with the presence of only the *anti*-conformation of CzOCz in the ground state as mentioned above. The *anti–int* isomerization requires the cooperative rotation both in φ_1 and φ_2 while the *int–syn* isomerization is almost dependent on the φ_1 rotation alone, suggesting that the *anti–int* isomerization is more difficult than the *int–syn* isomerization. Indeed, as shown in Figure 3-6c, the potential barrier is higher in the *anti–int* isomerization than in the *int–syn* isomerization. This is probably true in the excited state although the potential is calculated in the ground state. Thus, the *anti–int* isomerization would be more difficult than the *int–syn* isomerization in the excited state.

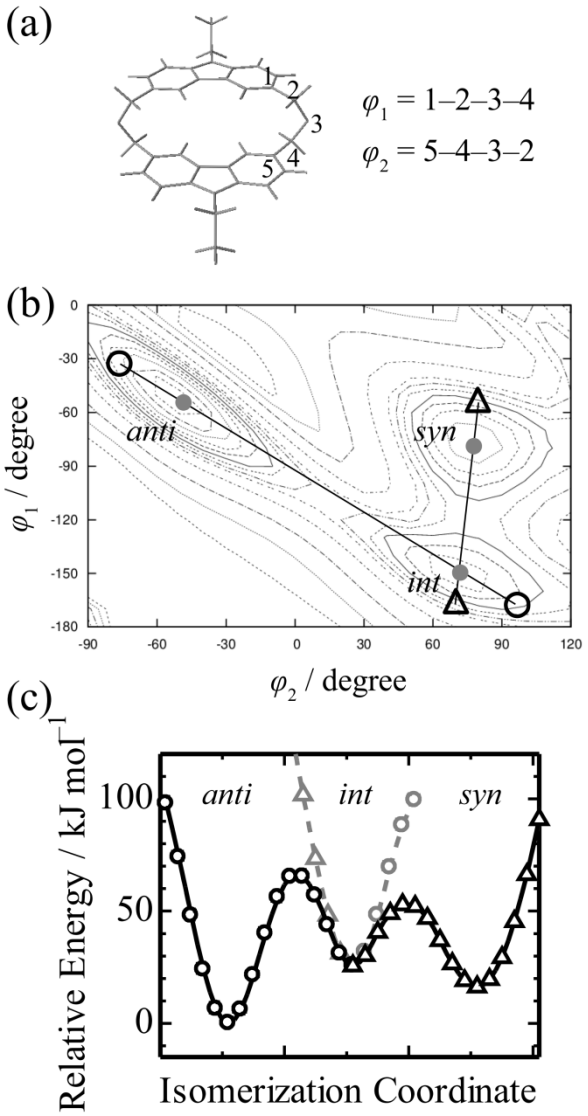

Figure 3-6. (a) Definition of the dihedral angles φ_1 and φ_2. The dihedral angles in the opposite side, φ_1' and φ_2', are assumed to be the same as φ_1 and φ_2, respectively. (b) Potential energy surface of CzOCz in the ground state as a function of the dihedral angles φ_1 and φ_2 calculated by using generalized AMBER force field (gaff). Three local potential minima, *anti*-, *int*-, and *syn*-conformations are marked as ●. (c) Potential energy curves along the solid lines in the panel (b).

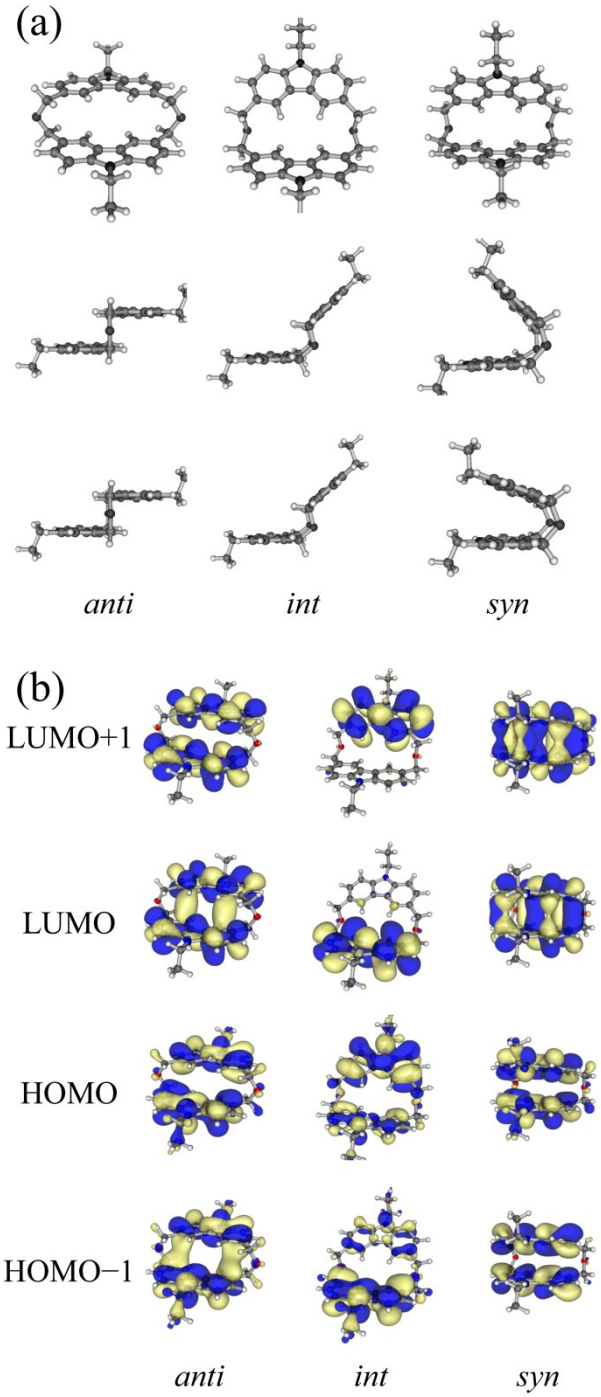

Figure 3-7. (a) Optimized structures of CzOCz isomers in the ground (the first and second rows), and excited state (the third row) calculated with the (TD-)DFT/CAM-B3LYP level at the 6-31G(d,p) basis set. (b) Relevant molecular orbitals HOMO−1, HOMO, LUMO, and LUMO+1 in CzOCz isomers calculated with the TD-DFT/CAM-B3LYP level at the 6-31G(d,p) basis set.

Next, the optimized structures of these three stable CzOCz isomers in the ground (excited) states was calculated by (time-dependent) density functional theory ((TD-)DFT) at the (TD-)DFT/CAM-B3LYP level with the 6-31G(d,p) basis set.[52,53] For *anti*-CzOCz and *int*-CzOCz, as shown in Figure 3-7a, no distinct difference in the conformation is observed between the ground and excited state. For *syn*-CzOCz, the interchromophoric distance is shorter in the excited state than in the ground state, resulting from the attractive interchromophoric interaction in the excited state. Figure 3-7b shows the relevant molecular orbitals of these three CzOCz isomers in the excited state. The main configurations of the lowest excited state for *anti*- and *syn*-CzOCz correspond to the highest occupied molecular orbital to the lowest unoccupied molecular orbital (HOMO to LUMO) transition, and that for *int*-CzOCz corresponds to a mixture of the HOMO−1 to LUMO and the HOMO to LUMO transitions. In the *anti*-CzOCz, the HOMO to LUMO transition mainly corresponds to the intrachromophore transition in each carbazole chromophore, suggesting negligible interchromophoric interaction. In the *syn*-CzOCz, on the other hand, the LUMO is symmetrically delocalized over two carbazole chromophores, suggesting considerable interchromophoric interaction. Interestingly, the molecular orbitals in the *int*-CzOCz are distributed asymmetrically between two carbazole chromophores: the HOMO and LUMO+1 are localized onto one carbazole ring and the HOMO−1 and LUMO are localized onto another ring. Thus, the HOMO−1 to LUMO transition corresponds to the intrachromophore transition in the one carbazole chromophore, which is ascribed to the local excitation in the *int*-CzOCz. The HOMO to LUMO transition corresponds to the interchromophore transition from one carbazole to the other carbazole chromophore, which is ascribed to the CT excitation in the *int*-CzOCz as will be discussed later.

Table 3-3. Vertical Transition Energies and Energy Difference Calculated.

	$E_{vert,\ anti}$ (kJ mol^{-1})	$E_{vert,\ syn}$ (kJ mol^{-1})	ΔE_{ai} (kJ mol^{-1})	ΔE_{as} (kJ mol^{-1})
Vaccum	415 (4.30)	345 (3.57)	−1.8	−15.1
in MeCN	411 (4.26)	348 (3.61)	−8.8	−16.2
in THF	412 (4.27)	348 (3.60)	−6.7	−15.0

The vertical transition energies in parenthesis are in eV scale.

To compare the relative stability in these three CzOCz isomers, the energy difference between the optimized isomers in the excited state ΔE was calculated. In contrast to the ground state, the *anti*-conformation is the most unstable in the excited state, suggesting the attractive interaction between two carbazole rings in the *int*- and *syn*-conformations in the excited state. As summarized in Table 3-3, the energy difference between the *anti*- and *int*-conformations ΔE_{ai} increases from −1.8 to −8.8 kJ mol^{-1} with increasing surrounding polarity. On the other hand, the energy difference between the *anti*- and *syn*-conformations ΔE_{as} remains the same at ~−15 kJ mol^{-1} independently of the surrounding polarity. This polarity dependence indicates that the *int*-CzOCz has a CT character in the excited state while the *syn*-CzOCz in the excited state is rather neutral as will be discussed later. It is noteworthy that the vertical excitation energy from the ground to the excited state E_{vert} for *anti*- and *syn*-conformations is independent of the surrounding polarity, which is consistent with the polarity-independent emission mentioned above.

Scheme 3-1. Kinetic Scheme for the Intramolecular Excimer Formation.

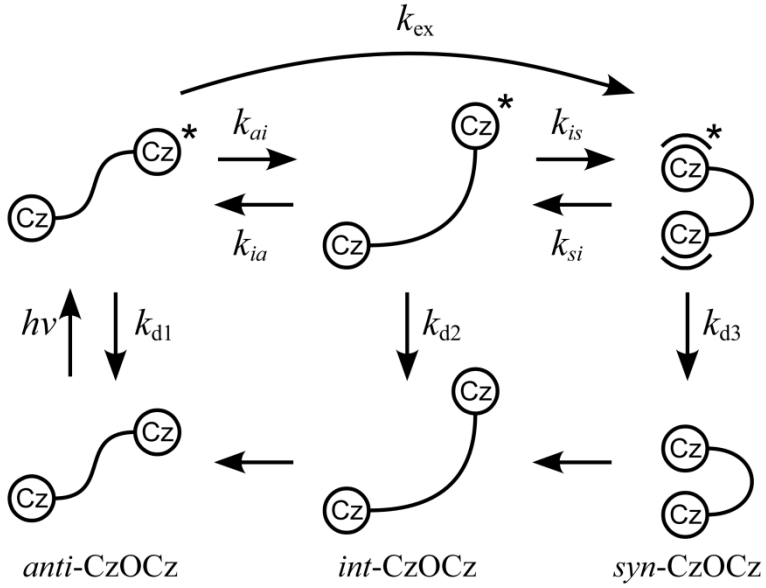

The rate constants k_{d1}, k_{d2}, and k_{d3} are due to radiative and non-radiative monomolecular deactivations of *anti*-, *int*-, and *syn*-CzOCz, respectively. The rate constants k_{ai}, k_{is}, k_{ia}, and k_{si} represent the association and dissociation rates of the intramolecular excimer, respectively. The rate constant k_{ex} represents the apparent excimer formation rate of the intramolecular excimer.

3.3. Discussion

3.3.1. Kinetics of the Intramolecular Excimer Formation. In order to analyze the formation dynamics of intramolecular excimer in CzOCz, the author proposes the kinetic scheme as shown in Scheme 3-1. Thus, the rate equations are described by Eq. 3-1

$$\begin{aligned} \frac{dA(t)}{dt} &= -k_{d1}A(t) - k_{ai}A(t) + k_{ia}I(t) \\ \frac{dI(t)}{dt} &= -k_{d2}I(t) + k_{ai}A(t) - k_{ia}I(t) - k_{is}I(t) + k_{si}S(t) \\ \frac{dS(t)}{dt} &= -k_{d3}S(t) + k_{is}I(t) - k_{si}S(t) \end{aligned} \qquad (3\text{-}1)$$

where $A(t)$, $I(t)$, and $S(t)$ are the density of the *anti*-, *int*-, and *syn*-CzOCz in the excited state at a delay time t after the laser excitation, k_{d1}, k_{d2}, and k_{d3} are the rate constants of the radiative and non-radiative deactivations in the *anti*-, *int*-, and *syn*-CzOCz, respectively, and k_{ai}, k_{is}, k_{ia}, and k_{si} are the isomerization rate constants in the excited state. On the basis of the energy difference calculated above, it can be safely said that $k_{ai} >> k_{ia}$ and $k_{is} >> k_{si}$, which is consistent with the single

exponential decay of the monomer emission in CzOCz. Furthermore, it can be set that $k_{ai} << k_{is}$ because $I(t) \approx 0$: no observation of the *int*-CzOCz in the time-resolved fluorescence and transient absorption measurements. In other words, the *anti–int* isomerization is the rate-limiting process for the excimer formation in CzOCz. This is probably because the *anti–int* isomerization requires a cooperative rotation in both angles φ_1 and φ_2 while the *int–syn* isomerization requires the φ_1 rotation alone as mentioned above. Under these conditions, $A(t)$ and $S(t)$ are simply described by Eq. 3-2 (details are described in the Appendix).

$$A(t) = A_0 \exp[-(k_{\mathrm{d1}}+k_{ai})t]$$
$$S(t) = \frac{k_{ai}}{k_{\mathrm{d1}} + k_{ai} - k_{\mathrm{d3}}} A_0\{\exp(-k_{\mathrm{d3}}t) - \exp[-(k_{\mathrm{d1}}+k_{ai})t]\} \quad (3\text{-}2)$$

Therefore, the apparent excimer formation rate constant can be considered to be the same as $k_{ai} = 1/\tau_{\mathrm{mono}} - k_{\mathrm{d1}}$. Assuming that k_{d1} is the same as the decay rate constant of the CzOMe, k_{ai} is described as $k_{ai} \approx 1/\tau_{\mathrm{mono}} - 1/\tau_{\mathrm{f}}^0 = k_{\mathrm{ex}}$ where τ_{f}^0 is the fluorescence lifetime of the CzOMe. Thus, the k_{ex} and E_{iso} evaluated above corresponds to the rate constant and the activation energy for the *anti–int* isomerization, respectively. Therefore it is concluded that the efficient excimer formation in polar solutions is attributed to the reduction in the potential barrier for the *anti–int* isomerization of CzOCz in the excited state.

Scheme 3-2. Schematic illustration of Potential Curve for Intramolecular Excimer Formation.

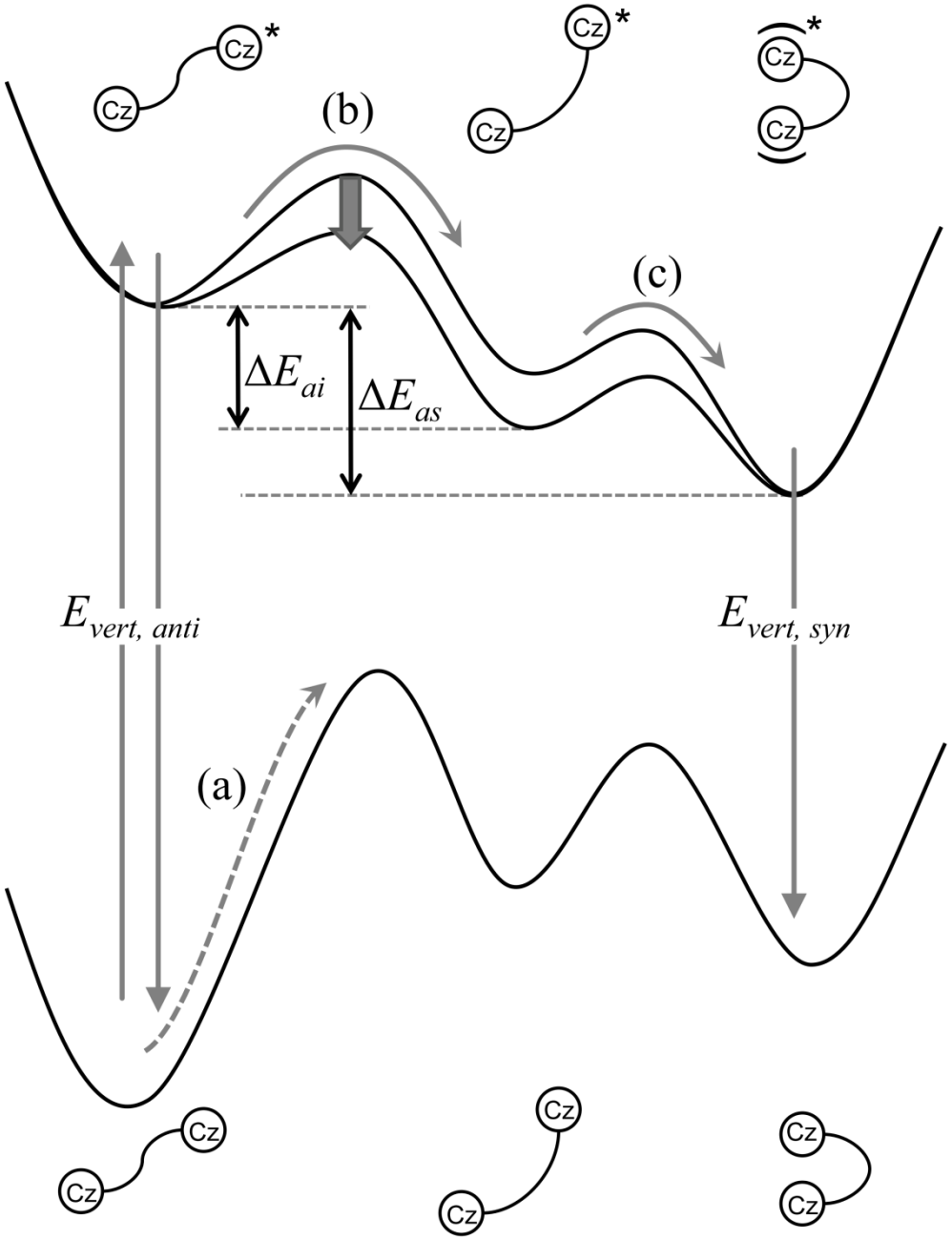

The *anti–int* isomerization is negligible in the ground state because of high potential barrier (a). In contrast, the potential barrier in the excited state is much lower than that in the ground state, and hence the isomerization easily undergoes (b). Because the potential barrier becomes lower in polar solutions, the *int*-conformation is formed more efficiently in polar solutions. Once, the *int*-conformation is formed, the subsequent isomerization from the *int*- to *syn*-conformation undergoes immediately because of lower potential barrier (c).

Scheme 3-3. Schematic illustration of Excited State Configurations for CzOCz Isomers.

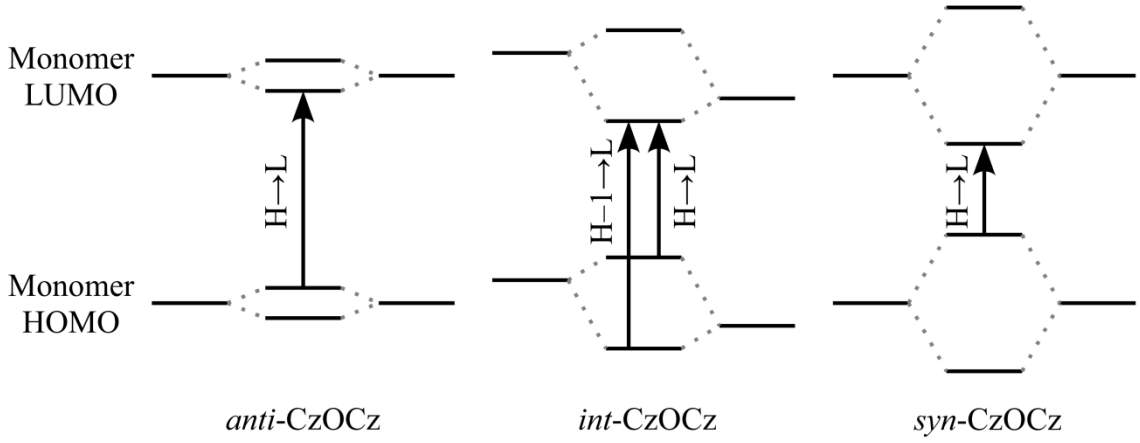

Ground state: Both bonding and anti-bonding orbitals are filled with electrons, and hence favorable and unfavorable orbital interaction is canceled out in the dimer state. Rather, the repulsive interchromophore interaction increases as two carbazole rings are approaching. As a result, the *anti*-conformation is the most stable because of the smallest ring overlap.
Excited state: In the dimer state, the favorable interaction is enhanced by the HOMO–LUMO transition. The stabilization energy is dependent on the interchromophore interaction in CzOCz. Thus, *syn*-CzOCz is the most stable and *anti*-CzOCz is the most unstable.

3.3.2. Excimer Formation Mechanism. On the basis of the kinetic analysis described above, the intramolecular excimer formation in CzOCz can be summarized as shown in Scheme 3-2. In the ground state, the *anti*-conformation is more stable than the *int*- and *syn*-conformations. This is because both bonding and anti-bonding orbitals are filled with electrons in the ground state and hence favorable and unfavorable orbital interaction is canceled out in the dimer geometry. Rather, the repulsive interchromophoric interaction increases as two carbazole rings are approaching in the ground state. As a result, the *anti*-conformation is the most stable because of the smallest ring overlap. As shown in Figure 3-6c, the potential barrier from the *anti*- to *int*-CzOCz is so high that the *anti–int* isomerization is negligible (arrow a): only *anti*-CzOCz exists in the ground state. In contrast, the *anti*-conformation is the most unstable in the excited state as summarized in Table 3-3, suggesting that the attractive interaction between two carbazole rings in the *int*- and *syn*-conformations is considerably large in the excited state. As summarized in Scheme 3-3, the main

configurations of the lowest excited state correspond to the HOMO–LUMO transition for *anti*- and *syn*-CzOCz and a mixture of the HOMO–LUMO and HOMO−1–LUMO transitions for *int*-CzOCz. In the dimer geometry, the favorable interaction is enhanced by the HOMO–LUMO transition. In other words, the HOMO–LUMO transition is the major origin of the stabilization in the excited state for all the three conformations in CzOCz. On the other hand, the stabilization energy is dependent on the interchromophoric interaction in CzOCz, which is most sensitive to the interchromophoric distance. Thus, *syn*-CzOCz is the most stable and *anti*-CzOCz is the most unstable in the excited state.[9–14,54] The stabilization of *int*-CzOCz in the excited state leads to the decrease in the potential barrier, resulting in the efficient *anti–int* isomerization (arrow b). Once *anti*-CzOCz converts to *int*-CzOCz, it immediately further converts to *syn*-CzOCz, because the *int–syn* isomerization rate is much larger than the *anti–int* isomerization rate as mentioned above (arrow c). The *int*-CzOCz in polar solutions is more stable because of the CT character in the excited state, resulting in the lower potential barrier for the *anti–int* isomerization. Thus, the *anti–int* isomerization is more efficient in polar solutions. Therefore it is concluded that the CT character of the *int*-CzOCz in the excited state is a key determinant for the solvent-polarity-induced intramolecular excimer formation.

3.3.3. Origin of the CT Character of *int*-CzOCz. The author finally discusses the origin of the CT character even in a homodimer with two carbazole groups. Intramolecular CT in the dimer of identical chromophores was first reported for 1,2-di(1-anthryl)ethane in polar solutions by Mataga et al.[18,19,55–58] They found that anthracene radical cation and anion are formed first because of strong intramolecular CT character and then intramolecular excimer is formed by recombination of the CT state.[18,19] The energy level of the CT state in 1,2-di(1-anthryl)ethane is estimated to be lower than that of the LE state, and hence the CT character is large. In this case, the energy level of the CT state in the *anti*-CzOCz in an MeCN solution is estimated to be 4.2 eV, which is 0.6 eV higher than that of the LE state (details are described in the Appendix),[12,34,46,59,60] and hence mixing of the CT state and the LE state would be negligibly small in the *anti*-conformation. This is in good agreement

with the solvent-polarity independent monomer emission band. Thus, the conformation of the *int*-CzOCz is probably important to the CT character. Because of the edge-to-face geometry in the *int*-CzOCz, the facial and axial carbazole rings are energetically not equivalent. This is in contract to the symmetrical geometry in the *anti*- and *syn*-CzOCz. Consequently, as shown in Figure 3-7b, the molecular orbitals are distributed asymmetrically between two carbazole rings in the *int*-CzOCz, which would be helpful to mix the CT state with the LE state.[61] Therefore it is concluded that the asymmetrical edge-to-face geometry is a key determinant of the CT character in the *int*-CzOCz in the excited state.

3.4. Conclusions

In this chapter, solvent-polarity-induced formation dynamics of the intramolecular excimer in CzOCz has been studied by time-resolved spectroscopic methods and computational calculations. In the ground state, the stacking mode of two carbazole rings is the *anti*-conformation, and the isomerization from the *anti*- to *syn*-CzOCz is negligible because of large activation energy. In contrast, in the excited state, the potential barrier for the isomerization is much lower than that in the ground state and becomes lower in polar solutions. Because the *anti–int* isomerization requires the cooperative rotation both in φ_1 and φ_2 while the *int–syn* isomerization is almost dependent on the φ_1 rotation alone, the rate-limiting process of the excimer formation is the *anti–int* isomerization, and hence the potential barrier for the isomerization E_{iso} corresponds to the activation energy for the *anti–int* isomerization. Owing to the favorable orbital interaction between the two carbazole rings, the *int*-CzOCz becomes more stable compared to the *anti*-CzOCz in the excited state. This stabilization leads to the decrease in the potential barrier in the excited state. The *int*-CzOCz in polar solutions is more stable because of the CT character in the excited state, resulting in efficient *anti–int* isomerization in polar solutions. Therefore it is concluded that the efficient excimer formation in polar solvents is attributed to the CT character of the *int*-CzOCz in the excited state. Because of the edge-to-face geometry in the *int*-CzOCz, the facial and axial carbazole rings are energetically not

equivalent. Consequently, the molecular orbitals are distributed asymmetrically between two carbazole rings in *int*-CzOCz, which would be helpful to mix the CT state to the LE state. Therefore it is concluded that the asymmetrical edge-to-face geometry is a key determinant of the CT character in the *int*-CzOCz in the excited state.

3.5. Experimental Section

Materials. Dioxa[3.3](3,6)carbazolophane (CzOCz) was synthesized by the cyclization reaction between 3,6-bis(hydroxymethyl)carbazole and 3,6-bis(bromomethyl)carbazole, and was purified by alumina chromatography and recrystallization. As a reference, 3,6-bis(methoxymethyl)carbazole (CzOMe) was also prepared. Details of the synthesis have been described elsewhere.[44] Solvents used in this study were acetonitrile (MeCN, Wako, spectroscopic grade), *N,N*-dimethyl formamide (DMF, Nacalai Tesque, spectroscopic grade), and tetrahydrofuran (THF, Wako, spectroscopic grade). These solvents were used without further purification.

Measurements. Absorption and photoluminescence spectra were measured at room temperature in a 1-cm quartz cell with a UV–visible spectrophotometer (Hitachi, U-3500) and a fluorescence spectrophotometer (Hitachi, F-4500) equipped with a red-sensitive photomultiplier (Hamamatsu, R928F), respectively. Photoluminescence decay was measured by the time-correlated single-photon-counting (TCSPC) method (Horiba Jobin Yvon, FluoroCube). The excitation wavelength was 296 nm. The total instrument response function is an FWHM of ca. 800 ps. Transient absorption data were collected with a pump and probe femtosecond transient spectroscopy system. This system consists of a transient absorption spectrometer (Ultrafast Systems, Helios) and a regenerative amplified Ti:sapphire laser (Spectra-Physics, Hurricane). The amplified Ti:sapphire laser provided 800 nm fundamental pulses at a repetition rate of 1 kHz with a power of 0.9 mJ and a pulse width of 100 fs (FWHM), which were split into two optical beams with a beam splitter to generate pump and probe pulses. One fundamental beam was converted into pump pulses at 350 nm with an ultrafast optical parametric amplifier (Spectra-Physics, TOPAS). The other fundamental beam was converted into white light pulses employed as probe pulses in the wavelength region from 400 to 1700 nm. The pump pulses were modulated mechanically with a repetition rate of 500 Hz. The temporal evolution of the probe intensity was recorded with a CMOS linear sensor (Ultrafast Systems, SPEC-VIS) for the visible measurement and with an InGaAs linear diode array sensor (Ultrafast Systems, SPEC-NIR) for the near-IR measurement. The transient absorption spectra and

decays were collected over the time range from −5 ps to 3 ns. Typically, 2500 laser shots were averaged at each delay time to obtain a detectable absorbance change as small as ~10^{-4}. In order to cancel out orientation effects on the dynamics, the polarization direction of the linearly polarized probe pulse was set at a magic angle of 54.7 ° with respect to that of the pump pulse. Samples were degassed by Ar bubbling for 30 min. The concentration of carbazole compounds was in the order of 10^{-4} mol L^{-1} for the transient absorption measurements and 10^{-5} mol L^{-1} for the other measurements. Note that the transient absorption spectra and dynamics were highly reproducible even after the several times measurements. In other words, the laser irradiation had negligible effects on the sample degradation at least under this experimental condition.

Calculations. Gas-phase molecular mechanics calculations of the CzOCz were performed with AMBER10.[51] The CzOCz was assigned to gaff atom types and AM1-BCC charges by using the antechamber module. The molecular structure in the *anti*-, *int*-, and *syn*-conformations was energy-minimized with the sander module. Owing to the reversal symmetry in CzOCz, the dihedral angles in the opposite side, φ_1' and φ_2', can be assumed to be equal to φ_1 and φ_2, respectively. As a function of the dihedral angles φ_1 and φ_2, conformational energy was determined from minimization by applying a very strong harmonic potential around the value of each dihedral angle. All quantum chemical calculations were carried out using Gaussian 09.[52] The ground state optimizations were carried out using the density functional theory (DFT) methods with the CAM-B3LYP functional, which is a long-distance corrected functional, at the 6-31G(d,p) basis set. The excited state optimizations were carried out using time-dependent DFT (TD-DFT) methods with the same level. The effect of solvent environment was simulated using the polarizable continuum model (PCM).[53] The state-specific solvation of vertical transitions (absorption and emission) was accomplished using a procedure described in the g09 manual.[52] Molecular orbitals were visualized by using Molekel 5.4.[62]

3.6. Appendix

3.6.1. Transient Absorption Decays. Figure 3-A1 shows the transient absorption decays of CzOCz in an MeCN solution measured at 640 (open circles), and 930 (open triangles) nm. As mentioned in the manuscript, the visible absorption band at around 640 nm is due to the superposition of the $S_n \leftarrow S_1$ absorption of *anti*-CzOCz and the LE band of *syn*-CzOCz. The $S_n \leftarrow S_1$ absorption of *anti*-CzOCz is almost the same as the LE band of *syn*-CzOCz, and hence the *anti*–*syn* isomerization has no impact on the absorption signal in this wavelength region. Thus, the absorption decay was fitted with a single exponential function with a time constant of ~11 ns. This value is in good agreement with the fluorescence lifetime of the CzOCz excimer evaluated by the TCSPC method except for the slight shortness due to the limited time window. The near-IR absorption band at around 930 nm has been ascribed to the charge transfer (CT) band of carbazole excimer.[34] The time evolution of the CT band was fitted with the sum of two exponential functions in which the longer time constant was fixed at 11 ns. The shorter time constant (rise component) was estimated to be ~1.2 ns, which is in good agreement with the rise time constant of the excimer fluorescence evaluated by the TCSPC method.

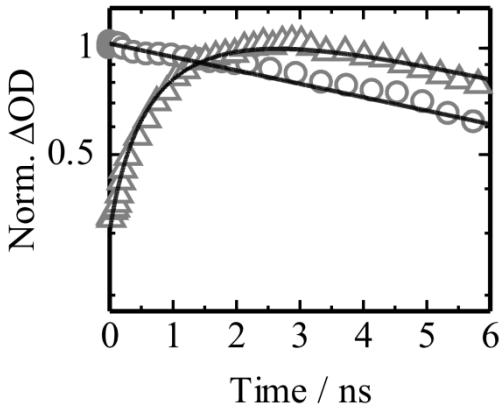

Figure 3-A1. Transient absorption decays of CzOCz in an MeCN solution measured at 640 (open circles), and 930 (open triangles) nm. The excitation wavelength (fluence) was 350 nm (~30 μJ cm^{-2}). The solid lines represent the fitting curves with one (640 nm) or two (930 nm) exponential functions.

3.6.2. Kinetics of the Intramolecular Excimer Formation. The density of *anti*- and *int*-CzOCz in the excited state at a delay time *t* after the laser excitation, $A(t)$ and $S(t)$, is described by Eq. 3-A1.

$$A(t) = A_0 \exp[-(k_{d1}+k_{ai})t]$$
$$S(t) = \frac{k_{ai}}{k_{d1} + k_{ai} - k_{d3}} A_0\{\exp(-k_{d3}t) - \exp[-(k_{d1}+k_{ai})t]\} \quad \text{(3-A1)}$$

Here, the author briefly sketches the derivation of these equations. The kinetics of the intramolecular excimer formation in CzOCz is represented as shown in Scheme 3-1. The rate equations are described by Eq. 3-A2

$$\frac{dA(t)}{dt} = -k_{d1}A(t) - k_{ai}A(t) + k_{ia}I(t) \; D = \eta\left(\frac{4\pi\rho}{3}\right)^{4/3} \frac{R_0^6}{\tau} \quad \text{(3-A2-1)}$$

$$\frac{dI(t)}{dt} = -k_{d2}I(t) + k_{ai}A(t) - k_{ia}I(t) - k_{is}I(t) + k_{si}S(t) \quad \text{(3-A2-2)}$$

$$\frac{dS(t)}{dt} = -k_{d3}S(t) + k_{is}I(t) - k_{si}S(t) \quad \text{(3-A2-3)}$$

where $I(t)$ is the density of *int*-CzOCz. Under the equilibrium condition, the ratio of the density of *anti*-, and *int*-CzOCz, $A/I_{t\to\infty}$ can be expressed as $A/I_{t\to\infty} = k_{ia}/k_{ai}$. Assuming the Boltzmann distribution, k_{ia}/k_{ai} is described as Eq. 3-A3

$$\frac{k_{ia}}{k_{ai}} = \exp\left(-\frac{E_{ai}}{RT}\right) \quad \text{(3-A3)}$$

where E_{ai} is the energy difference between the *anti*- and *int*-CzOCz. Using the energy gap between *anti*- and *int*-CzOCz estimated by the TD-DFT calculation, k_{ia}/k_{ai} is estimated to be <<1 at room temperature regardless of the solvent polarity, indicating that back-isomerization from the *int*- to *anti*-conformation is negligible at room temperature. This is consistent with the observation that the fluorescence decay of the LE emission can be fitted with a single exponential function as shown in Figure 3-3. Therefore, the third term in Eq. 3-A2-1 (and also the third term in Eq. 3-A2-2) is negligible, and hence $A(t)$ can be solved as Eq. 3-A1. Assuming the steady-state approximation to the *int*-CzOCz, $I(t)$ can be described as Eq. 3-A4

$$I(t) = \frac{k_{ai}A(t) + k_{si}S(t)}{k_{is} + k_{d2}} \quad \text{(3-A4)}$$

Because there is no indication of the *int*-CzOCz in the time-resolved fluorescence and transient absorption measurements, $I(t)$ can be assumed to be ~0, indicating that the denominator of the right hand side in Eq. 3-A4 is much larger than the numerator. According to the time-resolved fluorescence spectra as shown in Figure 3-A1, k_{d2} must be small, therefore the following equation can be obtained.

$$I(t) = \frac{k_{ai}}{k_{is}} A(t) + \frac{k_{si}}{k_{is}} S(t) \approx 0 \qquad \text{(3-A5)}$$

In analogy with the relationship between the *anti*- and *int*-conformation, $k_{si}/k_{is} << 1$ is obvious. An important conclusion is that $k_{ai}/k_{is} << 1$ in other words, the rate-limiting process is the *anti–int* isomerization. This result is reasonable because the *anti–int* isomerization requires cooperative rotation of the dihedral angle φ_1 and φ_2, while the *int–syn* isomerization requires only slight φ_2 change during the φ_1 rotation as shown in Figure 3-6a. Substituting Eq. 3-A5 into Eq. 3-A2-3, $A(t)$ is solved as Eq.3-A1. The above discussion indicates that the kinetics of intramolecular excimer formation in CzOCz is equivalent to the simplified scheme 3-A1. Therefore, the apparent excimer formation rate k_{ex} can be considered to be equal to the association rate k_{ai}.

Scheme 3-A1. Simplified Kinetic Scheme of Intramolecular Excimer Formation in CzOCz.

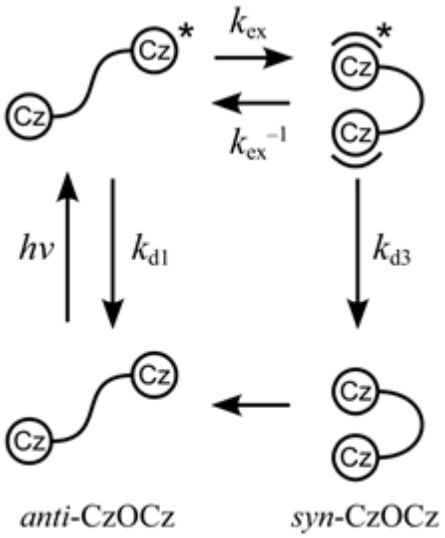

3.6.2. Kinetics of the Intramolecular Excimer Formation. The energy level of the radical ion pair state ($Cz^+ + Cz^-$) E(RIP) is approximately estimated by Eq. 3-A6.

$$E(\mathrm{RIP}) = IP - EA + C(r) \tag{3-A6}$$

Here IP and EA are the ionization potential and the electron affinity of the monomer, respectively. The Coulomb interaction between the cation and anion $C(r)$ can be estimated by

$$C(r) = -\frac{e^2}{4\pi\varepsilon_0\varepsilon_r r} \tag{3-A7}$$

where e is the elementary charge, ε_0 is the vacuum permittivity, ε_r is a dielectric constant of the medium, and r is a separation distance between the cation and anion. The value of $IP - EA$ in the polar medium was estimated by using Eq. 3-A8, because it is different from that in vacuum $IP_g - EA_g$ because of the polarization energy induced by the cation and anion $P_{\pm}$.[60]

$$IP - EA = IP_g - EA_g + P_+ + P_- \tag{3-A8}$$

The polarization energy P can be estimated by Born's formula,[63]

$$P = P_+ = P_- = -\frac{e^2}{8\pi\varepsilon_0 R}\left(1 - \frac{1}{\varepsilon_r}\right) \tag{3-A9}$$

where R is the effective radius of the ion. Born's formula has been reported to give reasonable values when the van der Waals radius R_{vdW} is used as the effective radius R of the ion.[64,65] Parameters used in the evaluation of E(RIP) are IP_g = 7.8 eV,[46,59,60] EA_g = 0 eV,[46,59,60] ε_r = 37.5 (MeCN), R = 3.75 Å, and the center-to-center distance between two carbazole rings in the *anti*-CzOCz of 4.8 Å was used as the separation distance between ions r in Eq. 3-A7. This gives E(RIP) = 4.0 eV. The energy level of the CT state in the dimer configuration is assumed to be 0.2 eV higher than that of a radical ion pair state,[66] resulting in E(CT) = 4.2 eV.

References

(1) Yanari, S. S.; Bovey, F. A.; Lumry, R. *Nature* **1963**, *200*, 242–244.

(2) Hirayama, F. *J. Chem. Phys.* **1965**, *42*, 3163–3171.

(3) Chandross, E. A.; Dempster, C. J. *J. Am. Chem. Soc.* **1970**, *92*, 3586−3593.

(4) Klöpffer, W. *Chem. Phys. Lett.* **1969**, *4*, 193−194.

(5) Klöpffer, W. *J. Chem. Phys.* **1969**, *50*, 2337−2343.

(6) Ito, S.; Yamamoto, M.; Nishijima, Y. *Bull. Chem. Soc. Jpn.* **1981**, *54*, 35−40.

(7) Ito, S.; Yamamoto, M.; Nishijima, Y. *Bull. Chem. Soc. Jpn.* **1982**, *55*, 363−368.

(8) Ito, S.; Takami, K.; Tsujii, Y.; Yamamoto, M. *Macromolecules* **1990**, *23*, 2666−2673.

(9) Birks, J. B. *Photophysics of Aromatic Molecules*; Wiley-Interscience: London, 1970; Chapter 7.

(10) Birks J. B. *Rep. Prog. Phys*. **1975**, *38*, 903–974.

(11) Azumi, T.; Armstrong, A. T.; McGlynn, S. P. *J. Chem. Phys.* **1964**, *41*, 3839–3852.

(12) Katoh, R.; Sinha, S.; Murata, S.; Tachiya, M. *J. Photochem. Photobiol., A* **2001**, *145*, 23–34.

(13) Amicangelo, J. C. *J. Phys. Chem. A* **2005**, *109*, 9174–9182.

(14) Shirai, S.; Iwata, S.; Tani, T.; Inagaki, S. *J. Phys. Chem. A* **2011**, *115*, 7687–7699.

(15) Lim, E. C. *Acc. Chem. Res.* **1987**, *20*, 8−17.

(16) East, A. L. L.; Lim, E. C. *J. Chem. Phys.* **2000**, *113*, 8981−8994.

(17) Terazima, M.; Cai, J.; Lim. E. C. *J. Phys. Chem. A* **2000**, *104*, 1662−1669.

(18) Mataga, N.; Yao, H.; Okada, T. *Tetrahedron* **1989**, *45*, 4683–4692.

(19) Yao, H.; Okada, T.; Mataga, N. *J. Phys. Chem.* **1989**, *93*, 7388–7394.

(20) Mataga, N.; Chosrowjan, H.; Taniguchi, S. *J. Photochem. Photobiol., C* **2005**, *6*, 37–79.

(21) Cram, D. J.; Cram, J. M. *Acc. Chem. Res.* **1971**, *4*, 204–213.

(22) Cram, D. J.; Allinger, N. L.; Steinberg, H. *J. Am. Chem. Soc.* **1954**, *76*, 6132–6141.

(23) Vala, M. T.; Hillier, I. H.; Rice, S. A.; Jortner, J. *J. Chem. Phys.* **1966**, *44*, 23–35.

(24) Hillier, I. H.; Glass, L.; Rice, S. A. *J. Chem. Phys.* **1966**, *45*, 3015–3021.

(25) Longworth, J. W.; Bovey, F. A. *Biopolymers* **1966**, *4*, 1115–1129.

(26) Froines, J. R.; Hagerman, P. J. *Chem. Phys. Lett.* **1969**, *4*, 135–138.

(27) Yanagidate, M.; Takayama, K.; Takeuchi, M.; Nishimura, J.; Shizuka, H. *J. Phys. Chem.* **1993**, *97*, 8881–8888.

(28) Morita, M.; Kishi, T.; Tanaka, M.; Tanaka, J.; Ferguson, J.; Sakata, Y.; Misumi, S.; Hayashi, T.; Mataga, N. *Bull. Chem. Soc. Jpn.* **1978**, *51*, 3449–3457.

(29) Nakamura, Y.; Tsuihiji, T.; Mita, T.; Minowa, T.; Tobita, S.; Shizuka, H.; Nishimura, J. *J. Am. Chem. Soc.* **1996**, *118*, 1006–1012.

(30) Nakamura, Y.; Kaneko, M.; Yamanaka, N.; Tani, K.; Nishimura, J. *Tetrahedron Lett.* **1999**, *40*, 4693–4696.

(31) Tani, K.; Tohda, Y.; Takemura, H.; Ohkita, H.; Ito, S.; Yamamoto, M. *Chem. Commun.* **2001**, 1914–1915.

(32) Ohkita, H.; Ito, S.; Yamamoto, M.; Tohda, Y.; Tani, K. *J. Phys. Chem. A* **2002**, *106*, 2140–2145.

(33) Benten, H.; Ohkita, H.; Ito, S.; Yamamoto, M.; Sakumoto, N.; Hori, K.; Tohda, Y.; Tani, K.; Nakamura, Y.; Nishimura, J. *J. Phys. Chem. B* **2005**, *109*, 19681–19687.

(34) Benten, H.; Guo, J.; Ohkita, H.; Ito, S.; Yamamoto, M.; Sakumoto, N.; Hori, K.; Tohda, Y.; Tani, K. *J. Phys. Chem. B* **2007**, *111*, 10905–10914.

(35) Tani, K.; Sakumoto, N.; Kubono, K.; Hori, K.; Tohda, Y.; Benten, H.; Ohkita, H.; Ito, S.; Yamamoto, M. *Chem. Lett.* **2009**, *38*, 140–141.

(36) Griffin Jr., R. W.; Coburn, R. A. *J. Am. Chem. Soc.* **1967**, *89*, 4638–4641.

(37) Sorimachi, K.; Morita, T.; Shizuka, H. *Bull. Chem. Soc. Jpn.* **1974**, *47*, 987–990.

(38) Shizuka, H.; Ogiwara, T.; Morita, T. *Bull. Chem. Soc. Jpn.* **1975**, *48*, 3385–3386.

(39) Hayashi, T.; Mataga, N.; Sakata, Y.; Misumi, S. *Chem. Phys. Lett.* **1976**, *41*, 325–328.

(40) Hayashi, T.; Mataga, N.; Umemoto, T.; Sakata, Y.; Misumi, S. *J. Phys. Chem.* **1977**, *81*, 424–429.

(41) Fujise, Y.; Nakasato, Y.; Ito, S. *Tetrahedron Lett.* **1986**, *27*, 2907–2908.

(42) Mitchell, R. H.; Vinod, T. K.; Bushnell, G. W. *J. Am. Chem. Soc.* **1990**, *112*, 3487–3497.

(43) Ito, S.; Nakasato, Y.; Hioki, H.; Nagaku, M.; Kan, Y.; Fukazawa, Y. *Tetrahedron Lett.* **1993**, *34*, 3789–3792.

(44) Tani, K.; Tohda, Y.; Hisada, K.; Yamamoto, M. *Chem. Lett.* **1996**, 145–146.

(45) Johnson, G. E. *J. Phys. Chem.* **1974**, *78*, 1512–1521.

(46) Johnson, G. E. *J. Chem. Phys.* **1975**, *62*, 4697−4709.

(47) Bonesi, S. M.; Erra-Balsells, R. *J. Lumin.* **2001**, *93*, 51–74.

(48) Loughnane, B. J.; Scodinu, A.; Farrer, R. A.; Fourkas, J. T.; Mohanty, U. *J. Chem. Phys.* **1999**, *111*, 2686–2694.

(49) Szwarc, M. *Carbanions Living Polymers and Electron Transfer Processes*; Interscience, N.Y., 1968

(50) Masuhara, H.; Tamai, N.; Mataga, N.; De Schryver, F. C.; Vandendriessche, J.; Boens, N. *Chem. Phys. Lett.* **1983**, *95*, 471–475.

(51) AMBER10, Case, D. A.; Darden, T. A.; Cheatham, III, T. E.; Simmerling, C. L.; Wang, J.; Duke, R. E.; Luo, R.; Crowley, M.; Walker, R. C.; Zhang, W.; Merz, K. M.; Wang, B.; Hayik, S.; Roitberg, A.; Seabra, G.; Kolossváry, I.; Wong, K. F.; Paesani, F.; Vanicek, J.; Wu, X.; Brozell, S. R.; Steinbrecher, T.; Gohlke, H.; Yang, L.; Tan, C.; Mongan, J.; Hornak, V.; Cui, G.; Mathews, D. H.; Seetin, M. G.; Sagui, C.; Babin, V.; Kollman, P. A. AMBER 10, University of California, San Francisco, 2008.

(52) Gaussian 09, Revision C.01, Frisch, M. J.; Trucks, G. W.; Schlegel, H. B.; Scuseria, G. E.; Robb, M. A.; Cheeseman, J. R.; Scalmani, G.; Barone, V.; Mennucci, B.; Petersson, G. A.; Nakatsuji, H.; Caricato, M.; Li, X.; Hratchian, H. P.; Izmaylov, A. F.; Bloino, J.; Zheng, G.; Sonnenberg, J. L.; Hada, M.; Ehara, M.; Toyota, K.; Fukuda, R.; Hasegawa, J.; Ishida, M.; Nakajima, T.; Honda, Y.; Kitao, O.; Nakai, H.; Vreven, T.; Montgomery, Jr., J. A.; Peralta, J. E.; Ogliaro, F.; Bearpark, M.; Heyd, J. J.; Brothers, E.; Kudin, K. N.; Staroverov, V. N.;

Kobayashi, R.; Normand, J.; Raghavachari, K.; Rendell, A.; Burant, J. C.; Iyengar, S. S.; Tomasi, J.; Cossi, M.; Rega, N.; Millam, J. M.; Klene, M.; Knox, J. E.; Cross, J. B.; Bakken, V.; Adamo, C.; Jaramillo, J.; Gomperts, R.; Stratmann, R. E.; Yazyev, O.; Austin, A. J.; Cammi, R.; Pomelli, C.; Ochterski, J. W.; Martin, R. L.; Morokuma, K.; Zakrzewski, V. G.; Voth, G. A.; Salvador, P.; Dannenberg, J. J.; Dapprich, S.; Daniels, A. D.; Farkas, Ö.; Foresman, J. B.; Ortiz, J. V.; Cioslowski, J.; Fox, D. J. Gaussian, Inc., Wallingford CT, 2009.

(53) Tomasi, J.; Mennucci, B.; Cammi, R. *Chem. Rev.* **2005**, *105*, 2999–3093.

(54) Huenerbein, R.; Grimme, S. *Chem. Phys.* **2008**, *343*, 362–371.

(55) Nakashima, N.; Murakawa, M.; Mataga, N. *Bull. Chem. Soc. Jpn.* **1976**, *49*, 854–858.

(56) Mataga, N.; Yao, H.; Okada, T.; Rettig, W. *J. Phys. Chem.* **1989**, *93*, 3383–3386.

(57) Mataga, N.; Nishikawa, S.; Okada, T. *Chem. Phys. Lett.* **1996**, *257*, 327–332.

(58) Grabowski, Z. R.; Rotkiewicz, K.; Rettig, W. *Chem. Rev.* **2003**, *103*, 3899–4031.

(59) Sharp, J. H. *J. Phys. Chem.* **1966**, *70*, 584–586.

(60) Katoh, R.; Katoh, E.; Nakashima, N; Yuuki, M.; Kotani, M. *J. Phys. Chem. A* **1997**, *101*, 7725–7728.

(61) Lee, E. C.; Hong, B. H.; Lee, J. Y.; Kim, J. C.; Kim, D.; Kim, Y.; Tarakeshwar, P.; Kim, K. S. *J. Am. Chem. Soc.* **2005**, *127*, 4530–4537.

(62) Varetto, U.; MOLEKEL 5.4.; *Swiss National Supercomputing Centre: Lugano, Switzerland.*

(63) Born, M. *Z. Phys.* **1920**, *1*, 45−48.

(64) Edward, J. T. *J. Chem. Educ.* **1970**, *47*, 261−270.

(65) Katoh, R.; Lacmann, K.; Schmidt, W. F. *Z. Phys. Chem.* **1995**, *190*, 193−201.

(66) Sadygov, R. G.; Lim, E. C. *Chem. Phys. Lett.* **1994**, *225*, 441−447.

Chapter 4

Triplet Exciton Dynamics in Fluorene–Amine Copolymer Films

4.1. Introduction

Triplet exciton dynamics is of particular importance in understanding the electron/photon conversion mechanism in polymer light-emitting diodes (PLEDs) based on fluorescent polymeric materials. Both singlet and triplet excitons are generated by the recombination of an electron and hole carriers injected from electrodes.[1,2] Only singlet excitons contribute to the luminescence in the conventional PLEDs because triplet excitons typically deactivate non-radiatively to the ground state. Thus, the generation yield of singlet excitons is one of the most important factors to determine the device efficiency in PLEDs.[3–5] From simple spin statistics, it is predicted that 25% of singlet excitons and 75% of triplet excitons are generated by the charge recombination. In other words, the internal quantum efficiency (IQE) in PLEDs would be limited to be only 25% at most. However, this limitation can be overcome by singlet exciton regeneration through triplet–triplet annihilation (TTA).[1,2] By considering the singlet exciton regeneration through the TTA, the total singlet exciton generation yield could reach up to 40%.[6,7] Thus, the TTA efficiency is one of the most important photophysical properties for PLEDs.[6–9]

Incorporation of aromatic amines into fluorescent fluorene host materials can remarkably increase both the device efficiency and color stability compared to fluorene homopolymers: either blending a small amount of aromatic amines[10–12] or copolymerizing aromatic amines with fluorenes.[13–15] In the device based on fluorene–amine copolymers, the small amount of aromatic amines acts as not only

hole-trapping[15–18] but also light-emitting site, and hence their chemical structures and incorporation ratio have a critical impact on the device efficiency significantly.[14,15] The contribution of TTA to the device efficiency was studied for a fluorescent PLED based a fluorene–amine copolymer of poly(9,9'-di-*n*-octylfluorene-*ran*-*N*,*N*'-bis(4-*n*-butylphenyl)-*N*,*N*'-diphenyl-1,4-benzenediamine) (F8-PDA).[8] As is discussed in Ref. 8, the delayed fluorescence through TTA contributes to at least 20% of the total emission in the F8-PDA device at a high voltage. However, there are few reports on photophysics in fluorene–amine copolymer films. The relationship between the chemical structure of aromatic amines and the exciton dynamics is not clear yet.

In this chapter, the triplet exciton dynamics in two fluorene–amine random copolymers, F8-PDA and poly(9,9'-di-*n*-octylfluorene-*ran*-*N*,*N*'-bis(4-*t*-butylphenyl)-*N*,*N*'-diphenyl-9,10-anthracenediamine) (F8-ADA) (chemical structures of these copolymers are shown in Figure 4-1) is studied. Exciton dynamics is measured by transient absorption spectroscopy over a wide temporal window from the singlet exciton generation (~1 ps) to the triplet exciton decay (~ms). In this study, the author focuses his attention on the triplet exciton formation through the intersystem crossing (ISC) and the triplet exciton diffusion. Although the ISC from the singlet exciton reduces the fluorescence quantum efficiency Φ_f and hence the device efficiency, little is known about the ISC in conjugated polymers.[19–24] The ISC efficiency in fluorene–amine copolymers is discussed in terms of the planarity of the chain conformation and energy difference between singlet and triplet excited states. The triplet exciton diffusion dynamics is discussed in terms of triplet state energy of aromatic amines and its incorporation ratio. On the basis of these analyses, the author provides a strategy for further improvement in the efficiency of PLEDs based on fluorene–amine copolymers.

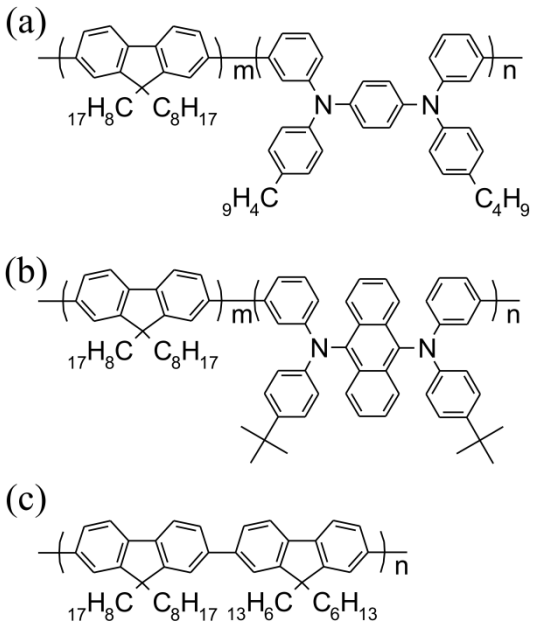

Figure 4-1. Chemical structures of (a) F8-PDA, (b) F8-ADA(-H), and (c) F8-F6. The contents of each unit are as follows: F8-PDA (*m* : *n* = 95 : 5), F8-ADA (*m* : *n* = 97 : 3), and F8-ADA-H (*m* : *n* = 70 : 30).

4.2. Results

4.2.1. Absorption and Photoluminescence Spectra. As shown in Figure 4-2, the absorption spectra of F8-PDA and F8-ADA films resembled that of a fluorene homopolymer, poly(9,9'-di-*n*-octylfluorene-*alt*-9,9'-di-*n*-hexylfluorene) (F8-F6) film, suggesting that the primary photoexcitation in these films is fluorene singlet exciton. This is because the incorporation ratio of aromatic amine units in the polymer chain is as low as ~5 mol% for F8-PDA and ~3 mol% for F8-ADA. In contrast, the fluorescence spectra of F8-PDA and F8-ADA films were red-shifted compared to that of the F8-F6 film, suggesting singlet energy transfer to aromatic amines. The fluorescence band of F8-PDA was also red-shifted compared to that of the corresponding PDA monomer (data is not shown), suggesting that the singlet exciton in F8-PDA is not localized at the PDA unit but delocalized over fluorene and PDA units. On the other hand, the fluorescence band of F8-ADA was almost identical to that of the corresponding ADA monomer (data is not shown), suggesting that the singlet exciton in F8-ADA is localized at the ADA unit. The gray solid lines in Figure 4-2 show the delayed

photoluminescence spectra of these films at 77 K measured by using a mechanical chopper. For all the films, two emission bands were observed: the emission band at a shorter wavelength is the same as the corresponding prompt fluorescence band and hence attributable to the delayed fluorescence probably due to TTA, and the emission band at a longer wavelength is assigned to the phosphorescence band.[25] The phosphorescence spectrum of F8-PDA was the same as that of F8-F6, suggesting that the energetically relaxed triplet exciton in F8-PDA is fluorene triplet excited state as will be discussed later. On the other hand, the phosphorescence spectrum of F8-ADA was red-shifted compared to that of F8-F6, suggesting that the triplet excited state in F8-ADA is ADA triplet excited state. From the peak wavelength of the fluorescence and phosphorescence spectra, the lowest singlet and triplet excited states energy were estimated to be 2.95 and 2.10 eV for F8-F6, 2.76 and 2.10 eV for F8-PDA, and 2.34 and 1.63 eV for F8-ADA.

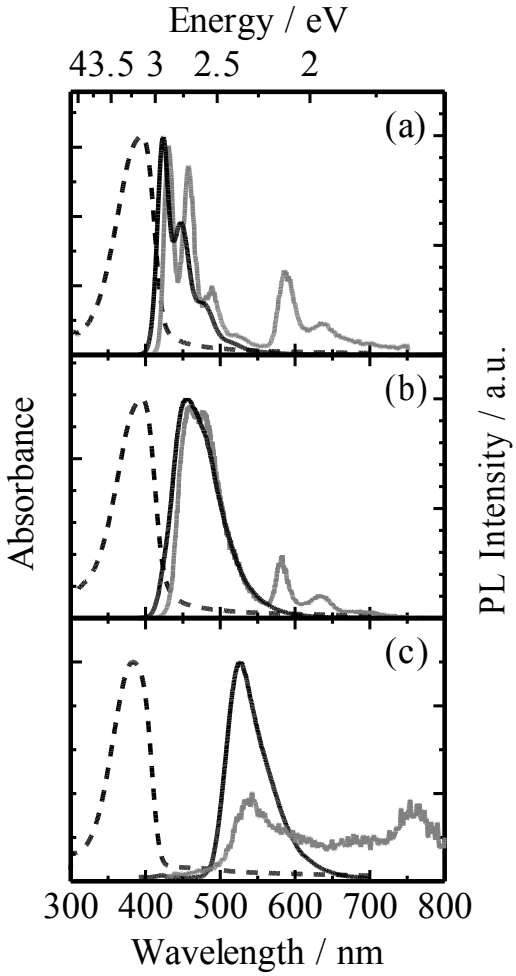

Figure 4-2. Absorption (broken), fluorescence (black), and delayed photoluminescence (gray) spectra of (a) F8-F6, (b) F8-PDA, and (c) F8-ADA films. The delayed photoluminescence spectra were measured at 77 K, which were collected in a time domain longer than 2 ms after the excitation by using a mechanical chopper.

4.2.2. Quantum Chemical Calculations. The molecular structures of the copolymers employed in this study in the ground state were optimized by using the density functional theory (DFT) at the DFT/B3LYP level with the 6-31G(d,p) basis set.[26,27] Here, $F0_n$-PDA-$F0_n$ and $F0_n$-ADA-$F0_n$ oligomers were employed as model compounds for F8-PDA and F8-ADA, respectively, where *n* is the number of fluorene monomer units, and F0 denotes the fluorene monomer unit without alkyl side chains. For $F0_3$-PDA-$F0_3$, as shown in Figure 4-3a, the highest occupied molecular orbital (HOMO) is localized at the PDA unit and the lowest unoccupied molecular orbital (LUMO) is delocalized over several fluorene units. For $F0_3$-ADA-$F0_3$, as shown in Figure 4-3b, HOMO is localized at the ADA unit and the LUMO is localized at the anthracene unit. The lowest singlet excited state of the model oligomers was calculated by the time-dependent DFT (TD-DFT) at the same level. For $F0_n$-PDA-$F0_n$, the vertical transition energy decreases with the increase in the number of fluorene monomer units *n* (see the Appendix), suggesting that the lowest singlet excited state is delocalized over several fluorene units. For $F0_n$-ADA-$F0_n$, on the other hand, the vertical transition energy is independent of *n* and almost identical to that of the ADA monomer (see the Appendix), suggesting that the lowest singlet excited state is localized at the ADA unit. These findings are in good agreement with the photoluminescence spectra, and are qualitatively consistent with the spatial distribution of the HOMO and LUMO in the ground state mentioned above because the main configuration of the lowest singlet excited state is the transition from HOMO to LUMO for both $F0_n$-PDA-$F0_n$ and $F0_n$-ADA-$F0_n$. It is noted that the singlet excited state of F8-PDA has a charge transfer (CT) character between PDA donor and fluorene acceptor and hence is more stable than either fluorene or PDA excited state. Indeed, the fluorescence band of F8-PDA was red-shifted with increasing solvent polarity while that of F8-ADA was less sensitive to the solvent polarity (see the Appendix).[28–31] For the lowest triplet excited states of the oligomers, the optimized geometry and molecular orbital distribution were calculated by using the unrestricted DFT (U-DFT). As shown in Figure 4-3c, the HOMO and LUMO in $F0_3$-PDA-$F0_3$ are located on the fluorene units, which is in good agreement with the fluorene phosphorescence observed for F8-PDA. As shown in Figure 4-3d,

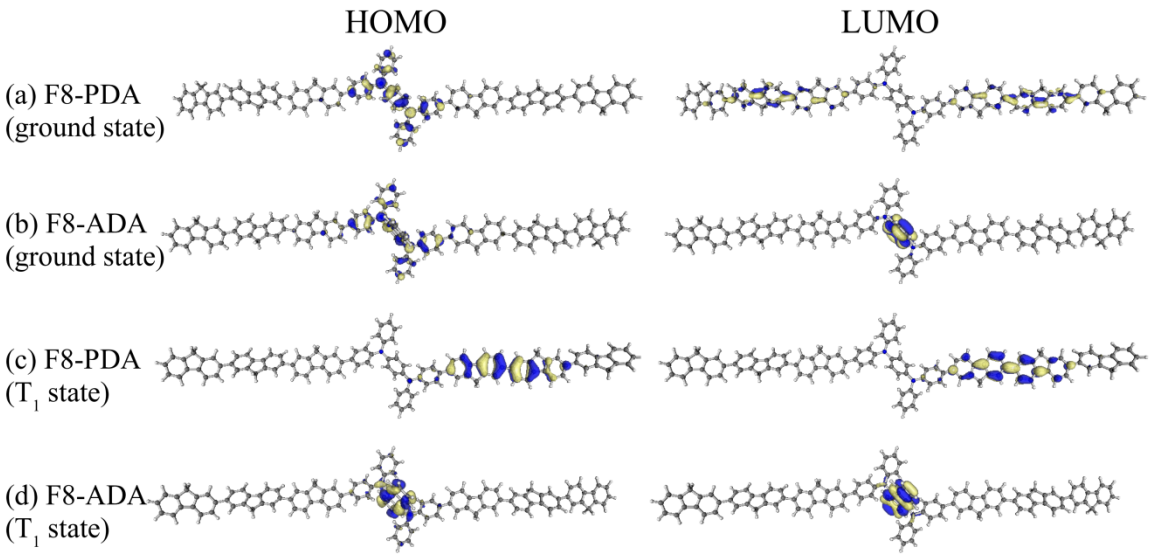

Figure 4- 3. Optimized structures and frontier orbitals of (a,c) $F0_3$-PDA-$F0_3$ and (b,d) $F0_3$-ADA-$F0_3$: (a,b) the ground states, and (c,d) the lowest triplet excited states calculated at the (U-)DFT/B3LYP level with the 6-31G(d,p) basis set.

on the other hand, the HOMO and LUMO in $F0_3$-ADA-$F0_3$ are almost localized at the anthracene unit. In summary, the lowest singlet excited state in F8-PDA is assigned to the CT exciton of $^1(F8^{\delta-}\cdots PDA^{\delta+})$* and that in F8-ADA is assigned to rather neutral local exciton of ^{1}ADA*. The lowest triplet excited state in F8-PDA is assigned to the fluorene triplet excited state ^{3}F8* and that in F8-ADA is assigned to the ADA triplet excited state ^{3}ADA*, the wavefunction of which is almost localized at the central anthracene unit.

4.2.3. Transient Absorption Spectra. *F8-PDA*: Figure 4-4a shows the femtosecond transient absorption spectra of an F8-PDA film measured from 0 ps to 3 ns after the laser excitation at 400 nm. A large absorption band was observed at 800 nm and two small absorption shoulders were observed at 600 and 1000 nm at 0 ps after the laser excitation, and then rapidly decayed in a few picoseconds. These bands are ascribed to the fluorene singlet excitons as reported previously.[25,32] At 100 ps, the fluorene singlet exciton bands disappeared, and instead a large absorption band and broad absorption tail were observed at 600 and 1400 nm, respectively. These bands decayed with a lifetime of τ_S =

620 ps under lower exciton densities, which is the same as the fastest component of the emission lifetime of F8-PDA evaluated by time-correlated single-photon-counting (TCSPC) method (data is shown in the Appendix), and hence are assigned to the CT exciton of $^1(F8^{\delta-}\cdot\cdot PDA^{\delta+})$*. On a time scale of nanoseconds, these CT bands decayed slowly and a new absorption band was observed at around 800 nm. No decay was observed for the new band at around 800 nm in the nanosecond time domain. As shown in Figure 4-5a, the long-lived absorption band at around 800 nm was still observed even in the microsecond time domain but decayed faster under an O_2 atmosphere. The absorption spectrum of the long-lived species was identical to that of triplet excitons in F8-F6. Thus, the long-lived species is ascribed to the fluorene triplet exciton.[25,33,34] No CT triplet exciton $^3(F8^{\delta-}\cdot\cdot PDA^{\delta+})$* was observed over the whole time range measured, suggesting that triplet energy transfer from $^3(F8^{\delta-}\cdot\cdot PDA^{\delta+})$* to ^{3}F8* is much faster than the ISC from $^1(F8^{\delta-}\cdot\cdot PDA^{\delta+})$* to $^3(F8^{\delta-}\cdot\cdot PDA^{\delta+})$*. In other words, the ISC in the CT exciton is the rate-limiting process of the fluorene triplet exciton formation in F8-PDA.

F8-ADA: Figure 4-4b shows the femtosecond transient absorption spectra of an F8-ADA film measured from 0 ps to 3 ns after the laser excitation at 400 nm. The absorption bands observed at 0 ps after the laser excitation are again ascribed to the fluorene singlet exciton, which rapidly decayed in a few picoseconds. At 100 ps, the fluorene singlet exciton bands disappeared, and instead a broad absorption band was observed at 1000 nm. This band decayed slowly with a lifetime of about τ_S = 12 ns under lower exciton densities, which is the same as the emission lifetime of F8-ADA evaluated by the TCSPC method (data is shown in the Appendix), and hence are assigned to the singlet exciton ^{1}ADA*. On a time scale of microseconds, as shown in Figure 4-5b, new absorption bands were observed at around 400 and 1000 nm but decayed faster under O_2 atmosphere. Thus, the new absorption bands are ascribed to the ADA triplet excitons. Note that the negative signal at around 480 nm is attributed to the ground state photobleaching of F8-ADA because the wavelength corresponds to the absorption band of the ADA unit (see the Appendix).

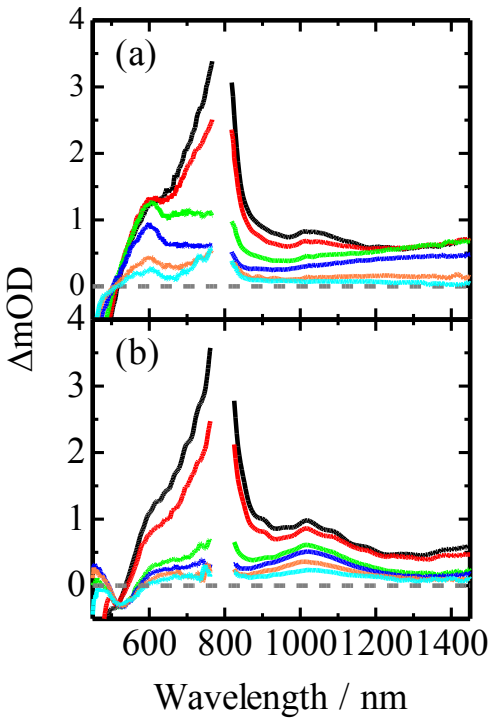

Figure 4-4. Transient absorption spectra of (a) F8-PDA and (b) F8-ADA films excited at 400 nm (7.5 μJ cm^{-2}) measured at 0, 1, 10, 100, 1000, and 3000 ps after the laser excitation from top to bottom in each panel.

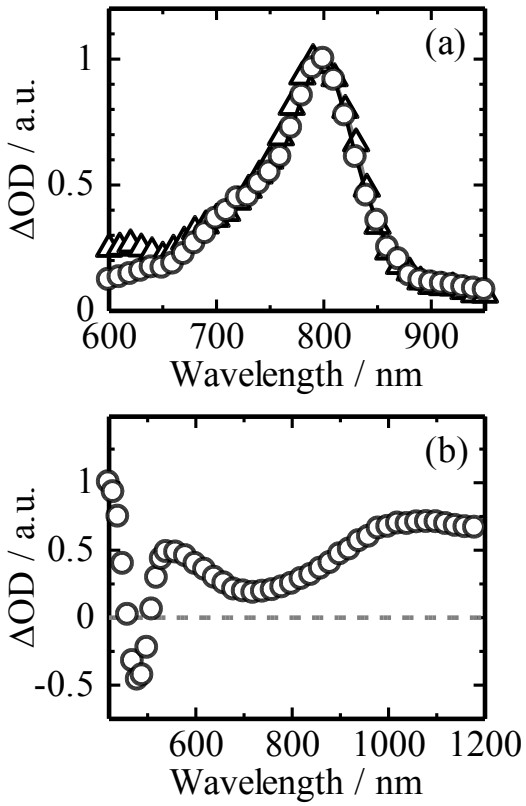

Figure 4-5. Transient absorption spectra of (a) F8-PDA (circles) and (b) F8-ADA films measured at 0.5 and 150 μs after the laser excitation, respectively. The triangles in the panel (a) show the T_1–T_n absorption spectra of the F8-F6 film.

4.2.4. Transient Absorption Decays. In order to focus on the energy transfer from fluorene to amine unit, the transient absorption decays of singlet excitons in the copolymers excited at 400 nm on a time scale of picoseconds was first measured. Figure 4-6 shows the time evolution of transient absorption signals of F8-PDA measured at 1000 and 600 nm. The transient signals at 1000 nm are assigned to the fluorene singlet exciton and well fitted with the sum of an exponential decay (1.6 ps) and a constant fraction. On the other hand, as shown in Figure 4-4a, the transient signals at 600 nm are assigned to a superposition of the fluorene singlet exciton and the CT excitons $^{1}(F8^{\delta-}\cdot\cdot PDA^{\delta+})^{*}$ at an early time stage. The time evolution of the CT exciton band can be extracted by subtracting the transient signals at 1000 nm (open circles) from those at 600 nm (open triangles) after the initial signal at 0 ps is normalized. The time evolution extracted (closed squares) was well fitted with the sum of an exponential rise (1.4 ps) and a constant fraction. This agreement in the rise and decay constants indicates that the CT exciton is generated through rapid energy transfer from the fluorene singlet exciton. The time constant of the energy transfer is as short as ~1.5 ps, which is much shorter than the fluorescence lifetime of an F8-F6 film (420 ps) evaluated by the TCSPC method. Such rapid energy transfer is consistent with the fully quenched fluorene fluorescence as shown in Figure 4-2. A similar energy transfer was observed for F8-ADA (see the Appendix). Note that the fluorene singlet exciton is transferred to the ADA singlet exciton. The time constant of the energy transfer in F8-ADA was estimated to be ~2.9 ps, which is also much faster than the fluorene fluorescence lifetime (420 ps). From these results, it can be safely said that no fluorene singlet exciton at >10 ps because of the rapid energy transfer.

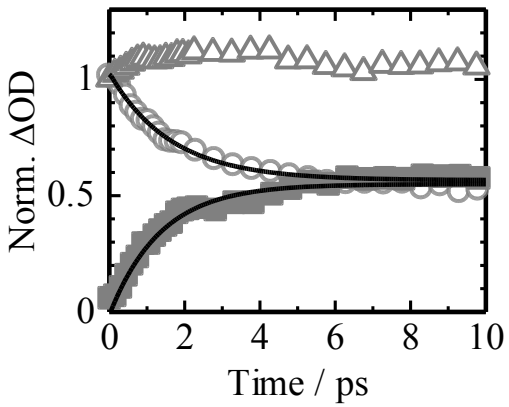

Figure 4-6. Transient absorption signals measured at 1000 nm (open circles), and 600 nm (open triangles) of the F8-PDA film excited at 400 nm (7.5 μJ cm^{-2}). The closed squares show the rise fraction at 600 nm that is evaluated by subtracting the transient signals at 1000 nm (open circles) from those at 600 nm (open triangles) after the initial signal at 0 ps is normalized. The transient signals at 1000 nm were fitted with the sum of an exponential decay and a constant fraction: $\Delta OD(t) = A_d \exp(-t/\tau_d) + B$. The time evolution extracted (closed squares) was fitted with the sum of an exponential rise and a constant fraction: $\Delta OD(t) = A_r \exp(-t/\tau_r) + B$. The solid lines represent the best fitting curves.

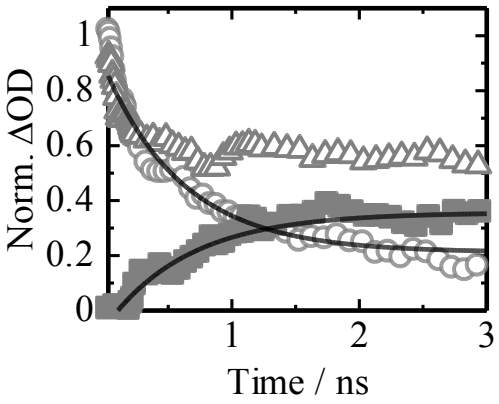

Figure 4-7. Transient absorption signals measured at 600 nm (open circles), and 780 nm (open triangles) of the F8-PDA film excited at 400 nm (7.5 μJ cm^{-2}). The closed squares show the rise fraction at 780 nm that is evaluated by subtracting the transient signals at 600 nm (open circles) from those at 780 nm (open triangles) after the signal at 30 ps is normalized. The transient signals at 600 nm were fitted with the sum of an exponential decay and a constant fraction: $\Delta OD(t) = A_d \exp(-t/\tau_d) + B$. The time evolution extracted (closed squares) was fitted with the sum of an exponential rise and a constant fraction: $\Delta OD(t) = A_r \exp(-t/\tau_r) + B$. The solid lines represent the best fitting curves.

Next the time evolution of triplet exciton in the copolymers was measured to study the formation dynamics of triplet excitons on a time scale of nanoseconds. Figure 4-7 shows the time evolution of transient absorption signals of F8-PDA measured at 600 and 780 nm. The absorption band at 600 nm is safely ascribed to the CT exciton alone because the fluorene singlet exciton is already deactivated in this time domain. This band was well fitted with the sum of an exponential decay (620 ps) and a constant fraction. The decay constant was independent of the excitation intensity up to 20 μJ cm^{-2}, indicating that monomolecular deactivation pathways such as radiative decay and ISC are dominant but bimolecular reactions such as singlet–singlet annihilation (SSA) are negligible. The lifetime of 620 ps is in good agreement with the fastest component of the fluorescence lifetime of F8-PDA evaluated by the TCSPC method. As shown in Figure 4-4a, the transient signals at 780 nm are assigned to a superposition of the CT exciton and the fluorene triplet exciton at a later time stage. It can be safely assumed that no triplet exciton is generated up to 30 ps after the laser excitation because spin flip in organic materials is generally negligible in such a short time domain.

Thus, the time evolution of the fluorene triplet exciton can be extracted by subtracting the transient signals at 600 nm (open circles) from those at 780 nm (open triangles) after both signals are normalized at 30 ps. The time evolution extracted (closed squares) was well fitted with the sum of an exponential rise (650 ps) and a constant fraction, which is in good agreement with the decay constant of the CT exciton. This agreement indicates that triplet exciton is generated through the ISC as will be discussed later. For F8-ADA, triplet exciton was observed as shown in Figure 4-5b. However, the triplet exciton formation in F8-ADA was not observed directly because of the small molar absorption coefficient of F8-ADA triplet excitons (6.5×10^3 M^{-1} cm^{-1}, see the Appendix) and the long lifetime of ADA singlet exciton (11.2 ns) as will be discussed later.

Finally, the decay dynamics of triplet excitons in the copolymers on a time scale of microseconds was measured. Here, transient signals $\Delta OD(t)$ were converted into the number density of triplet excitons $N(t)$ according to the Beer–Lambert law: $N(t) = \Delta OD(t)\ N_A\ (1000\varepsilon l)^{-1}$ where N_A is the Avogadro's constant, ε is the molar absorption coefficient (5×10^4 M^{-1} cm^{-1} for the fluorene triplet exciton[33] and 6.5×10^3 M^{-1} cm^{-1} for the ADA triplet exciton), and l is the film thickness. Figure 4-8a shows the time evolution of the fluorene triplet exciton in F8-PDA measured at 800 nm under various excitation intensities. Under the lowest excitation intensity, the transient decay was fitted with an exponential function $N(t) = A \exp(-t/\tau_T)$ with a lifetime of $\tau_T = 3.6$ μs, which is due to radiative and non-radiative decay pathways without bimolecular reactions. Under higher excitation intensities, as shown in Figure 4-8a, the transient absorption decayed faster, suggesting that the TTA becomes more dominant under higher excitation intensity as will be discussed later. On the other hand, as shown in Figure 4-8b, the time evolution of the ADA triplet exciton measured at 1000 nm was fitted with an exponential function $N(t) = A \exp(-t/\tau_T)$ with a lifetime of $\tau_T = 8.1$ ms and independent of the excitation intensity, indicating that monomolecular deactivation is dominant rather than TTA. This is probably due to the low concentration of ADA units. Indeed, as shown in Figure 4-8c, the ADA triplet exciton decayed faster in F8-ADA with ~30 mol% ADA incorporation

ratio (hereafter abbreviated as F8-ADA-H) under higher excitation intensities, suggesting that the TTA is dominant in F8-ADA-H as will be discussed later.

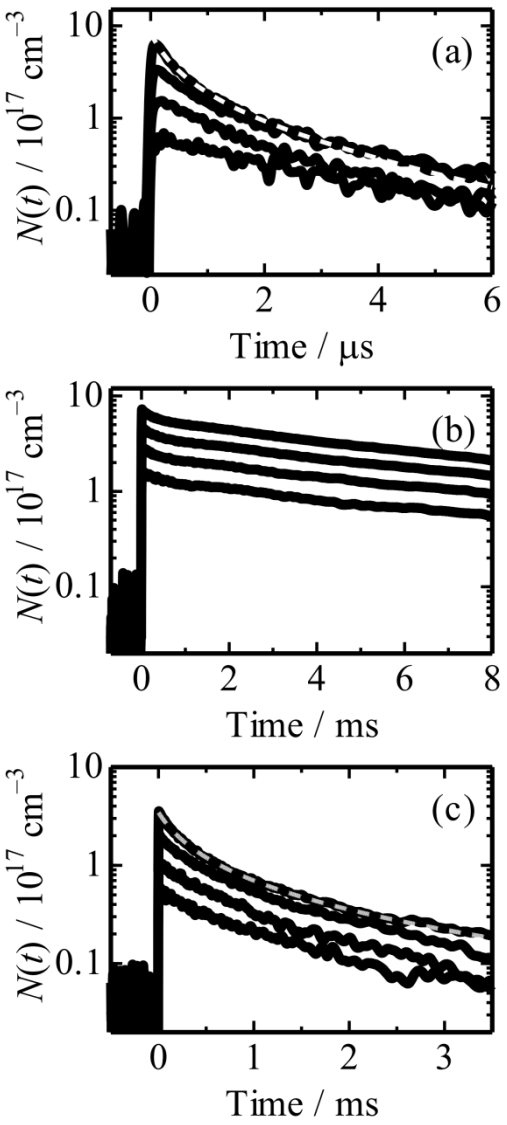

Figure 4-8. Transient absorption decays of (a) F8-PDA at 800 nm, (b) F8-ADA at 1000 nm, and (c) F8-ADA-H at 1000 nm. The excitation intensity was varied over (a) 1.3, 5, 10, and 20 μJ cm^{-2}, and (b), (c) 10, 18, 30, and 45 μJ cm^{-2} from bottom to top. Transient signals ΔOD(t) were converted into the number density of triplet excitons $N(t)$ according to the Beer–Lambert law: $N(t) = \Delta OD(t)\ N_A\ (1000\varepsilon l)^{-1}$. The broken lines in panels (a) and (c) represent the best fitting curves with Eq. 4-6.

Scheme 4-1. Energy Diagrams in F8-PDA and F8-ADA Films

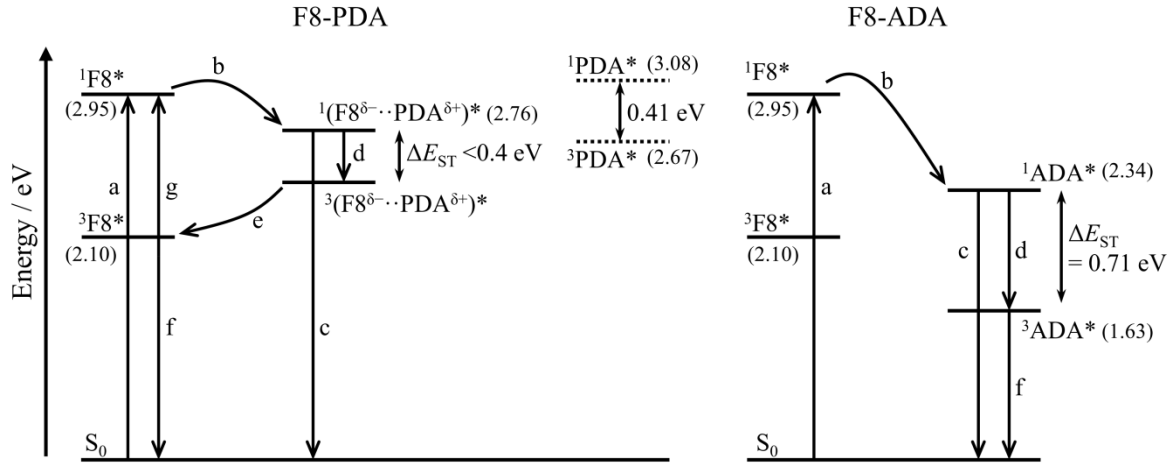

[a] Key: (a) photon absorption, (b) singlet energy transfer, (c) radiative and non-radiative deactivations (k_r, k_{nr}), (d) intersystem crossing (k_{ISC}), (e) triplet energy transfer, (f) monomolecular triplet deactivation, and (g) triplet–triplet annihilation (TTA). The values in parentheses are energy levels of the states evaluated from photoluminescence measurements.

4.3. Discussion

Transient species in the fluorene–amine copolymers is first summarized before moving onto the detailed discussion. As shown in Scheme 4-1, the primary photoexcitation formed after the 400-nm excitation is the fluorene singlet excitons ^{1}F8* either for F8-PDA or F8-ADA (arrows a). On a time scale of picoseconds, the fluorene singlet exciton is completely quenched because of rapid energy transfer to the aromatic amine unit with a time constant of 1.5 ps for F8-PDA and 2.9 ps for F8-ADA (arrows b). As a result of the energy transfer, the ^{1}F8* in F8-PDA is relaxed to a CT exciton formed between PDA donor and fluorene acceptor ^{1}(F8$^{\delta-}$··PDA$^{\delta+}$)* and that of F8-ADA is relaxed to a neutral localized exciton ^{1}ADA*. On a time scale of nanoseconds, these singlet excitons deactivate to the ground state (arrows c) or triplet excited state through the ISC (arrows d). In F8-PDA, ^{3}F8* is generated probably because of rapid triplet energy transfer from ^{3}(F8$^{\delta-}$··PDA$^{\delta+}$)* much faster than the ISC (arrow e). In other words, the rate-limiting process of ^{3}F8* formation is the ISC from ^{1}(F8$^{\delta-}$··PDA$^{\delta+}$)* to ^{3}(F8$^{\delta-}$··PDA$^{\delta+}$)*. In F8-ADA, triplet exciton is localized at the ADA unit ^{3}ADA*. Note that the wavefunction of ^{3}ADA* is almost localized at the central anthracene unit. On a time scale of micro- to milliseconds, these triplet excitons monomolecularly deactivate to the

ground state (arrows f). Before the monomolecular deactivation to the ground state, some triplet excitons collide with another triplet exciton and consequently singlet excitons are regenerated by the TTA (arrow g).

4.3.1. Enhancement of Intersystem Crossing. First the efficient triplet exciton formation in the fluorene–amine copolymer films is discussed. In the absence of SSA or TTA, the rate equations for the singlet and triplet exciton dynamics can be described by Eq. 4-1

$$\begin{aligned} \frac{\mathrm{d}N_{\mathrm{S}}(t)}{\mathrm{d}t} &= -kN_{\mathrm{S}}(t) \\ \frac{\mathrm{d}N_{\mathrm{T}}(t)}{\mathrm{d}t} &= k_{\mathrm{ISC}}N_{\mathrm{S}}(t) - \frac{N_{\mathrm{T}}(t)}{\tau_{\mathrm{T}}} \end{aligned} \tag{4-1}$$

where N_S and N_T are the singlet and triplet exciton density, respectively, k_{ISC} is the ISC rate, and k is the sum of the radiative decay rate (k_r), the ISC rate, and all the other non-radiative decay rate (k_{nr}). The second term in the rate equation of triplet excitons dynamics is negligible on a time scale of nanoseconds if the triplet exciton lifetime is long enough. Thus, the solution of Eq. 4-1 is given by Eq. 4-2

$$\begin{aligned} N_{\mathrm{S}} &= N_{\mathrm{S0}}\exp(-kt) \\ N_{\mathrm{T}} &= \frac{k_{\mathrm{ISC}}}{k}N_{\mathrm{S0}}[1-\exp(-kt)] \end{aligned} \tag{4-2}$$

where N_{S0} is the initial singlet exciton density. For F8-PDA, the ISC quantum efficiency was estimated to be $\Phi_{ISC} = 0.34$ from the time evolution of triplet exciton as shown in Figure 4-7 (details are described in the Appendix). As summarized in Table 4-1, the ISC, radiative, and non-radiative decay rates were estimated to be $k_{ISC} = 2.0 \times 10^8$ s^{-1}, $k_r = 3.5 \times 10^8$ s^{-1}, and $k_{nr} = 0.4 \times 10^8$ s^{-1}, respectively, from an averaged fluorescence lifetime of 1.7 ns and a fluorescence quantum efficiency of $\Phi_f = 0.60$. For F8-ADA, as will be discussed later, the upper limits of the ISC quantum efficiency and the ISC rate were estimated to be $\Phi_{ISC} < 0.25$ and $k_{ISC} < 2.2 \times 10^7$ s^{-1}, respectively. Note that these values are expected to be close to the true values because the fluorescence lifetime of F8-ADA

depended only slightly on temperature, suggesting that k_{nr} is expected to be small compared to other decay channels.

The ISC rate in F8-PDA is as high as $k_{ISC} = 2.0 \times 10^8$ s^{-1}, which is one order of magnitude larger than that of polyfluorenes (10^6 – 10^7 s^{-1})[2,22] and that of typical hydrocarbons (~10^7 s^{-1}).[2,35–37] In general, the small ISC rate in polyfluorenes is ascribed to the small spin–orbit coupling and the absence of heavy atoms.[2,35] As a result, the ISC quantum efficiency in polyfluorenes is typically as low as $\Phi_{ISC} \approx 0.01 – 0.02$. In contrast, aromatic amines exhibit relatively large ISC rate depending on the molecular structure.[38–40] For example, the ISC rate increases dramatically in going from planar carbazole (3.7×10^7 s^{-1}) to non-planar diphenylamine (3.6×10^8 s^{-1}) while the radiative decay rates remain almost the same ($3.0 – 4.4 \times 10^7$ s^{-1}). As a result, the ISC quantum efficiency increases from ~0.4 for carbazole to ~0.9 for diphenylamine.[38] This is probably because the spin–orbit coupling is enhanced by non-planar geometry of diphenylamine where a spin momentum change due to spin flip is likely to be compensated by an orbital momentum change.[2,35] The ISC rate in F8-PDA is of the same order of that in diphenylamine. Therefore it is concluded that the spin–orbit coupling in F8-PDA is enhanced by non-planar geometry of the PDA unit.[23,24,41,42]

The fluorescence quantum efficiency of F8-PDA is still as high as $\Phi_f = 0.60$ even though aromatic amine units are incorporated, and hence is useful as a light-emitting polymer material for PLEDs. This is in sharp contrast to the low fluorescence quantum efficiency of aromatic amine derivatives due to the efficient ISC.[38–40,43] For example, the fluorescence quantum efficiency of the PDA monomer has been reported to be only $\Phi_f \approx 0.05$.[43] The large Φ_f in F8-PDA is attributed to the large radiative decay rate $k_r = 3.5 \times 10^8$ s^{-1}, which is one order of magnitude higher than that of aromatic amine monomers. This is probably because the wavefunction of the singlet excited state is delocalized over several fluorene units in F8-PDA, as shown in Figure 4-3, to increase the oscillator strength though the spatial overlap between the HOMO and LUMO is small because of the CT character. Thus it is concluded that the CT exciton in F8-PDA has both properties of the fluorene unit with high Φ_f and the aromatic amine unit with high Φ_{ISC}.

In comparison with F8-PDA, F8-ADA exhibits the small ISC rate (<2.2 × 10^7 s^{-1}), which is at least one order of magnitude smaller than that of F8-PDA. The small ISC rate in F8-ADA is

Table 4-1. Kinetic Parameters of F8-PDA and F8-ADA

	τ^a / ns	Φ_f	$\Phi_{ISC}{}^c$	$k_r{}^d$ / s^{-1}	$k_{ISC}{}^e$ / s^{-1}	$k_{nr}{}^f$ / s^{-1}
F8-PDA	1.7[b]	0.6	0.34	3.5 × 10^8	2.0 × 10^8	0.4 × 10^8
F8-ADA	11.2	0.75	<0.25	6.6 × 10^7	<2.2 × 10^7	N.A.

[a] The fluorescence lifetimes were evaluated by the TCSPC method as shown in the Appendix. [b] Averaged fluorescence lifetime. [c] F8-PDA: determined from Figure 7. F8-ADA: the upper limit of Φ_{ISC} was estimated as $1 - \Phi_f$. [d] $k_r = \Phi_f/\tau$. [e] F8-PDA: $k_{ISC} = \Phi_{ISC}/\tau$. F8-ADA: the upper limit of k_{ISC} was estimated as $k_{ISC} = 1/\tau - k_r$. [f] F8-PDA: $k_{nr} = 1/\tau - (k_r + k_{ISC})$. F8-ADA: not available.

attributed to the large energy difference between the singlet and triplet excited states ΔE_{ST}. According to the energy gap law, the ISC rate is predicted to increase with decreasing difference in the ΔE_{ST}, which is proportional to twice the exchange integral K.[2,35] Thus, the ISC rate would be larger with the smaller K, which roughly corresponds to the smaller overlap between the HOMO and LUMO. Although the ΔE_{ST} in F8-PDA was not estimated, it can be assumed to be lower than that of PDA monomer (0.41 eV) because of the small overlap of the HOMO and LUMO in F8-PDA due to the CT character of the F8-PDA singlet exciton. On the other hand, as mentioned above, the ΔE_{ST} in F8-ADA is 0.71 eV, which is probably larger than that of F8-PDA. Thus, the small ISC rate in F8-ADA can be rationalized by the large ΔE_{ST} in terms of the energy gap law.[43] As a conclusion in this section, it is noted that an incorporation of aromatic amine units enhances the ISC rate depending on the planarity of chain conformation and the ΔE_{ST}: a non-planar conformation and a small ΔE_{ST} would enhance the ISC rate.

4.3.2. Triplet Exciton Diffusion. Next, the diffusion dynamics of triplet excitons in the fluorene–amine copolymer films is discussed from the view point of energy level alignments of fluorene and aromatic amine triplet excited states. As shown in Figure 4-8a, the efficient TTA is observed for F8-PDA. The rate equation for triplet exciton decay including TTA is given by Eq. 4-3

$$\frac{\mathrm{d}N(t)}{\mathrm{d}t} = -\frac{N(t)}{\tau_{\mathrm{T}}} - f\gamma_{\mathrm{TTC}}(t)N(t)^2 \tag{4-3}$$

where $N(t)$ is the triplet exciton density at a delay time t, τ_{T} is a triplet exciton lifetime of 3.6 μs, and $\gamma_{\mathrm{TTC}}(t)$ is the triplet exciton collision rate, which is distinguished from the bimolecular annihilation rate. Here three-dimensionally isotropic exciton diffusion is assumed because all the films employed are amorphous. In this case, $\gamma_{\mathrm{TTC}}(t)$ is simplified as Eq. 4-4 at a longer time stage

$$\gamma_{\mathrm{TTC}} = 8\pi DR \tag{4-4}$$

where D is the isotropic diffusion coefficient, and R is the effective reaction radius (here R is assumed to be 1 nm).[44] The factor f is the removing probability of triplet excitons after one triplet encounters another one, which depends on the dynamics after the encounter. Upon the encounter of two triplet excitons, nine possible intermediate pair states are formed statistically: one singlet pair state ^{1}(TT), three triplet pair states ^{3}(TT), and five quintet pair states ^{5}(TT).[1,2] As summarized in Eq. 4-5, a singlet pair state removes two triplet excitons, a triplet pair state removes one triplet exciton, and a quintet pair state removes no triplet excitons because the quintet states are typically energetically inaccessible. Therefore, the total removing probability f is roughly estimated to be 5/18.[45]

$$\mathrm{T_1} + \mathrm{T_1} \xrightarrow{\gamma_{\mathrm{TTC}}} \begin{cases} \xrightarrow{1/9} & {}^1(\mathrm{TT}) \rightarrow \mathrm{S}_n + \mathrm{S}_0 \rightarrow \mathrm{S_1} + \mathrm{S_0} + \mathrm{phonon} \\ \xrightarrow{3/9} & {}^3(\mathrm{TT}) \rightarrow \mathrm{T_n} + \mathrm{S_0} \rightarrow \mathrm{T_1} + \mathrm{S_0} + \mathrm{phonon} \\ \xrightarrow{5/9} & {}^5(\mathrm{TT}) \rightarrow \mathrm{T_1} + \mathrm{T_1} \end{cases} \tag{4-5}$$

More sophisticated treatments of the TTA have been reported elsewhere,[1,46,47] but this simple assumption is enough for rough estimation of triplet exciton diffusion coefficients. Thus, Eq. 4-5 can be solved as Eq. 4-6

$$N(t) = \frac{N_0 \exp(-t/\tau_T)}{1 + f\gamma_{TTC}\tau_T N_0[1 - \exp(-t/\tau_T)]} \quad (4\text{-}6)$$

From the best fitting result as shown in Figure 4-8a, the collision rate γ_{TTC} and diffusion coefficient D were estimated to be 1.2×10^{-11} cm^3 s^{-1} and 4.7×10^{-6} cm^2 s^{-1}, respectively, for F8-PDA. From the diffusion coefficient and the triplet excitons lifetime, triplet exciton diffusion length $L_D = (D\tau)^{1/2}$ was estimated to be 41 nm. As summarized in Table 4-2, these values are in the same order as those of F8-F6 (D = 7.9×10^{-6} cm^2 s^{-1}, L_D = 50 nm, the kinetic data are shown in the Appendix), indicating that triplet excitons generated in F8-PDA can freely mobile in the film.

On the other hand, as shown in Figure 4-8b, the triplet exciton decay in F8-ADA hardly depends on the exciton density, suggesting that the diffusion of triplet excitons is inefficient in the F8-ADA film. In the triplet exciton diffusion, the Dexter energy transfer plays the primary role.[1,2,35,48] Thus, the separation distance between neighboring chromophores has critical impact on the diffusion coefficient. The average distance between neighboring ADA units is estimated to be as long as 3.6 nm, assuming that a density of the F8-ADA film is 1 g cm^{-3}. Such a long separation distance causes poor triplet exciton diffusion, but rather triplet exciton trapping at ADA units. As shown in Figure 4-8c, triplet exciton became mobile by increasing ADA incorporating ratio. The collision rate γ_{TTC} and diffusion coefficient D of F8-ADA-H were estimated to be 3.0×10^{-14} cm^3 s^{-1} and 1.2×10^{-8} cm^2 s^{-1}, respectively, which are still about 400 times smaller than those of F8-PDA. The average distance is estimated to be 1.6 nm, which is still much longer than that of fluorene chromophores. Therefore it isconcluded that triplet excited state energy of aromatic amines incorporated should be higher than that of fluorenes in order to achieve a large diffusion coefficient. Interestingly, on the other hand, the diffusion length is estimated to be 48 nm, which is in the same order as that of F8-PDA. This is because the small diffusion coefficient is compensated by significantly longer triplet exciton lifetime of 1.9 ms, which is about 500 times longer than that of F8-PDA. As mentioned above, the triplet exciton lifetime in F8-ADA is as long as 1.9 – 8.1 ms depending on the ADA incorporation ratio, which are on the same order as that of the anthracene monomer (~ms) reported

Table 4-2. Fitting Parameters for Triplet Exciton Diffusion

	γ_{TTC} / cm^3 s^{-1}	D / cm^2 s^{-1}	τ_T / s	L_D / nm
F8-PDA	1.2×10^{-11}	4.7×10^{-6}	3.6×10^{-6}	41
F8-ADA[a]	N.A.	N.A.	8.1×10^{-3}	N.A.
F8-ADA-H	3.0×10^{-14}	1.2×10^{-8}	1.9×10^{-3}	48
F8-F6	2.0×10^{-11}	7.9×10^{-6}	3.2×10^{-6}	50

[a] The triplet collision rate γ_{TTC}, the diffusion coefficient D, and the diffusion length L_D of F8-ADA were not available.

previously.[49,50] On the other hand, the triplet exciton lifetime in F8-PDA is as short as 3.6 μs, which is much shorter than that of the fluorene monomer (150 μs).[51] Thus, the longer lifetime in F8-ADA is probably because triplet excitons in F8-ADA are almost localized at a rigid anthracene unit while triplet excitons in F8-PDA are delocalized over several fluorene units where C–C bonds linking between neighboring fluorene units freely rotate. As a conclusion of this section, it is noted that triplet excited state energy of aromatic amines incorporated should be higher than that of fluorenes in order to achieve a large diffusion coefficient and hence a long diffusion length. It is also noted that long diffusion length of triplet excitons can be achieved by long triplet exciton lifetime due to a rigid structure even though the diffusion coefficient is not so large.

4.3.3. Relevance to Polymer Light-Emitting Diodes. Finally, the author describes the relevance of the photophysics discussed above to PLED efficiency. The classical estimate of external quantum efficiency (EQE) of fluorescent PLEDs is given by Eq. 4-7

$$\mathrm{EQE} = \eta_c \times \eta_s \times \Phi_f \times \eta_{out} = \mathrm{IQE} \times \eta_{out} \quad (4\text{-}7)$$

where η_c is the charge balance ratio, η_s is the singlet exciton generation yield, and η_{out} is the emission out-coupling efficiency. For the device based on F8-PDA, the maximum EQE is 4.5%, which corresponds to the IQE of 23% if η_{out} is assumed to be 20% for the device geometry in this study. Using a value of 60% for Φ_f of F8-PDA, assuming perfect charge balance η_c = 100%, η_s is estimated

to be 38%, which is close to the theoretical upper limit of η_s = 40% under the efficient TTA as mentioned above. This simple estimation indicates that TTA in F8-PDA is efficient enough to reproduce singlet excitons.[8] However, the EQE is limited to only 4.5% because of relatively low fluorescence quantum efficiency of F8-PDA (60%). For the device based on F8-ADA, on the other hand, the EQE is 4.1%. Although the fluorescence quantum efficiency of F8-ADA is high (75%), η_r is estimated to be only 28% because of the less efficient TTA. Thus, the EQE of the device based on F8-ADA is limited by the low singlet generation yield. For further improvement in the device efficiency, both high singlet generation yield and high fluorescence quantum efficiency should be satisfied simultaneously. To improve the singlet generation yield, the author therefore emphasizes again that triplet energy level of aromatic amines incorporated should be higher than that of fluorenes as is the case of F8-PDA. To increase the fluorescence quantum efficiency, it would be important to decrease the ISC rate. In other words, a small spin–orbit coupling and a large singlet–triplet energy difference ΔE_{ST} would be desired. More specifically, increasing planarity of the chain conformation and decreasing CT character of the singlet excited state would be important.

4.4. Conclusions

In this chapter the triplet exciton formation and decay dynamics in fluorene–amine copolymer films with different amine derivatives, F8-PDA and F8-ADA, was studied by transient absorption spectroscopy. The ISC quantum efficiency and ISC rate of F8-PDA are estimated to be 0.34 and 2.0 $\times 10^8$ s^{-1}, respectively, which is one order of magnitude larger than that of polyfluorenes because the spin–orbit coupling is enhanced by non-planar geometry of PDA unit. The fluorescence quantum efficiency of F8-PDA is still as high as Φ_f = 0.60 even though aromatic amine units are incorporated, and hence is useful as a light-emitting polymer material for PLEDs. The larger Φ_f in F8-PDA compared to that in PDA monomer is attributed to the larger radiative decay rate $k_r = 3.5 \times 10^8$ s^{-1}, which is one order of magnitude higher than that of aromatic amine monomers. This is probably because the wavefunction of the singlet excited state is delocalized over several fluorene units in F8-

PDA to increase the oscillator strength though the spatial overlap between the HOMO and LUMO is small because of the CT character. Thus it is concluded that the CT exciton in F8-PDA has both properties of the fluorene unit with high Φ_f and the amine unit with high Φ_{ISC}. In comparison with F8-PDA, F8-ADA exhibits the small ISC rate ($<2.2 \times 10^7$ s^{-1}). The small ISC rate in F8-ADA can be rationalized by the large ΔE_{ST} (<0.4 eV for F8-PDA, and 0.71 eV for F8-ADA) in terms of the energy gap law. Therefore, an incorporation of aromatic amine units enhances the ISC rate depending on the planarity of chain conformation and the ΔE_{ST}: a non-planar conformation and a small ΔE_{ST} would enhance the ISC rate.

The diffusion coefficient D and diffusion length L_D of the triplet excitons generated in F8-PDA are estimated to be 4.7×10^{-6} cm^2 s^{-1} and 41 nm, respectively. These values are on the same order as those in F8-F6, indicating that the triplet excitons generated in F8-PDA can freely mobile in the film. On the other hand, the diffusion of triplet excitons is inefficient in the F8-ADA film because long separation distance of ADA units causes triplet exciton trapping at ADA units. Although triplet exciton became mobile by increasing ADA incorporating ratio (F8-ADA-H), the diffusion coefficient in F8-ADA-H is estimated to be 1.2×10^{-8} cm^2 s^{-1}, which is still about 400 times smaller than that in F8-PDA. Interestingly, on the other hand, the diffusion length is estimated to be 48 nm, which is on the same order as that in F8-PDA. This is because the small diffusion coefficient is compensated by significantly longer triplet exciton lifetime of 1.9 ms, which is about 500 times longer than that in F8-PDA. Therefore, the triplet state energy of aromatic amines incorporated should be higher than that of fluorenes in order to achieve a large diffusion coefficient and hence a long diffusion length. In other words, even though the diffusion coefficient is not so large, the diffusion length of triplet excitons can be long with a long triplet exciton lifetime due to a rigid structure.

From the maximum EQE of the device based on F8-PDA, η_s is estimated to be 38%, indicating that TTA in F8-PDA is efficient enough to reproduce singlet excitons. However, the EQE is limited to only 4.5% because of the relatively low fluorescence quantum efficiency in F8-PDA (60%). For

the device based on F8-ADA, on the other hand, although the fluorescence quantum efficiency in F8-ADA is high (75%), η_s is estimated to be only 28% because of the less efficient TTA. Thus, the EQE of the device based on F8-ADA is limited by the low singlet generation yield. For further improvement in the device efficiency, both high singlet generation yield and high fluorescence quantum efficiency should be satisfied simultaneously. To improve the singlet generation yield, The author therefore emphasizes again that triplet energy level of aromatic amines incorporated should be higher than that of fluorenes as is the case of F8-PDA. To increase the fluorescence quantum efficiency, it would be important to decrease the ISC rate. In other words, a small spin–orbit coupling and a large singlet–triplet energy difference ΔE_{ST} would be desired. More specifically, increasing the planarity of the chain conformation and decreasing CT character in the singlet excited state would be important.

4.5. Experimental Section

Sample Preparation. Polymers employed in this study were synthesized at Sumitomo Chemical Co., Ltd. Thin films were prepared by spincoating from a toluene solution. For transient absorption measurements, a sapphire substrate was employed to prevent waveguiding and amplified spontaneous emission[52,53] while the other experiments have done with a quartz substrate. The film thickness was about 100 – 150 nm.

Measurements. UV–visible absorption and photoluminescence spectra were measured with a UV−visible spectrophotometer (Hitachi, U-3500) and a fluorescence spectrophotometer (Hitachi, F-4500) equipped with a red-sensitive photomultiplier (Hamamatsu, R928F), respectively. Phosphorescence spectra were collected in a time domain longer than 2 ms after the excitation by using a mechanical chopper incorporated in the fluorescence spectrophotometer (Hitachi, F-4500). Photoluminescence decay was measured by the time-correlated single-photon-counting (TCSPC) method (Horiba Jobin Yvon, FluoroCube). The excitation wavelength was 375 nm. The detection wavelength was 460 nm for F8-PDA and 530 nm for F8-ADA, respectively. The total instrument response function is an FWHM of ca. 280 ps. A weak excitation power (~nJ cm^{-2}) was used in the measurement to prevent singlet–singlet annihilation.

Femtosecond transient absorption data were collected with a pump and probe femtosecond transient spectroscopy system. This system consists of a transient absorption spectrometer (Ultrafast Systems, Helios) and a regenerative amplified Ti:sapphire laser (Spectra-Physics, Hurricane). The amplified Ti:sapphire laser provided 800 nm fundamental pulses at a repetition rate of 1 kHz with an energy of 0.9 mJ and a pulse width of 100 fs (FWHM), which were split into two optical beams with a beam splitter to generate pump and probe pulses. One fundamental beam was converted into pump pulses at 400 nm with a second harmonic generator (Spectra-Physics, TP-F). The other fundamental beam was converted into white light pulses employed as probe pulses in the wavelength region from 400 to 1700 nm. The pump pulses were modulated mechanically with a repetition rate of 500 Hz. The temporal evolution of the probe intensity was recorded with a CMOS linear sensor (Ultrafast

Systems, SPEC-VIS) for the visible measurement and with an InGaAs linear diode array sensor (Ultrafast Systems, SPEC-NIR) for the near-IR measurement. Transient absorption spectra and decays were collected over the time range from −5 ps to 3 ns. Typically, 2500 laser shots were averaged at each delay time to obtain a detectable absorbance change as small as ~10^{-4}. In order to cancel out orientation effects on the dynamics, the polarization direction of the linearly polarized probe pulse was set at a magic angle of 54.7 ° with respect to that of the pump pulse.

Microsecond transient absorption data were collected with a highly sensitive microsecond transient absorption system. A dye laser (Photon Technology International Inc., GL-301) pumped by a nitrogen laser (Photon Technology International Inc., GL-3300) was used as an excitation source, which provides sub-ns pulses with various fluences from ~μJ to 0.1 mJ cm^{-2} at a repetition rate of 4 Hz. The excitation wavelength was 400 nm for F8-PDA and 337 nm for F8-ADA. A tungsten lamp (Thermo-Oriel, Model 66997) with an intensity controller (Thermo-Oriel, Model 66950) was used as a probe light source. The probe wavelength was selected by two monochromators (Ritsu, MC-10C) and appropriate optical cut-off filters equipped before and after the sample to reduce scattered light and emission. The temporal evolution of ΔOD was reduced using a high-gain Si photodiode (Hamamatsu Photonics, S1722-01). The signal from the photodiode was pre-amplified and sent to a main amplifier (Costronics Electronics) with an electronic band-pass filter to improve the signal-to-noise ratio. Finally, the amplified signal was collected using a digital oscilloscope (Tektronix, TDS2022), which was synchronized with a trigger signal of the laser pulse from Si photodiode (Thorlabs Inc., DET10A). The instrument response was in the order of 60 ns. Transient absorption decays were collected over the time range from sub-μs to ms, averaging 4000 laser shots on each decay time scale, yielding a sensitivity of 10^{-6} to 10^{-4} depending on the measuring time domain. The sample films were sealed in a quartz cuvette purged with N_2. Note that the transient absorption spectra and dynamics were highly reproducible even after the several times measurements. In other words, the laser irradiation had negligible effects on the sample degradation at least under this experimental condition.

Calculations. All calculations were carried out using the Firefly QC package,[26] which is partially based on the GAMESS (US)[27] source code. The structures of model oligomers in the ground state were optimized by using density functional theory (DFT) with a hybrid exchange-correlation functional (B3LYP) with the 6-31G(d,p) basis set. The vertical transition energies of the model oligomers were calculated by time-dependent DFT (TD-DFT) with optimized geometries in the ground state. The calculation was performed with the same level of the ground state. The structures of model oligomers in the lowest triplet excited state were optimized by using unrestricted DFT (U-DFT) with the same level. Molecular orbitals were visualized by using Molekel 5.4.[54]

4.6. Experimental Section

4.6.1. Vertical Transition Energy. Molecular structures of $F0_n$-PDA-$F0_n$ and $F0_n$-ADA-$F0_n$ in the ground states were optimized with DFT/B3LYP level at the 6-31G(d,p) basis set. On the basis of the optimized structure, the vertical transition energy of the lowest singlet excited state was calculated with TD-DFT/B3LYP level at the 6-31G(d,p) basis set.[26,27] Figure 4-A1 shows the vertical transition energies of $F0_{2n}$ (open circles, as a reference), $F0_n$-PDA-$F0_n$ (open triangles), and $F0_n$-ADA-$F0_n$ (open squares) as a function of the number of fluorene units n. The vertical transition energy of $F0_3$-PDA-$F0_3$ was lower than that of the PDA monomer, while that of $F0_n$-ADA-$F0_n$ was almost identical to that of ADA monomer, suggesting that the wavefunction of F8-PDA in the excited state is delocalized over the fluorene and PDA units, whereas that of F8-ADA is localized at the ADA unit.

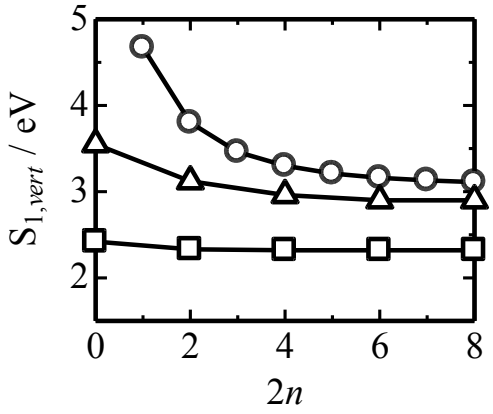

Figure 4-A1. Vertical transition energy of $F0_{2n}$ (open circles), $F0_n$-PDA-$F0_n$ (open triangles), and $F0_n$-ADA-$F0_n$ (open squares) calculated with TD-DFT/B3LYP level at the 6-31G(d,p) basis set against the number of fluorene units n.

4.6.2. Dependence of Emission Spectra on Solvent Polarity. The charge transfer (CT) character in the singlet excited state was examined by measuring the emission spectra of F8-PDA and F8-ADA in various solutions using solvents with different polarity. The solvent polarity dependence can be quantitatively well described by the Lippert–Mataga formula as Eq. 4-A1[28–31]

$$\begin{aligned}\tilde{\nu}_e &= \text{const} - \frac{1}{4\pi\varepsilon_0}\frac{2}{hc\rho^3}\left(\boldsymbol{\mu}_\text{e} - \boldsymbol{\mu}_\text{g}\right)^2\left(\frac{\varepsilon_r - 1}{2\varepsilon_r + 1} - \frac{1}{2}\frac{n^2 - 1}{2n^2 + 1}\right) \\ &= \text{const} - \frac{1}{4\pi\varepsilon_0}\frac{2}{hc\rho^3}\left(\boldsymbol{\mu}_\text{e} - \boldsymbol{\mu}_\text{g}\right)^2 f(\varepsilon_r, n)\end{aligned} \tag{4-A1}$$

where $\tilde{\nu}_\text{e}$ is the wavenumber of emission maximum, ε_0 is the vacuum permittivity, h is the Planck constant, c is the velocity of light, ρ is the radius of a spherical solute, $\boldsymbol{\mu}_\text{e}$ and $\boldsymbol{\mu}_\text{g}$ is the dipole moment of the solute in the excited and ground state, respectively, ε_r is the dielectric constant of the solvent, and n is the refractive index of the solvent. Figure 4-A2 shows the Lippert–Mataga plots of the emission for F8-PDA and F8-ADA in various solvents. Assuming the radius of solute ρ to be 5 Å, the dipole moment change was evaluated to be 14.4 for F8-PDA and 7.9 D for F8-ADA. Clearly, the maximum emission wavenumber of F8-PDA was more sensitive to the solvent polarity compared to F8-ADA. Thus, it is concluded that the singlet excited state in F8-PDA has a CT character while that of F8-ADA is rather neutral.

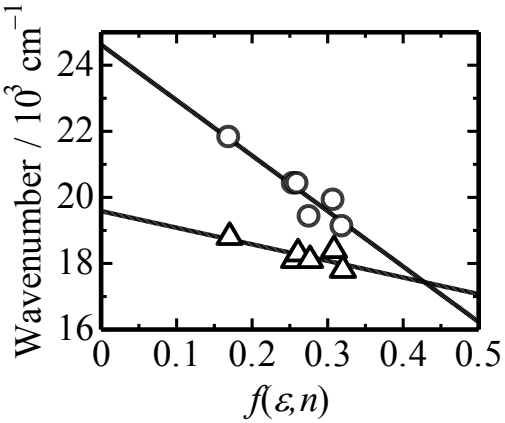

Figure 4-A2. Lippert–Mataga plots of F8-PDA (open circles) and F8-ADA (open triangles) fluorescence at room temperature. The solid lines represent the best fitting results with Eq. 4-A1. The solvents employed here are toluene, chloroform, chlorobenzene, *o*-dichlorobenzene, tetrahydrofuran, and dichloromethane from left to right.

4.6.3. Fluorescence Decay. Figure 4-A3 shows the fluorescence decay curves of F8-PDA and F8-ADA films measured by the time-correlated single-photon-counting (TCSPC) method at room temperature. The detection wavelengths were 460 nm for F8-PDA and 530 nm for F8-ADA. The fluorescence decay curve of F8-PDA was fitted with the sum of four exponential functions, while that of F8-ADA can be fitted with one exponential function. The fluorescence lifetime was evaluated to be 1.7 ns on average for F8-PDA and 11.2 ns for F8-ADA. Note that neither F8-PDA nor F8-ADA exhibited remarkable temperature dependence of the fluorescence lifetimes, suggesting that non-radiative decay channels k_{nr} is much smaller than radiative decay k_r and intersystem crossing k_{ISC}.

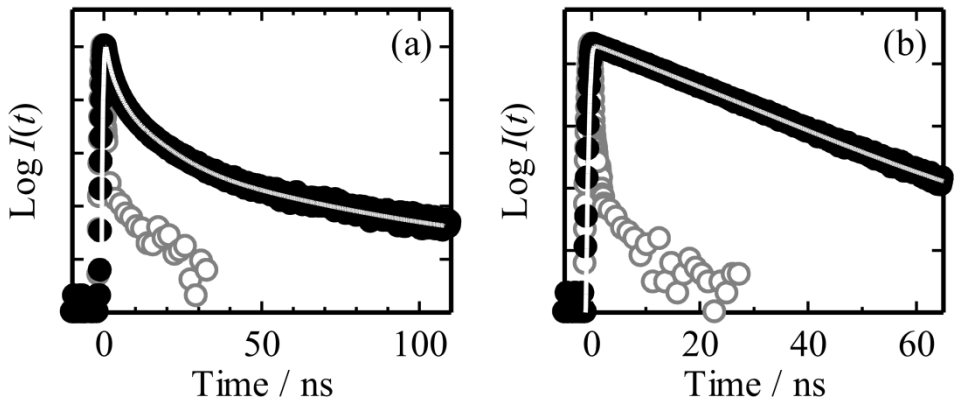

Figure 4-A3. Fluorescence decay curves of (a) F8-PDA and (b) F8-ADA films. The black circles represent the fluorescence decays. The gray circles are the instrument response function for the TCSPC measurement. The solid lines represent the best fitting curves with (a) four or (b) one exponential functions. The lifetime (the fraction) were 650 ps (60.0%), 2.2 ns (33.0%), 7.5 ns (6.5%), and 31 ns (0.5%) for F8-PDA and 11.2 ns (100%) for F8-ADA

4.6.4. Estimation of the Molar Absorption Coefficients. The molar absorption coefficient of the CT singlet exciton generated in F8-PDA was estimated as follows. Because energy transfer from the primary fluorene singlet to the CT singlet exciton occurred with a time constant of ~1.5 ps, there are only CT excitons at 10 ps after the laser excitation. In this time domain, singlet exciton deactivation can be ignored because the fluorescence lifetime of F8-PDA is much longer than 10 ps as mentioned above. Therefore, the molar absorption coefficient of the CT exciton is directly estimated by using

Beer–Lambert law: $N(t)= \Delta OD(t)\ N_A\ (1000\varepsilon l)^{-1}$ where N_A is the Avogadro's constant, ε is the molar absorption coefficient, and l is the film thickness. The exciton density at 10 ps was estimated from the film absorbance at 400 nm and the excitation photon density. From Figure 4-4a, the molar absorption coefficient of F8-PDA at 780 nm was estimated to be $4.2 \times 10^4\ M^{-1}\ cm^{-1}$.

The molar absorption coefficient of triplet exciton generated in F8-ADA was estimated as follows. First, the molar absorption coefficient of ADA in the ground state at 480 nm, i.e., the $S_1 \leftarrow S_0$ absorption coefficient, ε_{480}, was estimated to be $1.2 \times 10^4\ M^{-1}\ cm^{-1}$ from the absorption spectrum of F8-ADA in a toluene solution as shown in Figure 4-A4a. Next, the molar absorption coefficient of triplet exciton generated in F8-ADA at 1000 nm was estimated in comparison with the ground state photobleaching of ADA by using ε_{480}. Note that the base line of the ground state photobleaching was drawn so as to smoothly connect both side of the absorption edge as shown in Figure 4-A4b. As a result, the molar absorption coefficient of triplet exciton generated in F8-ADA at 1000 nm was estimated to be $6.5 \times 10^3\ M^{-1}\ cm^{-1}$.

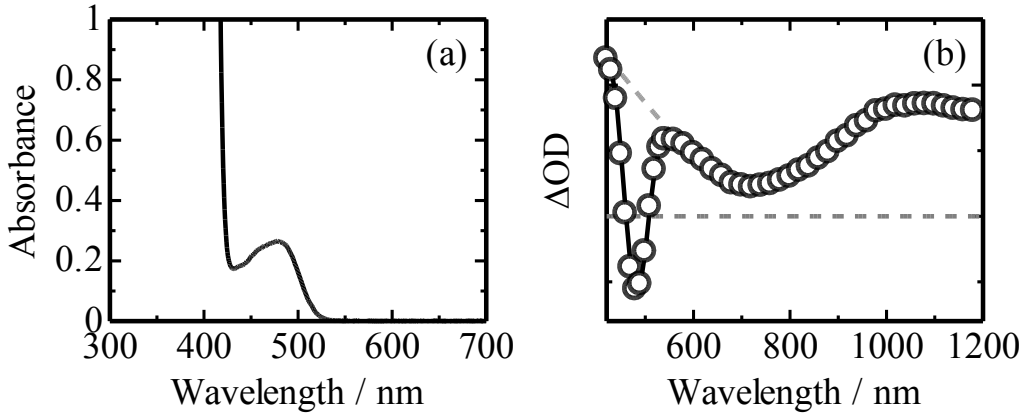

Figure 4-A4. (a) Absorption spectrum of F8-ADA in a toluene solution. (b) Transient absorption spectrum of an F8-ADA film at 150 μs after the laser excitation.

4.6.5. Singlet Energy Transfer Dynamics in F8-ADA. Figure 4-A5 shows the time evolution of transient absorption signals of F8-ADA measured at 600 and 1000 nm. The transient signals at 600 nm at an early time stage are safely assigned to the fluorene singlet excitons and well fitted with the sum of an exponential decay (2.8 ps) and a constant fraction. On the other hand, the transient signals at 1000 nm are assigned to a superposition of those of the fluorene and the ADA singlet excitons at an early time stage, as shown in Figure 4-4b. The time evolution of the ADA excitons was extracted by subtracting the transient signals at 600 nm (open circles) from those at 1000 nm (open triangles) after the initial signal at 0 ps is normalized. The time evolution extracted (closed squares) was well fitted with the sum of an exponential rise (2.9 ps) and a constant fraction, which was in good agreement with the decay constant of fluorene singlet excitons. This agreement in the rise and decay constants indicates that the ADA exciton is generated through rapid energy transfer from the fluorene singlet exciton.

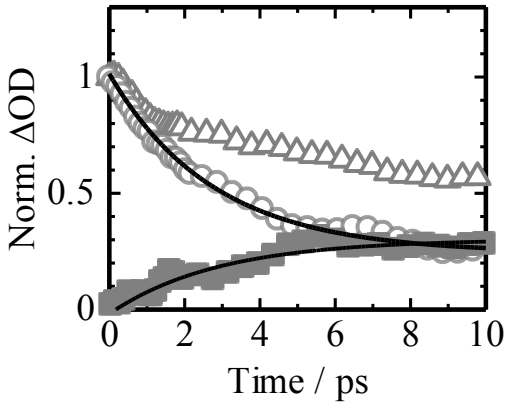

Figure 4-A5. Transient absorption signals measured at 600 nm (open circles) and 1000 nm (open triangles) of F8-ADA films excited at 400 nm (7.5 μJ cm^{-2}). The closed squares show the rise fraction at 1000 nm that is evaluated by subtracting the transient absorption signal of the fluorene singlet excitons at 600 nm (open circles) from that at 1000 nm (open triangles) after the initial signal at 0 ps is normalized. The transient signals at 600 nm were fitted with the sum of an exponential decay and a constant fraction: $\Delta OD(t) = A_d \exp(-t/\tau_d) + B$. The time evolution extracted (closed squares) was fitted with the sum of an exponential rise and a constant fraction: $\Delta OD(t) = A_r \exp(-t/\tau_r) + B$. The solid lines represent the best fitting curves.

4.6.6. Estimation of the ISC Quantum Efficiency in F8-PDA. The solutions of Eq. 4-1 is given by

$$N_{\mathrm{S}} = N_{\mathrm{S0}}\exp(-kt)$$
$$N_{\mathrm{T}} = \frac{k_{\mathrm{ISC}}}{k} N_{\mathrm{S0}}[1 - \exp(-kt)] \quad \text{(4-A2)}$$

where N_{S0} is the initial singlet exciton density. From Figure 4-7, the following relation is obtained

$$\Delta\mathrm{OD}_{\mathrm{T}\infty} = 0.4 \times \Delta\mathrm{OD}_{\mathrm{S0}} \quad \text{(4-A3)}$$

where ΔOD_S and ΔOD_T are the optical density (OD) due to singlet and triplet excitons at 780 nm, respectively, and the index 0 and ∞ represent t = 0 and sufficiently large t compared to singlet excitons lifetime (but sufficiently small compared to triplet excitons lifetime), respectively. The amplitude in the OD is proportional to the product of the number density of transient species and their molar absorption coefficients. Describing the molar absorption coefficients as ε_S and ε_T, Eq. 4-A3 can be replaced by Eq. 4-A4.

$$\varepsilon_{\mathrm{T}} \frac{k_{\mathrm{ISC}}}{k} N_{\mathrm{S0}} = 0.4 \times \varepsilon_{\mathrm{S}} N_{\mathrm{S0}}$$
$$\frac{k_{\mathrm{ISC}}}{k} = 0.4 \times \frac{\varepsilon_{\mathrm{S}}}{\varepsilon_{\mathrm{T}}} \quad \text{(4-A4)}$$

The molar absorption coefficient of the CT exciton at 780 nm was estimated to be 4.2×10^4 M^{-1} cm^{-1} as mentioned above. Assuming the molar absorption coefficient of fluorene triplet excitons to be 5×10^4 M^{-1} cm^{-1},[33] the ISC quantum efficiency in F8-PDA was estimated to be 0.34.

4.6.7. Triplet Exciton Decay Dynamics in F8-F6. Figure 4-A6 shows the time evolution of F8-F6 triplet excitons measured at 800 nm at a fluence of ~40 μJ cm^{-2}. For the quantitative discussion, the transient signals ΔOD(t) were converted into the number density of triplet excitons $N(t)$ according to the Beer–Lambert law: $N(t) = \Delta OD(t)\ N_A\ (1000\varepsilon l)^{-1}$ where N_A is the Avogadro's constant, ε is the molar absorption coefficient (5×10^4 M^{-1} cm^{-1}),[S7] and l is the film thickness. From the best fitting result with Eq. 4-6, the collision rate γ_{TTC} and diffusion coefficient D were estimated to be 2.0×10^{-11} cm^3 s^{-1} and 7.9×10^{-6} cm^2 s^{-1}, respectively. From the diffusion coefficient and the triplet exciton lifetime, the triplet exciton diffusion length $L_D = (D\tau)^{1/2}$ was estimated to be 50 nm.

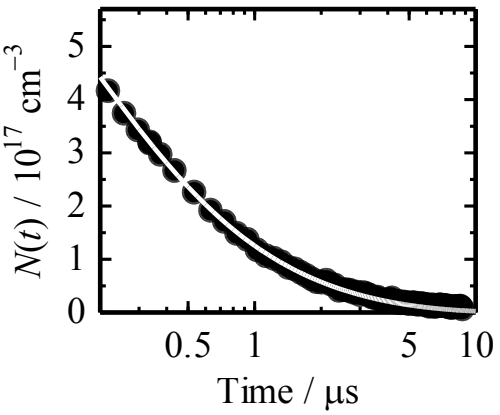

Figure 4-A6. Transient absorption decay of F8-F6 at 800 nm (fluence ~40 μJ cm^{-2}). The transient signals ΔOD(t) were converted into the number density of triplet excitons $N(t)$ according to the Beer–Lambert law: $N(t) = \Delta OD(t)\ N_A\ (1000\varepsilon l)^{-1}$. The solid lines represent the best fitting curves with Eq. 4-6.

References

(1) Pope, M.; Swenberg, C. E. *Electronic Processes in Organic Crystals and Polymers*; Oxford University Press: Oxford, U.K., 1999.

(2) Köhler, A.; Bässler, H. *Mater. Sci. Eng. R* **2009**, *66*, 71–109.

(3) Wilson, J. S.; Dhoot, A. S.; Seeley, A. J. A. B.; Khan, M. S.; Köhler, A.; Friend, R. H. *Nature* **2001**, *413*, 828–831.

(4) Wohlgenannt, M.; Jiang, X. M.; Vardeny, Z. V.; Janssen, R. A. J. *Phys. Rev. Lett.* **2002**, *88*, 197401.

(5) Carvelli, M.; Janssen, R. A. J.; Coehoorn, R. *Phys. Rev. B* **2011**, *83*, 075203.

(6) Kondakov, D. Y.; Pawlik, T. D.; Hatwar, T. K.; Spindler, J. P. *J. Appl. Phys.* **2009**, *106*, 124510.

(7) Wallikewitz, B. H.; Kabra, D.; Gélinas, S.; Friend, R. H. *Phys. Rev. B* **2012**, *85*, 045209.

(8) King, S. M.; Cass, M.; Pintani, M.; Coward, C.; Dias, F. B.; Monkman, A. P.; Roberts, M. *J. Appl. Phys.* **2011**, *109*, 074502.

(9) Zhang, Y.; Forrest, S. R. *Phys. Rev. Lett.* **2012**, *108*, 267404.

(10) Palilis, L. C.; Lidzey, D. G.; Redecker, M.; Bradley, D. D. C.; Inbasekaran, M.; Woo, E. P.; Wu, W. W. *Synth. Met.* **2000**, *111–112*, 159–163.

(11) Sainova, D.; Miteva, T.; Nothofer, H. G.; Scherf, U.; Glowacki, I.; Ulanski, J.; Fujikawa, H.; Neher, D. *Appl. Phys. Lett.* **2000**, *76*, 1810–1812.

(12) Marciniak, H.; Teicher, M.; Scherf, U.; Trost, S.; Riedl, T.; Lehnhardt, M.; Rabe, T.; Kowalsky, W.; Lochbrunner, S. *Phys. Rev. B* **2012**, *85*, 214204.

(13) Miteva, T.; Meisel, A.; Knoll, W.; Nothofer, H. G.; Scherf, U.; Müller, D. C.; Meerholz, K.; Yasuda, A.; Neher, D. *Adv. Mater.* **2001**, *13*, 565–570.

(14) Harkema, S.; Kicken, R. A. H. J.; Langeveld-Voss, B. M. W.; van Mensfoort, S. L. M.; de Kok, M. M.; Coehoorn, R. *Org. Electron.* **2010**, *11*, 755–766.

(15) Laquai, F.; Hertel, D. *Appl. Phys. Lett.* **2007**, *90*, 142109.

(16) Laquai, F.; Wegner, G.; Im, C.; Bässler, H.; Heun, S. *J. Appl. Phys.* **2006**, *99*, 023712.

(17) de Vries, R. J.; van Mensfoort, S. L. M.; Shabro, V.; Vulto, S. I. E.; Janssen, R. A. J.; Coehoorn, R. *Appl. Phys. Lett.* **2009**, *94*, 163307.

(18) Nicolai, H. T.; Hof, A. J.; Lu, M.; Blom, P. W. M.; de Vries, R. J.; Coehoorn, R. *Appl. Phys. Lett.* **2011**, *99*, 203303.

(19) Kraabel, B.; Moses, D.; Heeger, A. J. *J. Chem. Phys.* **1995**, *103*, 5102–5108.

(20) Burrows, H. D.; de Melo, J. S.; Serpa, C.; Arnaut, L. G.; Monkman, A. P.; Hamblett, I.; Navaratnam, S. *J. Chem. Phys.* **2001**, *115*, 9601–9606.

(21) Huang, Y.-F.; Chen, H.-L.; Ting, J. W.; Liao, C.-S.; Larsen, R. W.; Fann, W. *J. Phys. Chem. B* **2004**, *108*, 9619–9622.

(22) King, S.; Rothe, C.; Monkman, A. *J. Chem. Phys.* **2004**, *121*, 10803–10808.

(23) King, S. M.; Matheson, R.; Dias, F. B.; Monkman, A. P. *J. Phys. Chem. B* **2008**, *112*, 8010–8016.

(24) Petrozza, A.; Fazzi, D.; Avilov, I.; Beljonne, D.; Friend, R. H.; Kim, J.-S. *J. Phys. Chem. C* **2012**, *116*, 11298–11305.

(25) Monkman, A.; Rothe, C.; King, S.; Dias, F. *Adv. Polym. Sci.* **2008**, *212*, 187–225.

(26) Granovsky, A. A. Firefly version 7.1.G, www http://classic.chem.msu.su/gran/firefly/index.html.

(27) Schmidt, M. W.; Baldridge, K. K.; Boatz, J. A.; Elbert, S. T.; Gordon, M. S.; Jensen, J. H.; Koseki, S.; Matsunaga, N.; Nguyen, K. A.; Su, S.; Windus, T. L.; Dupuis, M.; Montgomery, J. A. *J. Comput. Chem.* **1993**, *14*, 1347–1363.

(28) Lippert, V. E. *Z. Naturforsch.* **1955**, *10A*, 541–545.

(29) Lippert, V. E. *Z. Elektrochem.* **1957**, *61*, 962–975.

(30) Mataga, N.; Kaifu, Y.; Koizumi, M. *Bull. Chem. Soc. Jpn.* **1955**, *28*, 690–691.

(31) Mataga, N.; Kaifu, Y.; Koizumi, M. *Bull. Chem. Soc. Jpn.* **1956**, *29*, 465–470.

(32) Stevens, M. A.; Silva, C.; Russell, D. M.; Friend, R. H. *Phys. Rev. B* **2001**, *63*, 165213.

(33) Cadby, A. J.; Lane, P. A.; Mellor, H.; Martin, S. J.; Grell, M.; Giebeler, C.; Bradley, D. D. C. *Phys. Rev. B* **2000**, *62*, 15604–15609.

(34) Hayer, A.; Khan, A. L. T.; Friend, R. H.; Köhler, A. *Phys. Rev. B* **2005**, *71*, 241302.

(35) Turro, N. J. *Modern Molecular Photochemistry*; University Science Books: Sausalito, CA, 1978.

(36) Nijegorodov, N. I.; Downey, W. S. *J. Phys. Chem.* **1994**, *98*, 5639–5643.

(37) Nijegorodov, N.; Vasilenko, V.; Monowe, P.; Masale, M. *Spectrochim. Acta A* **2009**, *74*, 188–194.

(38) Adams, J. E.; Mantulin, W. W.; Huber, J. R. *J. Am. Chem. Soc.* **1973**, *95*, 5477–5481.

(39) Haink, H. J.; Huber, J. R. *Chem. Phys. Lett.* **1976**, *44*, 117–120.

(40) Sarkar, A.; Chakravorti, S. *J. Lumin.* **1998**, *78*, 205–211.

(41) Beljonne, D.; Shuai, Z.; Pourtois, G.; Brédas, J. L. *J. Phys. Chem. A* **2001**, *105*, 3899–3907.

(42) Schmidt, K.; Brovelli, S.; Coropceanu, V.; Beljonne, D.; Cornil, J.; Bazzini, C.; Caronna, T.; Tubino, R.; Meinardi, F.; Shuai, Z.; Brédas, J. L. *J. Phys. Chem. A* **2007**, *111*, 10490–10499.

(43) Wu, C.; Djurovich, P. I.; Thompson, M. E. *Adv. Funct. Mater.* **2009**, *19*, 3157–3164.

(44) Chandrasekhar, S. *Rev. Mod. Phys.* **1943**, *15*, 1–89.

(45) Mozumder, A.; Pimblott, S. M. *Chem. Phys. Lett.* **1990**, *167*, 542–546.

(46) Johnson, R. C.; Merrifield, R. E. *Phys. Rev. B* **1970**, *1*, 896–902.

(47) Suna, A. *Phys. Rev. B* **1970**, *1*, 1716–1739.

(48) Laquai, F.; Park, Y.-S.; Kim, J.-J.; Basché, T. *Macromol. Rapid Commun.* **2009**, *30*, 1203–1231.

(49) Buettner, A. V. *J. Phys. Chem.* **1964**, *68*, 3253–3259.

(50) Grellmann, K. H.; Scholz, H.-G. *Chem. Phys. Lett.* **1979**, *62*, 64–71.

(51) Heinzelmann, W.; Labhart, H. *Chem. Phys. Lett.* **1969**, *4*, 20–24.

(52) Nisoli, M.; Stagira, S.; Zavelani-Rossi, M.; De Silvestri, S.; Mataloni, P.; Zenz, C. *Phys. Rev. B* **1999**, *59*, 11328–11332.

(53) Azuma, H.; Kobayashi, T.; Shim, Y.; Mamedov, N.; Naito, H. *Org. Electron.* **2007**, *8*, 184–188.

(54) Varetto, U.; MOLEKEL 5.4.; Swiss National Supercomputing Centre: Lugano, Switzerland.

Part II

Chapter 5

Singlet Fission in Poly(9,9'-di-*n*-octylfluorene) Films

5.1. Introduction

Singlet fission is an interconversion process in which one singlet excited state delocalized over neighboring two chromophore units is converted into two triplet excited states.[1,2] Because of the potential to improve the efficiency in organic photovoltaics (OPVs) by multiple exciton generation from one photon,[3–9] the singlet fission has attracted increasing attention recently. Since the first report of singlet fission in anthracene crystals,[10] a lot of experimental and theoretical studies have been published for various molecular crystals such as larger polyacenes (tetracene, pentacene).[2,11–18] In contrast, singlet fission in conjugated polymers has been reported only for limited materials,[2,19–26] and hence is not fully understood.

A clear morphology dependence of singlet fission has been reported for poly(3-hexylthiophene) (P3HT) films previously.[26] In regiorandom P3HT (RRa-P3HT) films, $2E(T_1)$ is slightly higher than $E(S_1)$, and hence singlet fission occurs not from the lowest singlet excited state but from a higher singlet excited state, which is generated by singlet–singlet annihilation (SSA). Interestingly, no triplet excitons are observed in regioregular P3HT (RR-P3HT) crystalline films. This is in sharp contrast with the singlet fission in small molecules, which is usually more efficient in molecular crystals rather than in less ordered films.[27,28] The absence of singlet fission in RR-P3HT crystalline films is attributed to preference polaron pair formation because of the large interchain interaction in π-stacked crystalline domains. On the other hand, both singlet fission and polaron pair formation have been reported for ladder-type poly(*p*-phenylene) (MeLPPP).[23,24,29] However, the limited data

reported so far are insufficient to understand the relationship between the film morphology and the efficiency of the singlet fission in conjugated polymers, and hence further investigations have been desired.

In this chapter, the singlet fission in poly(9,9'-di-*n*-octylfluorene) (PFO, the chemical structure is shown in the inset of Figure 5-1) films by transient absorption spectroscopy. Focusing on the morphology dependence of the fission efficiency, the singlet fission in disordered amorphous PFO films and in ordered PFO films with β phase, in which the conjugated main chains are planarly extended and aligned is studied.[30–32] The author performs spectroscopic analysis of triplet exciton formation and studies the decay dynamics in amorphous and β-PFO films. On the basis of these analyses, the morphology dependence of singlet fission in conjugated polymer films is discussed.

5.2. Results

5.2.1. Absorption and Photoluminescence Spectra. As shown in Figure 5-1a, the PFO film prepared from chloroform exhibited a featureless absorption band at around 390 nm, which is characteristic of amorphous PFO films. In contrast, the PFO film prepared from chloroform with a 1,8-diiodooctane (DIO) additive showed a large absorption at around 400 nm and an additional sharp absorption at around 440 nm. The sharp absorption at 440 nm is ascribed to the β-phase absorption in the film as reported previously.[33] Hereafter, this film is abbreviated as the β-PFO film. The β-phase absorption band is more pronounced with increasing concentration of the DIO additive.[34] In this study, the β-phase volume fraction was fixed to about 35% to balance high β-phase fraction and film smoothness. Figure 5-1b shows the fluorescence spectra of amorphous and β-PFO films. The amorphous PFO film exhibited a fluorescence band at 420 nm, which is attributable to the fluorescence band of amorphous phase.[33] On the other hand, the β-PFO film showed a sharp 0–0 emission band at 440 nm with almost no Stokes shift, which is attributed to the β-phase emission.[33] Interestingly, no amorphous phase emission was observed at all for the β-PFO film even though the amorphous phase was selectively excited at 360 nm, suggesting rapid energy transfer from

amorphous phase to β phase as reported previously.[35,36] Figure 5-1c shows the delayed photoluminescence spectra measured at 77 K by using a mechanical chopper. As shown in the figure, two emission bands were observed at 420 and 600 nm for the amorphous PFO film and 440 and 600 nm for the β-PFO film. The emission bands at shorter wavelengths are the same as the fluorescence bands as shown in Figure 5-1b and thus ascribed to the delayed fluorescence probably because of triplet–triplet annihilation (TTA).[33] The emission bands at longer wavelengths are

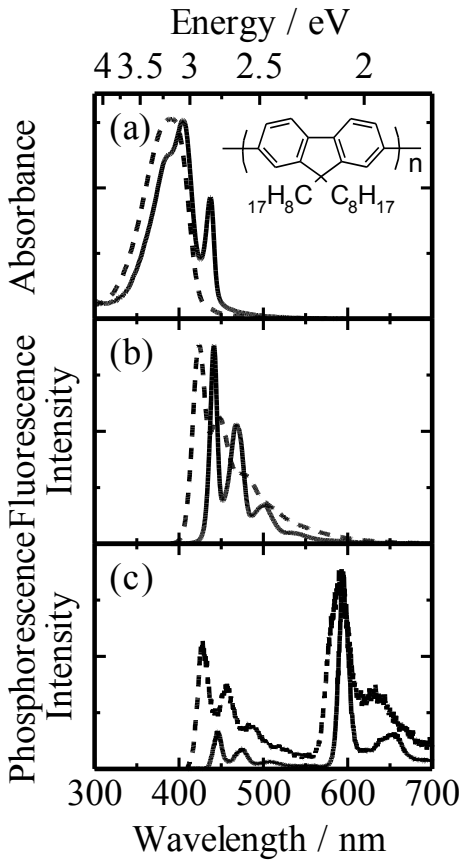

Figure 5-1. (a) Absorption, (b) fluorescence, and (c) phosphorescence spectra of amorphous PFO (broken) and β-PFO (solid) films. The photoluminescence spectra were measured with the 360 nm excitation. The phosphorescence spectra were measured at 77 K by using a mechanical chopper. The inset in panel (a) shows the chemical structure of PFO.

ascribed to the phosphorescence band of PFO films.[33] From the fluorescence and phosphorescence spectra, the energy levels of the lowest singlet and triplet excited states were estimated to be 2.93 and 2.11 eV for the amorphous PFO, and 2.81 and 2.09 eV for the *β*-PFO films, respectively.

5.2.2. Transient Absorption Spectra.

Amorphous PFO: Figure 5-2a shows the transient absorption spectra of the amorphous PFO film measured from 0 ps to 3 ns after the laser excitation at 400 nm with high excitation intensity (~60 μJ cm^{-2}). Immediately after the laser excitation, a large absorption band was observed at 800 nm and two small absorption shoulders were observed at around 600 and 1000 nm. The transient spectrum at 0 ps is in good agreement with that observed under a low excitation intensity. Thus, all the absorption bands are ascribed to singlet excitons as reported previously.[33,37] These absorption bands decayed rapidly in the picosecond time domain. At 3 ns, the small absorption shoulders disappeared but an absorption band was observed at around 800 nm, suggesting that the band at 800 nm is different from singlet excitons. This absorption band was still observed at around 800 nm even in the microsecond time domain but decayed faster under an O_2 atmosphere. Therefore, the absorption band at 800 observed after nanoseconds is ascribed to triplet excitons in amorphous PFO films as reported previously.[33,38,39] No other long-lived transients were observed under this experimental condition.

β-PFO: Figure 5-2b shows the transient absorption spectra of the *β*-PFO film measured from 0 ps to 3 ns after the laser excitation at 400 nm with high excitation intensity (~60 μJ cm^{-2}). Immediately after the laser excitation, a large absorption band was observed at 800 nm, which is the same as that of the amorphous PFO film, suggesting that singlet excitons are generated preferentially at amorphous phase in the *β*-PFO film by the 400-nm excitation. At 1 ps, this band was rapidly red-shifted to 850 nm with shoulders at 600 and 1000 nm, which is ascribed to singlet excitons in *β* phase, suggesting energy transfer from amorphous phase to *β* phase (details are described in the Appendix). Therefore, it can be safely said that singlet excitons in amorphous phase are negligible

after a few picoseconds. At 3 ns, two sharp absorption bands were observed at around 650 and at 850 nm but no shoulder was observed, suggesting that the band at 850 nm is no longer assigned to singlet excitons in the β phase. These two bands were still observed even in the microsecond time domain. The band at 850 nm decayed faster under an O_2 atmosphere. Therefore, the long-lived absorption bands at around 650 and 850 nm are assigned to polaron and triplet excitons in β-PFO films, respectively, as reported previously.[38,39]

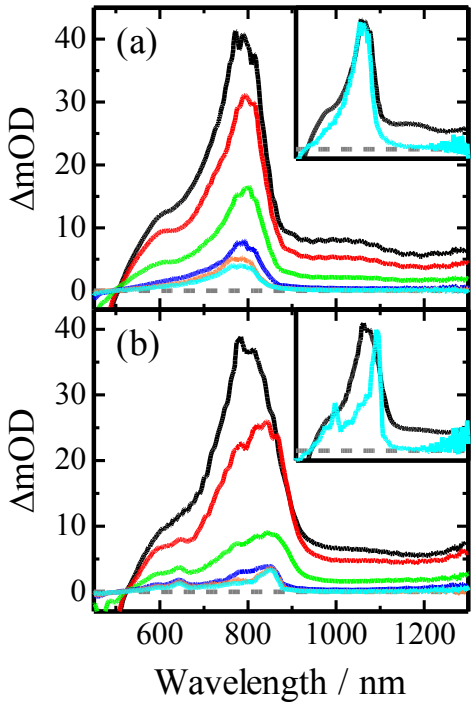

Figure 5-2. Transient absorption spectra of (a) amorphous PFO and (b) β-PFO films excited at 400 nm (~60 μJ cm^{-2}) measured at 0, 1, 10, 100, 1000, and 3000 ps after the laser excitation from top to bottom. The insets show the normalized transient absorption spectra measured at 0 and 3000 ps.

5.2.3. Transient Absorption Decays.

Amorphous PFO: In order to observe the dynamics of singlet excitons selectively, the transient absorption decay at 1050 nm was measured. As shown in Figure 5-3, the transient signals of the singlet exciton decayed faster under higher excitation intensities. The decay curve was fitted with the sum of three exponential functions: $\Delta OD(t) = A_1 \exp(-t/\tau_1) + A_2 \exp(-t/\tau_2) + A_3 \exp(-t/\tau_3)$. The fitting parameters are summarized in Table 5-1. Here, the longest lifetime τ_3 was fixed to a fluorescence lifetime of 410 ps that was evaluated by time-correlated single-photon-counting (TCSPC) method. The other two lifetimes shortened with increasing excitation intensity. The averaged lifetime of τ_1 and τ_2 is attributed to an effective deactivation time of singlet excitons through the SSA. Upon photoexcitaion under ~60 μJ cm^{-2}, the averaged lifetime was estimated to be 11 ps.

In order to extract the formation dynamics of triplet excitons, the decay fraction of singlet excitons from the transient absorption decay at 780 nm was subtracted as shown in Figure 5-4a. The triplet formation dynamics can be fitted with the sum of two exponential functions with the same time constants of τ_1 and τ_2 mentioned above. This agreement in the rise and decay dynamics of singlet and triplet excitons suggests that triplet excitons are rapidly interconverted from singlet excitons with an averaged time constant of 11 ps as will be discussed later. No contribution of τ_3 in the triplet formation dynamics indicates that the triplet formation through the intersystem crossing (ISC) is negligible because of the ISC rate as slow as $10^6 - 10^7$ s^{-1} in polyfluorene films.[40,41] Figure 5-4b shows the transient absorption decays of triplet excitons in a nanosecond range with various excitation intensities: the transient signals at 780 nm are safely ascribed to triplet excitons because no singlet excitons are survived in this time domain. The decay of the triplet exciton band was independent of the excitation intensity, and was fitted with the sum of an exponential function and a constant fraction: $\Delta OD(t) = A \exp(-t/\tau) + B$ with a lifetime of 1.7 ns and A : B = 50 : 50. The lifetime of 1.7 ns is too short to be assigned to "free" triplet excitons, which decays with a lifetime of ~3.2 μs (see the Appendix) as will be discussed later.

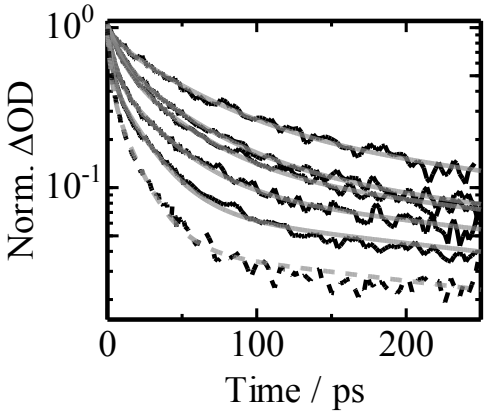

Figure 5-3. Transient absorption decays of PFO films measured at 1050 nm (solid lines: amorphous PFO films and broken line: *β*-PFO films). The excitation intensity was varied over 7, 14, 20, 40, 60 and 60 μJ cm^{-2} from top to bottom. The gray lines represent the fitting curves with the sum of three exponential functions: $\Delta OD(t) = A_1 \exp(-t/\tau_1) + A_2 \exp(-t/\tau_2) + A_3 \exp(-t/\tau_3)$ where τ_3 is fixed to a fluorescence lifetime of 410 ps (solid lines) and 390 ps (broken line) evaluated by the TCSPC method.

Table 5-1. Fitting Parameters for Transient Absorption Decays of PFO Films

Sample	Intensity / μJ cm^{-2}	$A_{1,2\text{-ave}}$ / %	$\tau_{1,2\text{-ave}}$ / ps	A_3 / %	τ_3 / ps
Amorphous PFO	7	77	43	23	410
	14	86	29	14	410
	20	87	24	13	410
	40	90	17	10	410
	60	93	11	7	410
β-PFO	60	95	8	5	390

Transient absorption decays at 1050 nm were fitted with the sum of three exponential functions: $\Delta OD(t) = A_1 \exp(-t/\tau_1) + A_2 \exp(-t/\tau_2) + A_3 \exp(-t/\tau_3)$. The longest lifetime τ_3 was fixed to a fluorescence lifetime of 410 ps for amorphous PFO and 390 ps for *β*-PFO films evaluated by the TCSPC method for all excitation intensities. The fraction $A_{1,2\text{-ave}}$ and the lifetime $\tau_{1,2\text{-ave}}$ represent the total fraction of A_1 and A_2, and the averaged lifetime of τ_1 and τ_2, respectively.

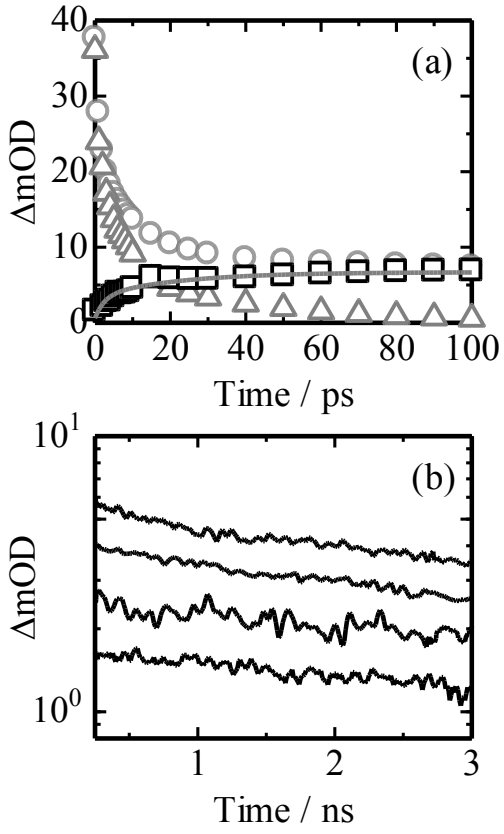

Figure 5-4. (a) Normalized transient absorption decays of amorphous PFO films excited at 400 nm (~60 μJ cm^{-2}) measured at 780 nm (open circles) and 1050 nm (singlet exciton, open triangles). The transient signals at 780 and 1050 nm were normalized at 0 ps. The open squares are obtained by subtracting the normalized transient absorption signal at 1050 nm from that at 780 nm, which represent the time evolution of triplet excitons. The solid line represents the fitting curve with the sum of two exponential functions with the same time constants of τ_1 and τ_2 in Figure 3. (b) Transient absorption decays at 780 nm observed on a time scale of nanoseconds with different fluences of 20, 30, 40, and 60 μJ cm^{-2} from bottom to top.

β-PFO Film: The dynamics of singlet excitons in *β* phase can be observed at 1050 nm selectively. As in the case of the amorphous PFO film, the *β* phase singlet exciton band also decayed faster under higher excitation intensities (in Figure 5-3, only the decay curve for an excitation intensity of ~60 μJ cm^{-2} is shown by the broken line). The decay curve was fitted with the sum of three exponential functions: $\Delta OD(t) = A_1 \exp(-t/\tau_1) + A_2 \exp(-t/\tau_2) + A_3 \exp(-t/\tau_3)$. The longest lifetime τ_3 was again fixed to a fluorescence lifetime of 390 ps that was evaluated by the TCSPC method. The averaged lifetime of the other two lifetimes was estimated to be 8 ps under ~60 μJ cm^{-2}, suggesting that the SSA proceeds more efficiently in the *β*-PFO film than in the amorphous PFO film.[42]

The formation dynamics of triplet excitons can be deduced by the same procedure as mentioned above. As shown in Figure 5-5a, the deduced formation dynamics of triplet excitons was again fitted with the sum of two exponential functions with the same time constants of τ_1 and τ_2 as fitted to the singlet decay. The coincidence in the rise and decay dynamics of singlet and triplet excitons suggests that triplet excitons are interconverted from singlet excitons as will be discussed later. Figure 5-5b shows the transient absorption decay of triplet excitons in a nanosecond range under an excitation intensity of ~60 μJ cm^{-2}. In this figure, the transient absorption decay of amorphous triplet excitons is also plotted for comparison. No decay of triplet excitons was observed for the *β*-PFO film in contrast to the distinct decay observed for the amorphous PFO film as will be discussed later.

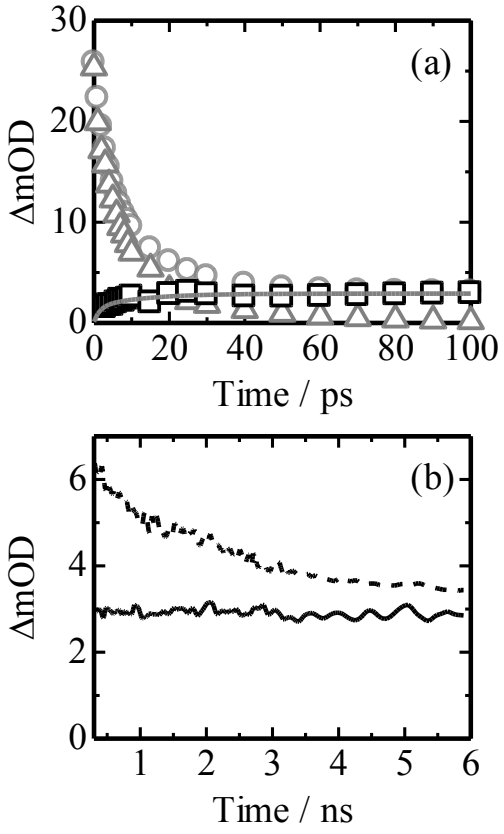

Figure 5-5. (a) Normalized transient absorption decays of *β*-PFO films excited at 400 nm (~60 μJ cm^{-2}) measured at 850 nm (open circles) and 1050 nm (singlet excitons, open triangles). The transient signals at 850 and 1050 nm were normalized at 0 ps. The open squares are obtained by subtracting the normalized transient absorption signal at 1050 nm from that at 850 nm, which represent the time evolution of triplet excitons. The solid line represents the fitting curve with the sum of two exponential functions with the same time constants of τ_1 and τ_2 in Figure 3. (b) Transient absorption decays at 850 nm on a time scale of nanoseconds under a fluence of 60 μJ cm^{-2}. The broken line represents the transient absorption decay of amorphous PFO films under the same fluence for comparison.

5.3. Discussion

5.3.1. Triplet Exciton Formation. First, the formation mechanism of triplet excitons in the amorphous PFO film is discussed. Under an excitation intensity of ~60 μJ cm^{-2}, as mentioned above, triplet excitons are rapidly interconverted from singlet excitons with a time constant of 11 ps. Such a rapid triplet exciton formation would require strong spin mixing between singlet and triplet excitons. Triplet excitons are typically generated through ISC on a time scale of nano- to microseconds, because the ISC is spin-forbidden. Indeed, the ISC rate in polyfluorenes has been reported as low as 10^6 – 10^7 s^{-1} because of the weak spin–orbit coupling.[40,41] Therefore, ultrafast triplet exciton formation observed in this study cannot be ascribed to usual ISC. Some reports suggested that the increase in triplet excitons generation yield in solid state than in solution is attributed to the charge recombination into triplet excitons.[38,43] However, this is not the case because hyperfine interaction (HFI) with nuclear magnetic moments, which plays an important role in the interconversion mechanism in organic radicals, is also too weak to explain such a rapid spin flip in picoseconds. A HFI value of ~5 mT reported for PFO[44] corresponds to an interconversion time of several nanoseconds, which is two orders of magnitude slower than the triplet formation time observed in this study. In other words, polaron pairs still conserve singlet spin state within a few picoseconds, and hence singlet state would be preferentially regenerated by the recombination of polaron pairs in this time domain. Therefore, singlet fission is a most probable scheme to rationalize such a rapid triplet formation. The overall reaction from singlet to triplet exciton in singlet fission is spin-conserving and spin-allowed, and therefore can proceed on a time scale of femto- to picoseconds.[2]

Next, the energetics for the rapid triplet exciton formation due to singlet fission is discussed. For efficient singlet fission, the singlet excited state energy should be higher than twice the triplet excited state energy $E(S) > 2E(T)$. As mentioned before, the energy levels of the lowest singlet and triplet excited states were estimated to be 2.93 and 2.11 eV, respectively. In other words, the singlet fission from the lowest singlet excited state is highly endothermic and hence is thermodynamically unfavorable. Furthermore, the lowest singlet excited state under high excitation intensities is

Scheme 5-1. Energy Diagrams for Singlet Fission in PFO Films

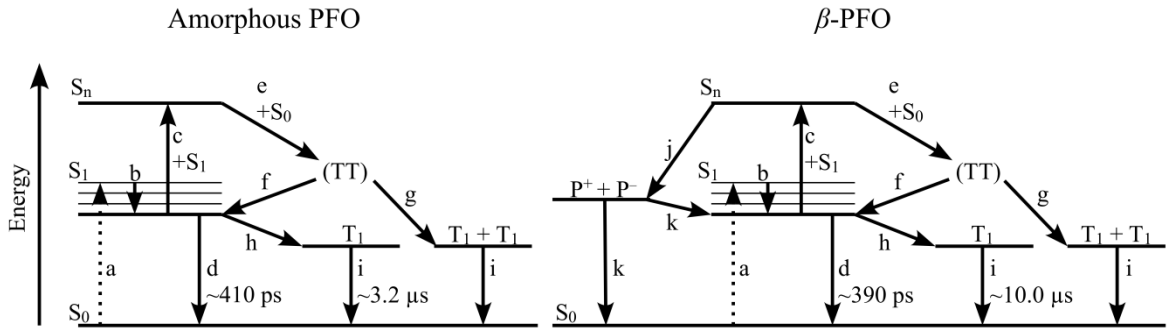

Key: (a) photon absorption, (b) vibrational relaxation, (c) singlet–singlet annihilation (SSA, singlet fusion), (d) radiative and non-radiative deactivations, (e) singlet fission, (f) back recombination of triplet pairs through triplet–triplet annihilation (TTA, triplet fusion), (g) triplet pair dissociation, (h) intersystem crossing (k_{ISC}), (i) monomolecular triplet deactivation, (j) polaron formation, (k) polaron recombination.

strongly quenched through the SSA. If the annihilation deactivates merely singlet excitons and is not related to the formation of triplet excitons, the formation yield of triplet excitons should be suppressed with increasing excitation intensity. However, triplet excitons are more efficiently formed at higher excitation intensities (see the Appendix), suggesting that triplet excitons are efficiently generated from a higher singlet excited state S_n formed by the SSA (singlet fusion). This singlet fusion followed by the singlet fission is thermodynamically favorable because $E(S_n) > 2E(T)$, which has been reported for several materials previously.[26,45–47] Therefore it is concluded that the rapid triplet exciton formation is attributed to the singlet fusion followed by the singlet fission into triplet excitons as shown in Scheme 1. Ultrafast formation of the long-lived transients in PFO film at the same spectral position was previously observed by Friend et al.[37] They also pointed out the possibility of triplet excitons generation through hot singlet fission.

5.3.2. Triplet Exciton Deactivation. As shown in Figure 5-4b, about 50% of triplet excitons are deactivated with a lifetime of 1.7 ns. This lifetime is too short to be assigned to "free" triplet excitons because the lifetime of "free" triplet excitons is as long as 3.2 μs. A simple scheme for the singlet fusion followed by the singlet fission is given by Eq. 5-1[1,2]

$$S_n + S_0 \underset{k_2}{\overset{k_{-2}}{\rightleftarrows}} (TT) \underset{k_1}{\overset{k_{-1}}{\rightleftarrows}} T_1 + T_1 \qquad (5\text{-}1)$$

where (TT) is an intermediate pair state (triplet pair state). In this state, triplet excitons are assumed to be close enough to collide with each other whose spin functions are coupled into a pure singlet state. The reverse reaction of singlet fission is equivalent to the TTA, and thus is also spin-allowed for the same reason. Therefore, this rapid decay is attributed to the back reaction of triplet excitons into two singlet states through the TTA.[1,26,41,48–50] As shown in Figure 5-4b, the deactivation time of triplet excitons was independent of the excitation intensity, suggesting that two triplet excitons generated by singlet fission are still close to each other in this time domain and hence can be considered as a pair state. In other words, 50% of the triplet pair states deactivates geminately through the intensity-independent TTA. On the other hand, the rest of triplet excitons (~50%) remain constantly. The constant component is ascribed to dissociated free triplet excitons, which would survive for even as long as microseconds. It should be noted that Figures 5-4 and 5 show the formation and decay dynamics of not "dissociated free triplet" but "triplet pair". It was also assumed that spectroscopic properties of the triplet pair state such as the transient absorption spectra and the molar absorption coefficient are identical to those of free triplet excitons because the interaction between a pair of two triplet excitons is considered to be very weak.[1,2] The relatively short lifetime of triplet excitons is indicative of the triplet formation via singlet fission because if triplet excitons was formed through the ISC or recombination of polaron pairs, they would be "free" and hence should have a long lifetime of microseconds.

5.3.3. Morphology Dependence of Singlet Fission Efficiency. This section deals with the singlet fusion followed by the triplet pair formation: $S_1 + S_1 \rightarrow S_n + S_0 \rightarrow (TT)$. As shown in Figure 5-3, the higher singlet excited state S_n is formed more efficiently in the *β*-PFO than in the amorphous PFO film. On the other hand, as shown in Figures 5-4 and 5-5, the triplet pair formation is about two times more efficient in the amorphous PFO than in the *β*-PFO film, indicating that the singlet fission from the S_n state is more efficient in the amorphous PFO rather than in the ordered *β*-PFO film, which is in sharp contrast to the singlet fission in small molecules: singlet fission is typically more efficient in molecular crystals than in less ordered films.[27,28] The decrease in the fission efficiency in the *β*-PFO film is attributable to the presence of another relaxation pathway from the S_n state. As shown in Figure 5-2b, polarons are additionally generated in the *β*-PFO film. Assuming that the molar absorption coefficients of triplet exciton and polaron are in the same order of $5 - 6 \times 10^4$ M^{-1} cm^{-1} as reported previously,[38,51] the formation rate of triplet pairs is estimated to be almost the same as that of polarons in the *β*-PFO film. This is in good agreement with about a two times lower triplet pair formation yield in the *β*-PFO film than in the amorphous PFO film. Therefore, the decrease in the triplet pair formation efficiency in ordered *β*-PFO films is attributed to the comparably efficient polaron formation (Scheme 1). This finding is consistent with the previous study on triplet formation in amorphous RRa-P3HT and crystalline RR-P3HT films: triplet excitons are efficiently generated through singlet fission in RRa-P3HT while no triplet excitons are generated in RR-P3HT films but instead polaron pairs are preferentially generated.[26] The efficient charge generation in *β*-PFO and RR-P3HT is probably attributed to the larger interchain interaction in ordered phases.

Next, moves onto the triplet pair dissociation into two free triplet excitons, $(TT) \rightarrow T_1 + T_1$. As shown in Figure 5-5b, about a half of triplet pairs are deactivated in the amorphous PFO film through the TTA with a time constant of 1.7 ns, while no triplet pair decay is observed in the *β*-PFO film. In other words, the triplet pair dissociation is more efficient in the *β*-PFO than in the amorphous PFO film, although the triplet pair formation is two times more efficient in the

amorphous PFO than in the *β*-PFO film as mentioned above. As a result, the overall triplet generation yield is comparable in these films. In the triplet pair dissociation, the triplet exciton diffusion plays a key role as reported previously.[48–50] In an extreme case, the triplet excitons are easily deactivated through the TTA in a covalently linked tetracene dimer although the efficient triplet dissociation is observed in tetracene single crystals.[49,50] Owing to the planner conformation in the *β*-PFO film, the triplet exciton diffusion coefficient would be larger in the *β*-PFO film than in amorphous PFO films because of the larger intrachain and interchain electronic couplings in the *β*-PFO film, which is beneficial for the Dexter energy transfer.[1,41,52] Therefore it is concluded that the efficient triplet pair dissociation in *β*-PFO is due to the larger triplet exciton diffusion coefficient. In summary, the triplet pair formation efficiency is more efficient in amorphous PFO than in ordered *β*-PFO films because of a competitive relaxation pathway of the efficient charge generation in *β*-PFO film. On the other hand, the triplet pair dissociation is more efficient in *β*-PFO than in amorphous PFO films because of larger triplet exciton diffusion coefficient in ordered phases.

5.3.4. Material Design for Efficient Singlet Fission in Conjugated Polymers. Most of the singlet fission mechanisms reported for conjugated polymers is the singlet fission not from the lowest singlet excited state but from a hot singlet excited state.[19–26] This is in contrast to the singlet fission in molecular crystals such as tetracene, and pentacene,[2,11–18] which occurs from the lowest singlet excited state efficiently. This is probably due to the small energy gap between the lowest singlet excited state (S_1 state) and the lowest triplet state (T_1 state) ΔE_{ST} in conjugated polymers with delocalized π system more than in small molecules. In such a case, the energy level of the S_1 state is lower than twice that of the T_1 state: the singlet fission from the S_1 state is thermodynamically unfavorable and hence inefficient. As described above, the singlet fission from a higher singlet excited state is in competition with polaron generation. This is because higher singlet excited states generally are more mixed with charge transfer states. Indeed, efficient polaron formations from higher singlet excited states have been reported for many conjugated polymers.[1,26,29,38,53,54] The

author therefore proposes that the singlet fission from the S_2 state would be an alternative for conjugated polymers. For example, some low-bandgap polymers have the S_1 band at around 800 nm (1.55 eV) and the S_2 band at around 400 nm (3.1 eV). The T_1 state is roughly estimated to be ~1 eV assuming that ΔE_{ST} is 0.5 eV. Thus, the singlet fission from the S_2 state is thermodynamically possible ($E(S_2) \geq 2E(T_1)$). Considering the high triplet exciton diffusion required for efficient dissociation into two triplets, low-bandgap crystalline polymers would be suitable for efficient singlet fission in conjugated polymers.

5.4. Conclusions

In this chapter, the singlet fission dynamics in PFO films was studied by transient absorption spectroscopy. Under an excitation intensity of ~60 μJ cm^{-2}, triplet excitons are rapidly interconverted from singlet excitons with a time constant of 11 ps in amorphous PFO and 8 ps in *β*-PFO films, which is too fast to be assigned to ISC from singlet to triplet excitons or the recombination from singlet polaron pairs to triplet excitons. Therefore, singlet fission is a most probable scheme to rationalize such a rapid triplet exciton formation. From the excitation intensity dependence of the triplet exciton formation efficiency, it is concluded that the rapid triplet exciton formation in PFO films is attributed to singlet fission from a higher singlet excited state S_n formed by the SSA (singlet fusion). The triplet pair formation efficiency is about two times more efficient in amorphous PFO than in ordered *β*-PFO films because of a competitive relaxation pathway of the efficient charge generation in *β*-PFO films. On the other hand, the triplet pair dissociation efficiency is more efficient in *β*-PFO than in amorphous PFO films because of larger triplet exciton diffusion coefficient in ordered phase. As a result, the overall triplet generation yield is comparable in these films. For efficient singlet fission in conjugated polymers, the author proposes that low-bandgap crystalline polymers would be suitable for efficient singlet fission in conjugated polymers.

5.5. Experimental Section

Sample Preparation. PFO was purchased from American Dye Source, Inc. and used without further purification. Amorphous PFO films were prepared by spincoating from chloroform solution and *β*-PFO films were prepared by spincoating from chloroform solution with an additive of 1,8-diiodooctane (DIO) (2% by volume). For transient absorption measurements, a sapphire substrate was used to prevent waveguiding and amplified spontaneous emission,[55,56] while the other experiments have done with a quartz substrate. The film thickness was about 100 nm.

Measurements. UV–visible absorption and photoluminescence spectra of PFO films were measured with a UV–visible spectrophotometer (Hitachi, U-3500) and a fluorescence spectrophotometer (Hitachi, F-4500) equipped with a red-sensitive photomultiplier (Hamamatsu, R928F), respectively. Phosphorescence spectra were collected in a time domain longer than 2 ms after the excitation by using a mechanical chopper incorporated in the fluorescence spectrophotometer (Hitachi, F-4500). Photoluminescence decay was measured by the time-correlated single-photon-counting (TCSPC) method (Horiba Jobin Yvon, FluoroCube). The excitation wavelength was 375 nm. The total instrument response function is an FWHM of ca. 280 ps. A weak excitation power (~nJ cm^{-2}) was used in the measurement to prevent singlet–singlet annihilation.

Transient absorption data were collected with a pump and probe femtosecond transient spectroscopy system. This system consists of a transient absorption spectrometer (Ultrafast Systems, Helios) and a regenerative amplified Ti:sapphire laser (Spectra-Physics, Hurricane). The amplified Ti:sapphire laser provided 800 nm fundamental pulses at a repetition rate of 1 kHz with an energy of 0.9 mJ and a pulse width of 100 fs (FWHM), which were split into two optical beams with a beam splitter to generate pump and probe pulses. One fundamental beam was converted into pump pulses at 400 nm with a second harmonic generator (Spectra-Physics, TP-F). The other fundamental beam was converted into white light pulses employed as probe pulses in the wavelength region from 400 to 1700 nm. The pump pulses were modulated mechanically with a repetition rate of 500 Hz. The

temporal evolution of the probe intensity was recorded with a CMOS linear sensor (Ultrafast Systems, SPEC-VIS) for the visible measurement and with an InGaAs linear diode array sensor (Ultrafast Systems, SPEC-NIR) for the near-IR measurement. The transient absorption spectra and decays were collected over the time range from −5 ps to 6 ns. Typically, 1500 laser shots were averaged at each delay time to obtain a detectable absorbance change as small as ~10^{-4}. In order to cancel out the orientation effects on the dynamics, the polarization direction of the linearly polarized probe pulse was set at a magic angle of 54.7 ° with respect to that of the pump pulse. The sample films were sealed in a quartz cuvette purged with N_2. Note that the transient absorption spectra and dynamics were highly reproducible even after the several times measurements. In other words, the laser irradiation had negligible effects on the sample degradation at least under this experimental condition.

5.6. Appendix

5.6.1. Singlet Energy Transfer from Amorphous Phase to *β* Phase. As mentioned above, singlet excitons in *β* phase were generated by rapid energy transfer from singlet excitons in amorphous domains even after the photoexcitation of the amorphous phase. Figure 5-A1 shows the time evolution of the transient absorption signals at 875 nm of a *β*-PFO film after the 400-nm excitation with a fluence of ~1 μJ cm^{-2}. This band is assigned to singlet excitons in the *β* phase and well fitted with the sum of an exponential rise (0.3 ps) and a constant fraction. This result indicates that the time constant of the energy transfer is as short as ~0.3 ps, which is much shorter than the fluorescence lifetime of amorphous PFO film (410 ps) evaluated by the TCSPC method. Such rapid energy transfer is consistent with fully quenched amorphous fluorescence as shown in Figure 5-1.

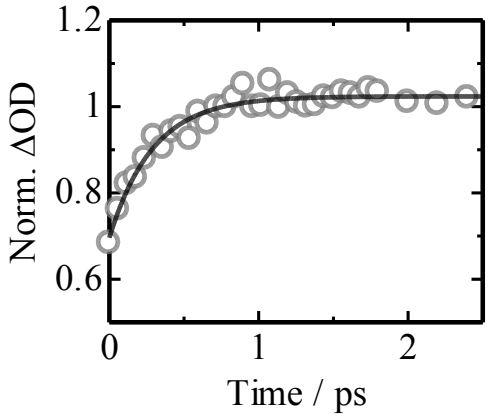

Figure 5-A1. Transient absorption signals measured at 875 nm of a *β*-PFO film excited at 400 nm (~1 μJ cm^{-2}). The transient absorption rise was fitted with the sum of an exponential function and a constant fraction: $\Delta OD(t) = A_r \exp(-t/\tau_r) + B$ with a time constant of 0.3 ps. The solid line represents the best fitting curve.

5.6.2. Triplet Exciton Lifetime. Figure 5-A2 shows the time evolution of the fluorene triplet excitons in amorphous and *β*-PFO films measured at 800 and 850 nm, respectively. Note that poly(9,9'-di-*n*-octylfluorene-*alt*-9,9'-di-*n*-hexylfluorene) (F8-F6) was used as an amorphous polyfluorene film instead of PFO. Owing to the different side chain lengths in F8-F6, the formation of the *β* phase is completely negligible in F8-F6 amorphous films. The other spectroscopic properties of F8-F6 are almost the same as that of amorphous PFO films. Under the lower excitation intensity, the transient decays were fitted with an exponential function $\Delta OD(t) = A \exp(-t/\tau_T)$ with a lifetime of $\tau_T = 3.2$ μs for F8-F6 films and $\tau_T = 10$ μs for *β*-PFO films, which is due to radiative and non-radiative monomolecular decay without bimolecular reactions.

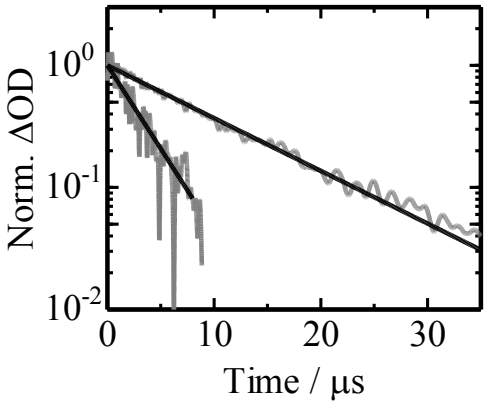

Figure 5-A2. Transient absorption signals measured at 800 nm for F8-F6 (lower) and 850 nm for *β*-PFO (upper) films. The transient absorption decays were fitted with an exponential function: $\Delta OD(t) = A \exp(-t/\tau_T)$. The solid lines represent the best fitting curves.

5.6.3. Excitation Intensity Dependence of Triplet Exciton Formation Yield. In order to discuss the mechanism of ultrafast triplet exciton formation in amorphous PFO films, the transient absorption signals of triplet excitons at 100 ps after the laser excitation at 400 nm under different intensities was measured. Figure 5-A3 shows the log–log plots of the transient absorption signals of triplet excitons observed for the amorphous PFO film against different excitation intensities. The transient absorption signals increased with increasing excitation intensity and hence well fitted with a power-law equation of $\Delta OD \propto I^m$ with a slope of $m = 2$, suggesting that there is a bimolecular reaction in the triplet exciton formation such as singlet–singlet annihilation.

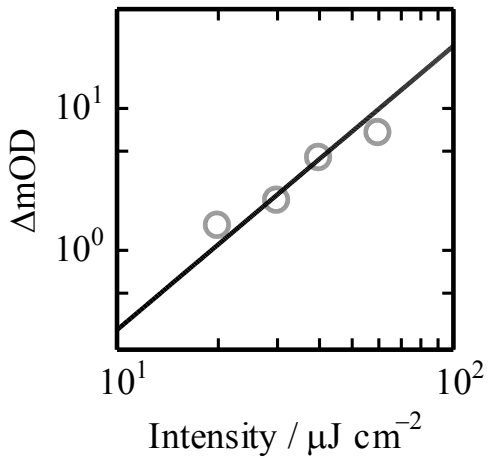

Figure 5-A3. Log–log plots of the transient absorption signals of triplet exciton in amorphous PFO films against the excitation intensity at 400 nm. The solid line represents the fitting curve with a power-law equation: $\Delta OD = I^m$ with a slope of $m = 2$.

References

(1) Pope, M.; Swenberg, C. E. *Electronic Processes in Organic Crystals and Polymers*; Oxford University Press: Oxford, U.K., 1999.

(2) Smith, M. B.; Michl, J. *Chem. Rev.* **2010**, *110*, 6891–6936.

(3) Hanna, M. C.; Nozik, A. J. *J. Appl. Phys.* **2006**, *100*, 074510.

(4) Rao, A.; Wilson, M. W. B.; Hodgkiss, J. M.; Albert-Seifried, S.; Bässler, H.; Friend, R. H. *J. Am. Chem. Soc.* **2010**, *132*, 12698–12703.

(5) Jadhav, P. J.; Mohanty, A.; Sussman, J.; Lee, J.; Baldo, M. A. *Nano Lett.* **2011**, *11*, 1495–1498.

(6) Ehrler, B.; Wilson, M. W. B.; Rao, A.; Friend, R. H.; Greenham, N. C. *Nano Lett.* **2012**, *12*, 1053–1057.

(7) Ehrler, B.; Walker, B. J.; Böhm, M. L.; Wilson, M. W. B.; Vaynzof, Y.; Friend, R. H.; Greenham, N. C. *Nat. Commun.* **2012**, *3*, 1019.

(8) Chan, W.-L.; Tritsch, J. R.; Zhu, X.-Y. *J. Am. Chem. Soc.* **2012**, *134*, 18295–18302.

(9) Ehrler, B.; Musselman, K. P.; Böhm, M. L.; Friend, R. H.; Greenham, N. C. *Appl. Phys. Lett.* **2012**, *101*, 153507.

(10) Singh, S.; Jones, W. J.; Siebrand, W.; Stoicheff, B. P.; Schneider, W. G. *J. Chem. Phys.* **1965**, *42*, 330–342.

(11) Thorsmølle, V. K.; Averitt, R. D.; Demsar, J.; Smith, D. L.; Tretiak, S.; Martin, R. L.; Chi, X.; Crone, B. K.; Ramirez, A. P.; Taylor, A. J. *Phys. Rev. Lett.* **2009**, *102*, 017401.

(12) Johnson, J. C.; Nozik, A. J.; Michl, J. *J. Am. Chem. Soc.* **2010**, *132*, 16302–16303.

(13) Burdett, J. J.; Müller, A. M.; Gosztola, D.; Bardeen, C. J. *J. Chem. Phys.* **2010**, *133*, 144506.

(14) Rao, A.; Wilson, M. W. B.; Albert-Seifried, S.; Di Pietro, R.; Friend, R. H. *Phys. Rev. B* **2011**, *84*, 195411.

(15) Burdett, J. J.; Gosztola, D.; Bardeen, C. J. *J. Chem. Phys.* **2011**, *135*, 214508.

(16) Wilson, M. W. B.; Rao, A.; Clark, J.; Kumar, R. S. S.; Brida, D.; Cerullo, G.; Friend, R. H. *J. Am. Chem. Soc.* **2011**, *133*, 11830–11833.

(17) Zimmerman, P. M.; Bell, F.; Casanova, D.; Head-Gordon, M. *J. Am. Chem. Soc.* **2011**, *133*, 19944–19952.

(18) Ma, L.; Zhang, K.; Kloc, C.; Sun, H.; Michel-Beyerle, M. E.; Gurzadyan, G. G. *Phys. Chem. Chem. Phys.* **2012**, *14*, 8307–8312.

(19) Austin, R. H.; Baker, G. L.; Etemad, S.; Thompson, R. *J. Chem. Phys.* **1989**, *90*, 6642–6646.

(20) Kraabel, B.; Hulin, D.; Aslangul, C.; Lapersonne-Meyer, C.; Schott, M. *Chem. Phys.* **1998**, *227*, 83–98.

(21) Lanzani, G.; Stagira, S.; Cerullo, G.; De Silvestri, S.; Comoretto, D.; Moggio, I.; Cuniberti, C.; Musso, G. F.; Dellepiane, G. *Chem. Phys. Lett.* **1999**, *313*, 525–532.

(22) Lanzani, G.; Cerullo, G.; Zavelani-Rossi, M.; De Silvestri, S. *Phys. Rev. Lett.* **2001**, *87*, 187402.

(23) Wohlgenannt, M.; Graupner, W.; Österbacka, R.; Leising, G.; Comoretto, D.; Vardeny, Z. V. *Synth. Met.* **1999**, *101*, 267–268.

(24) Wohlgenannt, M.; Graupner, W.; Leising, G.; Vardeny, Z. V. *Phys. Rev. B* **1999**, *60*, 5321–5330.

(25) Österbacka, R.; Wohlgenannt, M.; Shkunov, M.; Chinn, D.; Vardeny, Z. V. *J. Chem. Phys.* **2003**, *118*, 8905–8916.

(26) Guo, J.; Ohkita, H.; Benten, H.; Ito, S. *J. Am. Chem. Soc.* **2009**, *131*, 16869–16880.

(27) Marciniak, H.; Fiebig, M.; Huth, M.; Schiefer, S.; Nickel, B.; Selmaier, F.; Lochbrunner, S. *Phys. Rev. Lett.* **2007**, *99*, 176402.

(28) Marciniak, H.; Pugliesi, I.; Nickel, B.; Lochbrunner, S. *Phys. Rev. B* **2009**, *79*, 235318.

(29) Gulbinas, V.; Zaushitsyn, Y.; Bässler, H.; Yartsev, A.; Sundström, V. *Phys. Rev. B* **2004**, *70*, 035215.

(30) Grell, M.; Bradley, D. D. C.; Ungar, G.; Hill, J.; Whitehead, K. S. *Macromolecules* **1999**, *32*, 5810–5817.

(31) Chen, S. H.; Su, A. C.; Chen, S. A. *J. Phys. Chem. B* **2005**, *109*, 10067–10072.

(32) Knaapila, M.; Winokur, M. J. *Adv. Polym. Sci.* **2008**, *212*, 227–272.

(33) Monkman, A.; Rothe, C.; King, S.; Dias, F. *Adv. Polym. Sci.* **2008**, *212*, 187–225.

(34) Peet, J.; Brocker, E.; Xu, Y.; Bazan, G. C. *Adv. Mater.* **2008**, *20*, 1882–1885.

(35) Ariu, M.; Sims, M.; Rahn, M. D.; Hill, J.; Fox, A. M.; Lidzey, D. G.; Oda, M.; Cabanillas-Gonzalez, J.; Bradley, D. D. C. *Phys. Rev. B* **2003**, *67*, 195333.

(36) Khan, A. L. T.; Sreearunothai, P.; Herz, L. M.; Banach, M. J.; Köhler, A. *Phys. Rev. B* **2004**, *69*, 085201.

(37) Stevens, M. A.; Silva, C.; Russell, D. M.; Friend, R. H. *Phys. Rev. B* **2001**, *63*, 165213.

(38) Cadby, A. J.; Lane, P. A.; Mellor, H.; Martin, S. J.; Grell, M.; Giebeler, C.; Bradley, D. D. C.; Wohlgenannt, M.; An, C.; Vardeny, Z. V. *Phys. Rev. B* **2000**, *62*, 15604–15609.

(39) Hayer, A.; Khan, A. L. T.; Friend, R. H.; Köhler, A. *Phys. Rev. B* **2005**, *71*, 241302.

(40) King, S.; Rothe, C.; Monkman, A. *J. Chem. Phys.* **2004**, *121*, 10803–10808.

(41) Köhler, A.; Bässler, H. *Mater. Sci. Eng. R* **2009**, *66*, 71–109.

(42) Shaw, P. E.; Ruseckas, A.; Peet, J.; Bazan, G. C.; Samuel, I. D. W. *Adv. Funct. Mater.* **2010**, *20*, 155–161.

(43) King, S. M.; Rothe, C.; Dai, D.; Monkman, A. P. *J. Chem. Phys.* **2006**, *124*, 234903.

(44) Sheng, Y.; Nguyen, T. D.; Veeraraghavan, G.; Mermer, Ö.; Wohlgenannt, M.; Qiu, S.; Scherf, U. *Phys. Rev. B* **2006**, *74*, 045213.

(45) Katoh, R.; Kotani, M. *Chem. Phys. Lett.* **1992**, *196*, 108–112.

(46) Katoh, R.; Kotani, M.; Hirata, Y.; Okada, T. *Chem. Phys. Lett.* **1997**, *264*, 631–635.

(47) Watanabe, S.; Furube, A.; Katoh, R. *J. Phys. Chem. A* **2006**, *110*, 10173–10178.

(48) Arnold, S.; Alfano, R. R.; Pope, M.; Yu, W.; Ho, P.; Selsby, R.; Tharrats, J.; Swenberg, C. E. *J. Chem. Phys.* **1976**, *64*, 5104–5114.

(49) Müller, A. M.; Avlasevich, Y. S.; Müllen, K.; Bardeen, C. J. *Chem. Phys. Lett.* **2006**, *421*, 518–522.

(50) Müller, A. M.; Avlasevich, Y. S.; Schoeller, W. W.; Müllen, K.; Bardeen, C. J. *J. Am. Chem. Soc.* **2007**, *129*, 14240–14250.

(51) Takeda, N.; Asaoka, S.; Miller, J. R. *J. Am. Chem. Soc.* **2006**, *128*, 16073–16082.

(52) Turro, N. J. *Modern Molecular Photochemistry*; University Science Books: Sausalito, CA, 1978.

(53) Scholes, G. D. *ACS Nano* **2008**, *2*, 523–537.

(54) Dicker, G.; de Haas, M. P.; Siebbeles, L. D. A.; Warman, J. M. *Phys. Rev. B* **2004**, *70*, 045203.

(55) Nisoli, M.; Stagira, S.; Zavelani-Rossi, M.; De Silvestri, S.; Mataloni, P.; Zenz, C. *Phys. Rev. B* **1999**, *59*, 11328–11332.

(56) Azuma, H.; Kobayashi, T.; Shim, Y.; Mamedov, N.; Naito, H. *Org. Electron.* **2007**, *8*, 184–188.

Chapter 6

Selective Observation of Singlet Exciton Diffusion in Poly(3-hexylthiophene) Crystalline Domains

6.1. Introduction

Singlet excitons are primary photoexcitations formed in organic materials after photon absorption. Excitons are a coulombically bound electron–hole pair, and hence cannot contribute to the photocurrent generation but can diffuse as an electron–hole pair before the deactivation to the ground state. In donor/acceptor blend films, some excitons can reach a donor/acceptor interface by the exciton diffusion, in which they can be dissociated into free charge carriers because of the energy gap between donor and acceptor materials enough to break the Coulomb attraction, and therefore can contribute to the photocurrent generation.[1–6] Thus, the exciton diffusion length is one of the most important photophysical properties for organic solar cells. Singlet exciton dynamics has been studied for many organic molecular crystals,[7–17] but is not fully understood for conjugated polymers, in particular, crystalline polymers. For example, there is not much difference in the diffusion length of singlet excitons reported for poly(*p*-phenylene vinylene) (PPV) amorphous films, which is typically as small as 5–7 nm.[18–23] In contrast, there is a significant difference in the diffusion length of singlet exciton reported for regioregular poly(3-hexythipene) (P3HT) crystalline films (2.6–27 nm): it has been reported to be typically <10 nm on the basis of exciton quenching in donor/acceptor bilayered films[24–27] and >10 nm on the basis of singlet–singlet annihilation.[28]

In crystalline polymer films like P3HT, there should be crystalline and disordered amorphous domains at the same time. This is in sharp contrast to molecular single crystals, which have no

disordered amorphous domains. Indeed, both crystalline and disordered amorphous domains are observed for P3HT films by scanning probe microscope (SPM) and transmission electron microscope (TEM) measurements. In crystalline domains, P3HT self-organizes into two-dimensional π-stacked lamellar structures to form crystalline fibrils, which are typically 10–20 nm in width and ~10 μm in length.[29–32] As a result of the crystallization, P3HT films exhibit a red-shifted absorption band and a high hole mobility, which are beneficial for photovoltaics. Thus, optoelectronic properties of P3HT films are strongly dependent on the crystallinity.[33–35]

In this chapter, the diffusion dynamics of singlet excitons in P3HT crystalline domains is studied by transient absorption spectroscopy. To focus on the exciton diffusion dynamics in crystalline domains alone, the excitation wavelength is carefully selected so as to excite crystalline domains selectively. More specifically, P3HT crystalline domains can be selectively excited by the laser excitation at the absorption band-edge of P3HT. The diffusion dynamics of singlet excitons can be discussed by analyzing singlet–singlet annihilation that is a diffusion-limited exciton quenching.[9,12,15,17,22,27,28,36–39] In order to discuss the time dependence of the exciton diffusion dynamics in detail, the singlet–singlet annihilation over the wide temporal range from pico- to nanoseconds was measured. On the basis of these careful analyses, the diffusion coefficient and diffusion length of singlet excitons in P3HT crystalline domains are evaluated, and further discusses the dimensionality of the exciton diffusion.

6.2. Results

6.2.1. Absorption and Fluorescence Spectra. As shown in Figure 6-1, P3HT films exhibit a characteristic absorption shoulder at around 600 nm, which is attributable to the absorption band of crystalline P3HT. The absorption shoulder is more pronounced for the P3HT film prepared from chlorobenzene than that from chloroform, suggesting that the former film has higher crystallinity than the latter one. This is because chlorobenzene (b.p. 131.7 °C) would be more slowly evaporated during the spincoating and hence promote the crystallization of P3HT more effectively than

chloroform (b.p. 61.2 °C). As shown in Figure 6-1, the characteristic vibronic band structures can be well simulated by weakly interacting *H*-aggregate model.[40–42] The gray lines in the figure represent the absorption spectra of crystalline P3HT simulated with each vibronic band. The difference between the measured and simulated spectra is attributed to the absorption of amorphous P3HT in the film. From the ratio of the crystalline and amorphous absorption bands, the crystallinity of the P3HT films was evaluated to be 64% for the P3HT film prepared from chlorobenzene and 46% for the P3HT film prepared from chloroform (details are described in the Appendix).[42] In addition, the difference in the vibronic band structures suggests that crystalline structures are more ordered in P3HT-H than in P3HT-L (details are described in the Appendix). Hereafter, these P3HT films are abbreviated as P3HT-H and P3HT-L, where H and L represent higher (64%) and lower (46%) crystallinity, respectively. In AFM images of the P3HT film, crystalline fibrils with ~100 nm length were observed (data is shown in Appendix). This is consistent with the crystalline structures of P3HT films reported previously.[29–32]

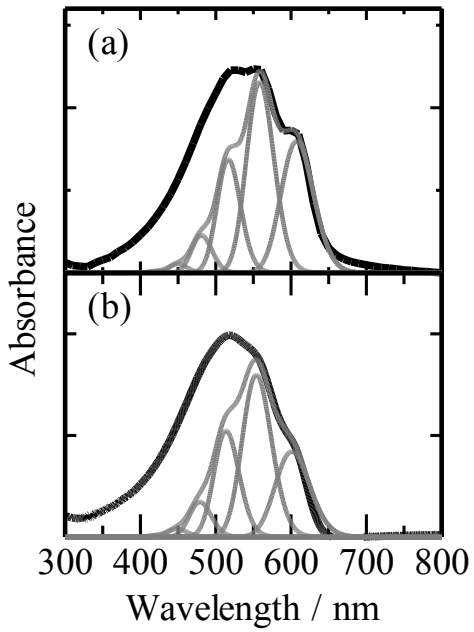

Figure 6-1. Absorption spectra of (a) P3HT-H and (b) P3HT-L films. The black lines represent the absorption spectra measured. The gray lines represent the absorption spectra of crystalline P3HT simulated by the weakly interacting *H*-aggregate model.

Figure 6-2 shows the fluorescence spectra and fluorescence decay of the two P3HT films. According to the weakly interacting *H*-aggregate model, the intensity ratio of the 0–0 to the 0–1 bands decreases with a higher structural order of crystalline domains.[43] As shown in Figure 6-2a, the 0–0 emission intensity of P3HT-H was lower than that of P3HT-L, suggesting that crystalline structures are more ordered in P3HT-H than in P3HT-L. This is consistent with the absorption spectra as mentioned above. Figure 6-2b shows the fluorescence decay of P3HT films measured by the time-correlated single-photon-counting (TCSPC) method. The fluorescence decays were fitted by a single exponential function with a lifetime of 480 ps for P3HT-H and 600 ps for P3HT-L. The fluorescence lifetime of 600 ps for P3HT-L is in good agreement with the previous report.[28] The slightly shorter lifetime of 480 ps may be due to the higher crystallinity of the P3HT-H film.

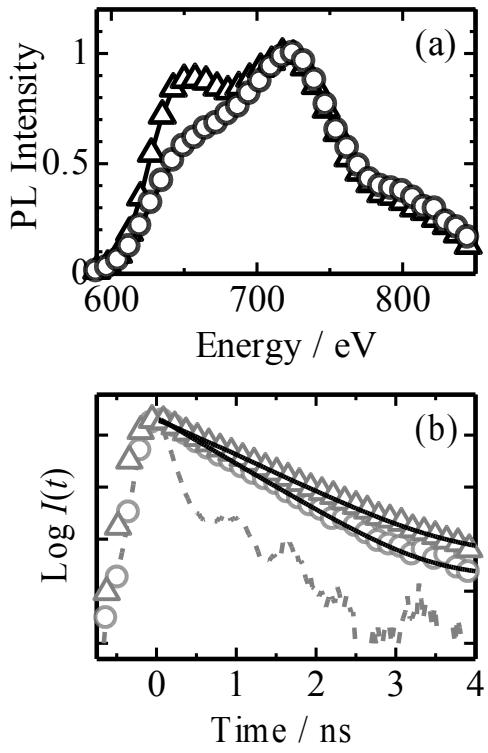

Figure 6-2. (a) Fluorescence spectra of P3HT-H (open circles) and P3HT-L (open triangles) films normalized at the 0–1 transition. (b) Fluorescence decay curves of P3HT-H (open circles) and P3HT-L (open triangles) films. The gray broken line is the instrument response function of the TCSPC measurement. The detection wavelength was 700 nm. The black lines represent best fitting curves with an exponential function.

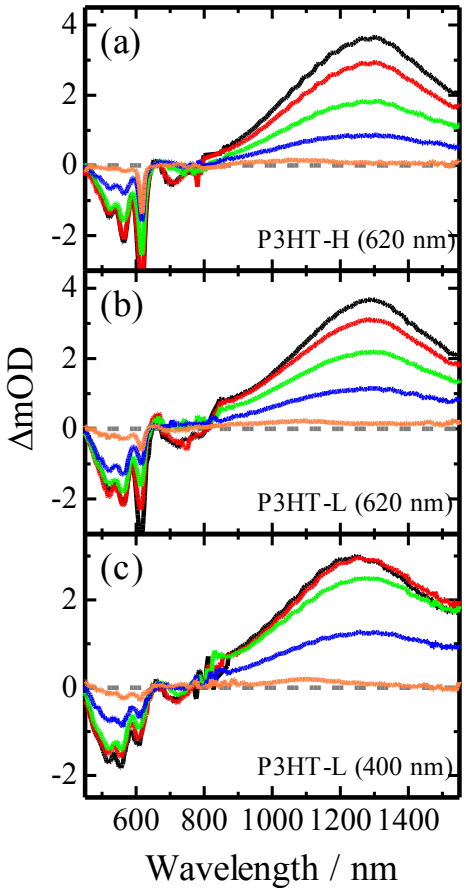

Figure 6-3. Transient absorption spectra of P3HT films measured at 0, 1, 10, 100, and 1000 ps after the laser excitation from top to bottom. The excitation wavelength (fluence) was (a), (b) 620 nm (2.7 μJ cm^{-2}) and (c) 400 nm (5.7 μJ cm^{-2}).

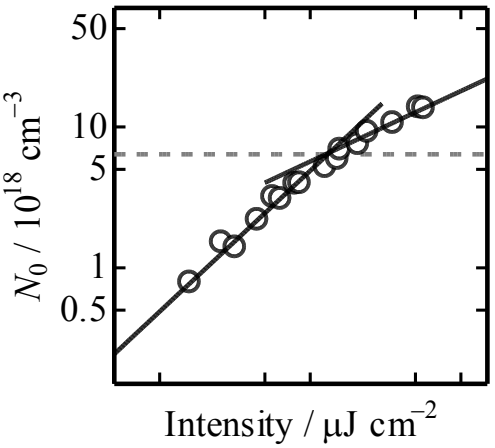

Figure 6-4. Log–log plots of the initial density of singlet excitons in P3HT-H films against the excitation intensity at 620 nm. The solid lines represent fitting curves with a power-law equation: $\Delta OD = I^m$. The broken line represents a threshold point from linear to non-linear dependence of the transient signals.

6.2.2. Transient Absorption Measurements. Figure 6-3 shows the transient absorption spectra of P3HT films measured from 0 ps to 1 ns after the laser excitation at 620 nm (absorption of P3HT crystalline domains) and at 400 nm (absorption of P3HT disordered domains). Upon the photoexcitation of P3HT films at 620 nm, as shown in the panels of (a) and (b), a broad absorption band was observed at around 1300 nm immediately after the laser excitation. This band is ascribed to singlet excitons as reported previously.[6,44,45] Interestingly, the peak wavelength was identical and no peak shift was observed over the whole time range measured regardless of the different crystallinity between P3HT-H and P3HT-L films. These findings suggest that the electronic properties of singlet excitons are rather insensitive to the crystallinity. Upon the photoexcitation of P3HT films at 400 nm, as shown in the panel (c), a broad absorption band was observed at around 1200 nm immediately after the laser excitation and then red-shifted to 1300 nm on a time scale of picoseconds. The peak shift observed suggests that singlet excitons generated in disordered domains migrate and/or relax to ordered crystalline domains. In summary, the 620-nm excitation can selectively excite P3HT ordered crystalline domains and the 400-nm excitation mainly excites disordered domains rather than ordered crystalline domains. In other words, the band-edge

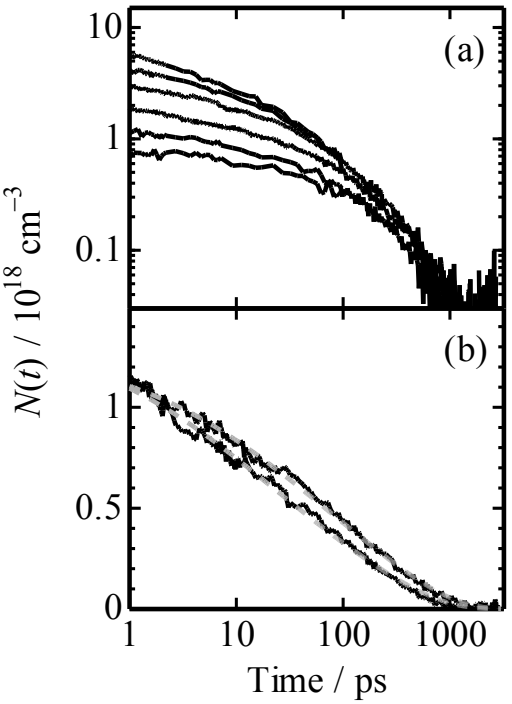

Figure 6-5. (a) Excitation-intensity dependence of singlet exciton decay of P3HT-H film measured at 1400 nm. The excitation intensity was varied over 1.6, 2.7, 5.7, 8.0, 15.3, and 35.7 μJ cm^{-2} from bottom to top. (b) Singlet exciton decay of (upper) P3HT-L and (lower) P3HT-H films measured at 1400 nm. The excitation wavelength (fluence) was 620 nm (2.7 μJ cm^{-2}). The broken lines represent the fitting curves with the 1D exciton diffusion model.

excitation at 620 nm is of particular importance for studying singlet excitons in P3HT crystalline domains as will be discussed later.

In order to estimate the effective interaction radii of singlet excitons generated in P3HT crystalline domains, the initial transient signal at 0 ps after the laser excitation at 620 nm under different intensities was measured. For the quantitative discussion, the initial transient signal ΔOD(0) was converted into the exciton density N_0 (details are described in the Appendix). Figure 6-4 shows log–log plots of the initial density of the singlet exciton observed for the P3HT-H film against different excitation intensities. Under lower excitation intensities, the initial density linearly increased with increasing excitation intensity and hence well fitted by a power-law equation of $N_0 \propto I^m$ with a slope of $m \approx 1$. Under higher excitation intensities, on the other hand, the slope was as low as ~0.5, suggesting that there is a bimolecular deactivation pathway of singlet excitons such as singlet–

singlet annihilation even on a short duration within the excitation laser pulse width (<100 fs). Similar intensity dependence was observed for P3HT-L films (data is not shown). From the threshold intensity, the effective interaction radius of singlet excitons was estimated to be 3.4 nm for P3HT-H and 3.3 nm for P3HT-L films. Note that singlet excitons are assumed as a sphere for the estimation.

Figure 6-5 shows the time evolution of the singlet exciton density in P3HT films. As shown in the panel (a), the exciton density decayed exponentially with a time constant of ~500 ps under lower singlet exciton densities. This is consistent with the exciton lifetime evaluated by the TCSPC method, suggesting monomolecular decay due to radiative and non-radiative deactivations. On the other hand, the exciton density decayed faster at early time stages under higher excitation intensities, suggesting bimolecular decay due to singlet–singlet annihilation based on the exciton diffusion. As shown in the panel (b), the decay dynamics of singlet excitons were slightly dependent on the crystallinity of P3HT films as will be discussed later.

6.3. Discussion

6.3.1. Excitation Wavelength Dependence. First, the dependence of the exciton diffusion dynamics on the excitation wavelength is discussed before moving onto the detailed discussion on the diffusion dynamics of singlet excitons in crystalline domains. As shown in Figure 6-3, the singlet exciton band and also the ground-state photobleaching were red-shifted with time from 1200 to 1300 nm ($\Delta E \approx 80$ meV) after the excitation at 400 nm. Such spectral shift is indicative of the fast downhill energy relaxation towards lower energy sites in the density of states (DOS). This is because singlet excitons at higher energy sites in the DOS are selectively generated by the excitation at 400 nm and hence can easily hop to more ordered sites. After the downhill relaxation, singlet excitons can hop among neighboring sites by thermal activation. In other words, the exciton diffusion dynamics induced by the 400-nm excitation does not only reflect singlet excitons in crystalline domains to be addressed in this study. In contrast, as shown in Figure 6-3, no spectral

shift was observed over the whole time range measured after the band-edge excitation at 620 nm. This is because singlet excitons at around the bottom in the DOS are selectively generated by the excitation at 620 nm and hence are not involved in the downhill relaxation. The author therefore focuses on the decay dynamics by the excitation at 620 nm in order to discuss the exciton diffusion in crystalline domains.

6.3.2. Singlet–Singlet Annihilation Model. The rate equation for the singlet exciton decay can be described by Eq. 6-1

$$\frac{\mathrm{d}N(t)}{\mathrm{d}t} = -\frac{N(t)}{\tau} - f\gamma(t)N(t)^2 \qquad (6\text{-}1)$$

where $N(t)$ is the exciton density at a delay time t after the laser excitation, τ is the fluorescence lifetime due to the radiative and non-radiative monomolecular deactivations and $\gamma(t)$ is the bimolecular decay rate due to the singlet–singlet annihilation. In the following analysis, τ was fixed to 480 ps for P3HT-H and 600 ps for P3HT-L evaluated by the TCSPC measurement. The annihilation rate $\gamma(t)$ has been reported to be both time-dependent[28,37,39,46,47] and time-independent[22,27,36,48] for conjugated polymers. The factor f depends on the exciton dynamics after the annihilation. Here, the singlet–singlet annihilation is considered as $S_1 + S_1 \rightarrow S_n + S_0$ where S_0 is the ground state, S_1 is the lowest excited singlet state, and S_n is a higher excited singlet state. The factor f would be unity if no exciton remains after the annihilation (for example, S_n is converted into polaron or triplet excitons before the vibrational relaxation to S_1). On the other hand, the factor f would be 1/2 if the exciton annihilation leaves one exciton ($S_1 + S_1 \rightarrow S_n + S_0 \rightarrow S_1 + S_0$ + phonon). Although additional terms are sometimes added to the rate equation to account for other deactivation pathways such as singlet–triplet or singlet–polaron annihilation,[36,49,50] such reactions are negligible because of low generation yields of triplet excitons and polarons in P3HT pristine films.

The diffusion-limited bimolecular reaction rates significantly depend on the dimensionality of the system. In the three-dimensional (3D) diffusion, excitons diffuse randomly in all the directions with

an isotropic diffusion coefficient. The bimolecular reaction rate for the 3D system is given by Eq. 6-2[51]

$$\gamma_{3D}(t) = 8\pi DR\left(1 + \frac{R}{\sqrt{2\pi Dt}}\right) \tag{6-2}$$

where D is the isotropic diffusion coefficient and R is the effective interaction radius of singlet excitons. For a late time stage after $t >> R^2/(2\pi D)$, the annihilation rate can be expressed as the time-independent formula $\gamma_{3D} = 8\pi DR$ because the second term is negligible. In the 2D system such as molecular crystals, excitons diffuse only along the major two crystallographic directions. The bimolecular reaction rate is given by Eq. 6-3[52]

$$\gamma_{2D}(t) = \frac{8DR}{\pi}\int_0^\infty \exp(-Du^2t)\frac{du}{u[J_0^2(uR) + Y_0^2(uR)]} \tag{6-3}$$

where J_0 and Y_0 are the Bessel functions of the first and second kind and zero order, respectively. A table of values of the integral term in Eq. 6-3 has been published by Jarger et al.[53] Useful approximations for Eq. 6-3 are given by Eq. 6-4

$$\gamma_{2D}(t) \approx 4\pi DR\left(\frac{1}{2} + \frac{R}{\sqrt{2\pi Dt}}\right) \tag{6-4}$$

for small values of Dt/R^2, and by Eq. 6-5

$$\gamma_{2D}(t) \approx 4\pi DR\left(\ln\frac{8Dt}{R} - 2\gamma\right)^{-1} \tag{6-5}$$

for large values of Dt/R^2, where γ is the Euler's constant (0.57722$\cdots$). From Eqs. 6-4 and 6-5, a general trend of the time-dependent bimolecular rate for the 2D system can be deduced: the annihilation rate decreases with time as $t^{-\alpha}$ where α is 0.5 at an earlier time stage and $\alpha < 0.5$ at a later time stage. In the 1D system, the bimolecular reaction rate is given by Eq. 6-6.[54]

$$\gamma_{1D}(t) = 4\pi DR\frac{R}{\sqrt{2\pi Dt}} \tag{6-6}$$

For simplicity, Eq. 6-6 was modified from a typical rate equation as described in the Appendix. In summary, the bimolecular rate becomes time-independent for the 3D system and $t^{-\alpha}$ ($\alpha < 0.5$) dependent for the 2D system at larger t, and is consistently $t^{-0.5}$ dependent for the 1D system over the

all time domain. Thus, the dimensionality of the exciton diffusion dynamics can be discussed on the basis of the time dependence of the annihilation rate.

The annihilation rate can be directly extracted from experimental decay curves by the following procedure reported previously.[37,46] A new variable given by Eq. 6-7 is introduced.

$$Y(t) = \exp\left(-t/\tau\right) N(t)^{-1} \tag{6-7}$$

By substituting Eq. 6-1 into Eq. 6-7, a linearized differential equation is obtained.

$$\frac{\mathrm{d}Y(t)}{\mathrm{d}t} = f\gamma(t) \exp\left(-t/\tau\right) \tag{6-8}$$

Consequently, $\gamma(t)$ can be directly extracted from Eq. 6-8 with a fluorescence lifetime τ and a temporal differentiation of the variable $Y(t)$ fitted with a simple equation so that it can accurately reproduce the time evolution of Eq. 6-7. In this study, f = 1/2 is assumed because of the low generation yield of triplet excitons and polarons from S_n compared to the vibrational relaxation.[55] Thus, Eq. 6-1 is solved as follows:

$$N(t) = \frac{N_0 \exp(-t/\tau)}{1 + N_0 F(t)} \tag{6-9}$$

$$F(t) = \begin{cases} 4\pi DR\tau\{1 - \exp(-t/\tau)\} + 4\pi R^2 \sqrt{D\tau/2}\, \mathrm{erf}\left(\sqrt{t/\tau}\right) & \text{(3D)} \\ \pi DR\tau\{1 - \exp(-t/\tau)\} + 2\pi R^2 \sqrt{D\tau/2}\, \mathrm{erf}\left(\sqrt{t/\tau}\right) & \text{(2D)} \\ 2\pi R^2 \sqrt{D\tau/2}\, \mathrm{erf}\left(\sqrt{t/\tau}\right) & \text{(1D)} \end{cases} \tag{6-10}$$

where "erf" denotes the error functions defined as $\mathrm{erf}(t) = 2/\sqrt{\pi} \int_0^t \exp(-x^2)\mathrm{d}x$. Here $F(t)$ for the 2D system is solved from Eq. 6-4 and hence valid only for short time t.

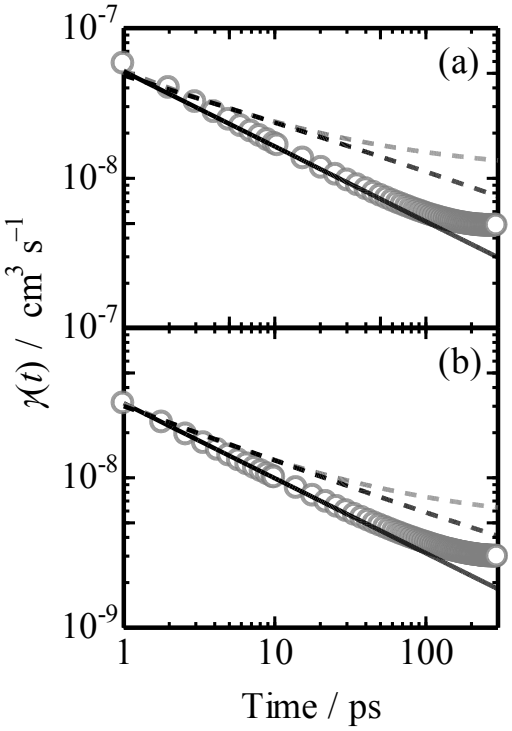

Figure 6-6. The extracted annihilation rates for (a) P3HT-H and (b) P3HT-L films excited at 620 nm by Eq. 6-7 and Eq. 6-8. The curve is calculated from 0 to 300 ps because of good signal-to-noise ratio in the transient absorption data on this time scale. The solid line represents the fitting curve using the 1D model. The broken lines represent the annihilation rate calculated by the 3D (gray) and 2D (black) models.

6.3.3. Time-Dependent Exciton Dynamics. This section deals with the origin of the time-dependent annihilation rate of singlet excitons formed in P3HT crystalline domains. As shown in Figure 6-6, the annihilation rate is not constant over the time range measured but exhibits almost $t^{-1/2}$ dependence for P3HT films. On the other hand, the annihilation rate in P3HT films has been reported to be both time-dependent[28] and time-independent[27]. As shown in Figure 6-6, the $t^{-1/2}$ dependence is so modest that the change in the annihilation rate is as small as less than one order of magnitude over the temporal change by one order of magnitude. Thus, it is of particular importance to measure the annihilation rate over a wide temporal range in order to discuss the time dependence in detail. In Ref. 27, the exciton dynamics is observed only for limited temporal range from 300 to 800 ps. In such a limited time range, the annihilation rate could be treated to be independent of time.

Indeed, the averaged annihilation rate in this limited time window is in good agreement with that reported in Ref. 27. On the other hand, the time-dependent annihilation rate has been reported over the temporal range from 100 ps to 1 ns in Ref. 28. However, the t^{-1} dependence reported in Ref. 28 is different from the $t^{-1/2}$ dependence observed in this study. As is discussed in the literature[28], the t^{-1} dependence is due to downhill relaxation in the energetic disorders in P3HT films. In contrast, the $t^{-1/2}$ dependence observed is not ascribed to the downhill relaxation in the energetic disorders because no spectral shift is observed by the laser excitation at the absorption edge of crystalline P3HT. Rather, the author ascribes the $t^{-1/2}$ dependence to inherent exciton dynamics in P3HT crystalline domains: as will discuss below it is ascribed to anisotropic exciton diffusion. This difference probably results from the difference in the excitation wavelength. Thus, it is concluded that ultrafast transient spectroscopy by the selective excitation is of particular importance to study the inherent exciton dynamics in crystalline domains of crystalline polymer films.

As described in the previous section, the $t^{-1/2}$ dependence over a wide temporal range can be best explained by the 1D exciton diffusion model. As shown in Figure 6-6, the experimental data are best fitted with the 1D exciton diffusion model over the wide temporal range measured. In contrast, there is a considerable discrepancy both in the 2D and 3D exciton diffusion models: they deviate from the $t^{-1/2}$ dependence at a longer time region. Therefore it is concluded that singlet excitons formed in P3HT crystalline domains mainly diffuse in the 1D motion. The $t^{-1/2}$-dependent exciton dynamics has been reported for many molecular crystals,[9,12,17] and is assigned to the 1D exciton diffusion in the crystallographic direction where the lattice spacing is shortest and hence the exciton coupling is largest. In analogy with molecular crystals, the 1D exciton diffusion in P3HT crystalline domains would be assigned to the exciton diffusion in the π-stacking direction because the π-stacking spacing has been reported to be as short as 0.38 nm in P3HT crystalline films.[29–32] Indeed, P3HT chains are likely to crystallize into 1D fibrils in the π-stacking direction.[29–32] However, the exciton coupling in crystalline polymers is more complicated than in molecular crystals because of the long delocalization in the main chain. In crystalline conjugated polymers, the point-dipole

Table 6-1. Fitting Parameters for Singlet Exciton Decay in P3HT Films

	γ / cm^3 s$^{-1/2}$	R / nm	D / cm^2 s^{-1}	τ / ps	L_D / nm
P3HT-H	$5.2 \times 10^{-14}\, t^{-1/2}$	3.4	7.9×10^{-3}	480	20
P3HT-L	$3.1 \times 10^{-14}\, t^{-1/2}$	3.3	3.3×10^{-3}	600	14

approximation is inappropriate for calculating the exciton coupling between adjacent chains. Recent quantum chemical calculations have shown that the exciton coupling between adjacent two delocalized chains decreases with increasing conjugation lengths that is longer than the separation distance between them.[56–59] In such case, the intrachain exciton coupling might be comparable to or larger than the interchain exciton coupling. Furthermore, as shown in Figure 6-6, a slight deviation from the $t^{-1/2}$ dependence at a later time stage is indicative of the contribution of the 2D exciton diffusion even though the diffusion coefficients are not the same in the two directions. At present, the limited data set presented herein is insufficient to provide unambiguous direction of the 1D exciton diffusion in P3HT crystalline domains. Further experiments to reveal the diffusion direction are currently in progress.

6.3.4. Exciton Diffusion Length. As summarized in Table 6-1, the diffusion coefficient D and the diffusion length $L_D = (D\tau)^{1/2}$ are evaluated to be 7.9×10^{-3} cm^2 s^{-1} and 20 nm for P3HT-H films and 3.3×10^{-3} cm^2 s^{-1} and 14 nm for P3HT-L films, respectively.[60,61] The larger diffusion coefficient and length in P3HT-H films are probably due to more ordered crystalline domains in P3HT-H films, which is consistent with the absorption and fluorescence spectra as mentioned before. Compared with previous reports on P3HT films, the diffusion length evaluated in this study (14–20 nm) is much longer than those evaluated by the exciton quenching in donor/acceptor bilayered films.[24–27] This is partly because disordered domains in the P3HT crystalline donor layer are not negligible for the exciton diffusion to the acceptor layer. In addition, this is partly due to anisotropic exciton diffusion in P3HT crystalline domains. Previous XRD studies have shown that P3HT crystalline is likely to be oriented with their side chains normal to the substrate and the main chain

backbone in the plane of the substrate.[29–32] This edge-on orientation is of disadvantage for the exciton diffusion to a quenching acceptor layer in donor/acceptor bilayered films because of the long hexyl chains. On the other hand, the diffusion length evaluated in this study (14–20 nm) is rather comparable to those evaluated by the singlet–singlet annihilation,[28] which is the same as the analysis in this study. As mentioned before, this is because the singlet–singlet annihilation in crystalline domains can be selectively observed by the selective excitation of the absorption band due to the crystal phase. Furthermore, the present estimate is also consistent with the theoretical prediction,[43] in which the diffusion length is estimated to be 15 nm from the dependence of Stokes shift on the number of chromophores in the aggregate. Note that the value of 15 nm is limited to diffusion along the π-stack and excluded the much less efficient migration normal to the stacking direction. In other words, the 1D exciton diffusion along the π-stack direction is theoretically suggested for P3HT crystalline domains. In conclusion, the author emphasizes again that the singlet–singlet annihilation analysis is more suitable for evaluating the exciton diffusion length in crystalline polymer films rather than the exciton quenching analysis for donor/acceptor bilayered films.

In comparison with other systems, the diffusion length in P3HT crystalline films is more than twice that reported for PPV amorphous films (5–7 nm).[18–23] This is primarily because the diffusion coefficient in P3HT crystalline films is one order of magnitude larger than that in PPV amorphous films. On the other hand, the diffusion length in P3HT crystalline films is less than half that reported for molecular crystals (typically 50–100 nm),[7,8,11–13,17] suggesting that there is still room to further improve the exciton diffusion length in P3HT. The longer diffusion length in molecular crystals is probably attributed to the higher structural order of the crystal, which has a critical impact on the exciton diffusion length in molecular crystals.[14,16] In defect-free molecular crystals, excitons would be delocalized over the entire crystal and hence diffuse coherently without trapping. In real crystals, excitons would be trapped at defect sites such as grain boundaries and chemical impurities, or self-trapped by lattice relaxation,[8] and hence the effective diffusion length is limited but still longer than that in crystalline polymers as mentioned above. For crystalline P3HT, a recent study has shown

that coherence length of the exciton along π-stacks is estimated to be only about three stacks, which corresponds to be as short as 1.1 nm. This is because there are significant disorders even in crystalline domains of P3HT films.[43] Thus, the exciton migration in P3HT films is due to incoherent hopping between limited coherent domains. For further improvements in the exciton diffusion length in crystalline polymer films, it would be of most importance to increase crystalline order.

6.4. Conclusions

In this chapter, the diffusion dynamics of singlet excitons in P3HT crystalline domains was studied by femtosecond transient absorption spectroscopy. By selective excitation of crystalline P3HT at the absorption edge, only singlet excitons in crystalline domains were observed exclusively. Immediately after the laser excitation, the exciton band was observed at around 1300 nm and was not shifted with time. This finding is indicative of no downhill relaxation in the energetic disorder. With increasing excitation intensity singlet excitons decayed faster, suggesting singlet–singlet annihilation. The annihilation rate of singlet excitons exhibited $t^{-1/2}$ dependence over the wide temporal range from 1 to 100 ps. It is concluded that the $t^{-1/2}$ dependence is due to 1D anisotropic exciton diffusion in P3HT crystalline domains rather than the downhill relaxation. From the detailed analysis of the annihilation, the exciton diffusion coefficient D and the diffusion length $L_D = (D\tau)^{1/2}$ are evaluated to be 7.9×10^{-3} cm^2 s^{-1} and 20 nm for P3HT-H films and 3.3×10^{-3} cm^2 s^{-1} and 14 nm for P3HT-L films, respectively. The larger diffusion coefficient and length in P3HT-H films are probably due to more ordered crystalline domains in P3HT-H films. The diffusion length evaluated in this study (14–20 nm) is much larger than those evaluated by the exciton quenching in donor/acceptor bilayered films. This is partly because disordered domains in the P3HT crystalline donor layer are not negligible for the exciton diffusion to the acceptor layer in bilayered films. In addition, this is partly due to anisotropic exciton diffusion in P3HT crystalline domains with edge-on orientation in the donor/acceptor bilayered films where excitons are likely to diffuse in the direction parallel to the quenching acceptor layer but hardly to the quenching layer because of the long hexyl

chains. On the other hand, the diffusion length evaluated in this study (14–20 nm) is rather comparable to those evaluated by the singlet–singlet annihilation because the exciton–exciton annihilation in crystalline domains can be selectively observed by the selective excitation of the absorption band due to the crystal phase. Thus, the author emphasizes that the exciton–exciton annihilation analysis is more suitable for evaluating the exciton diffusion length in crystalline polymer films rather than the exciton quenching analysis for donor/acceptor bilayered films. The diffusion length in P3HT crystalline films is more than twice that reported for PPV amorphous films (5–7 nm), primarily because the diffusion coefficient in P3HT crystalline films is one order of magnitude larger than that in PPV amorphous films. In contrast, the diffusion length in P3HT crystalline films is less than half that reported for molecular crystals (typically 50–100 nm), suggesting that there is still room to further improve the exciton diffusion length. For further improvement of the exciton diffusion length in crystalline polymer films, it would be most important to increase crystalline order. These findings provide in-depth understanding of singlet exciton diffusion in crystalline conjugated polymers.

6.5. Experimental Section

Sample Preparation. P3HT was purchased from Aldrich and used without further purification. P3HT films were prepared onto quartz substrate by spincoating from chlorobenzene or chloroform solution. The film thickness were about 70–100 nm.

Measurements. UV-visible absorption and photoluminescence spectra of P3HT films were measured with a UV-visible spectrophotometer (Hitachi, U-3500) and a fluorescence spectrophotometer (Horiba Jobin Yvon, FluoroLog-3) equipped with a calibrated iHR320 imaging detector, respectively. Photoluminescence decay was measured by the time-correlated single-photon-counting (TCSPC) method (Horiba Jobin Yvon, FluoroCube). The excitation and the detection wavelength were 470 and 700 nm, respectively. The total instrument response function is an FWHM of ca. 280 ps. A weak excitation power (~nJ cm^{-2}) was used in the measurement to prevent singlet–singlet annihilation.

Transient absorption data were collected with a pump and probe femtosecond transient spectroscopy system. This system consists of a transient absorption spectrometer (Ultrafast Systems, Helios) and a regenerative amplified Ti:sapphire laser (Spectra-Physics, Hurricane). The amplified Ti:sapphire laser provided 800 nm fundamental pulses at a repetition rate of 1 kHz with an energy of 0.9 mJ and a pulse width of 100 fs (FWHM), which were split into two optical beams with a beam splitter to generate pump and probe pulses. One fundamental beam was converted into pump pulses at 400 nm with a second harmonic generator (Spectra-Physics, TP-F) or 620 nm with an ultrafast optical parametric amplifier (Spectra-Physics, TOPAS). The other fundamental beam was converted into white light pulses employed as probe pulses in the wavelength region from 400 to 1700 nm. The pump pulses were modulated mechanically with a repetition rate of 500 Hz. The temporal evolution of the probe intensity was recorded with a CMOS linear sensor (Ultrafast Systems, SPEC-VIS) for the visible measurement and with an InGaAs linear diode array sensor (Ultrafast Systems, SPEC-NIR) for the near-IR measurement. Transient absorption spectra and decays were collected over the time range from −5 ps to 3 ns. Typically, 2500 laser shots were averaged on each delay

time to obtain a detectable absorbance change as small as ~10^{-4}. In order to cancel out orientation effects on the dynamics, the polarization direction of the linearly polarized probe pulse was set at a magic angle of 54.7 ° with respect to that of the pump pulse. The sample films were sealed in a quartz cuvette purged with N_2 at room temperature. Note that the transient absorption spectra and dynamics were highly reproducible even after the several times measurements. In other words, the laser irradiation had negligible effects on the sample degradation at least under this experimental condition.

6.6. Appendix

6.6.1. Estimation of Crystalline Absorption. As shown in Figure 6-1, the characteristic vibronic band structures can be well simulated by the weakly interacting *H*-aggregate model.[40,41] On the basis of this model, the ratio of the 0–0 and 0–1 peak absorbance is related to the free exciton bandwidth in aggregates *W* as follows:

$$\frac{Abs_{0-0}}{Abs_{0-1}} \approx \left(\frac{1 - 0.24\,W/E_{\mathrm{p}}}{1 + 0.073\,W/E_{\mathrm{p}}}\right)^2 \tag{6-A1}$$

where E_{p} is the main intramolecular vibration coupled to the electronic transition, typically C=C symmetry stretching energy ~180 meV, and Huang–Rhys factor is assumed to be unity. The crystalline absorption spectrum was determined using a modified Franck–Condon fit to the whole spectrum in Figure 6-1 by Eq. 6-A2[42]

$$Abs.\,(E) \propto \sum_m \left(\frac{e^{-S}S^m}{m!}\right)\left(1 - \frac{We^{-S}}{2E_p}\sum_{n\neq m}\frac{S^n}{n!\,(n-m)}\right)^2 \Gamma\left(E - \left(E_{0\leftarrow 0} + mE_p\right)\right) \tag{6-A2}$$

where *m* denotes the vibrational level and G_m is a constant factor according to $G_m = \sum_{n\neq m}\frac{S^m}{n!(n-m)}$ (in this analysis, it was calculated up to the 0–6 transition, which is enough to provide a precise result). Γ represents line shape functions of each vibronic transition. For simplicity, a Gaussian line shape with the same standard deviation σ was used. Therefore the standard deviation σ can be used as a disorder parameter for crystalline order. The gray lines in Figure 6-1 represent the absorption spectra of crystalline P3HT simulated with each vibronic band. The difference between measured and simulated spectra in higher energy region was attributed to the absorption of amorphous P3HT in the film. From the ratio of the crystalline and amorphous absorption bands, the crystallinity of the P3HT films was evaluated to be 64% for P3HT-H and 46% for P3HT-L film.[8] Disorder parameter σ for P3HT-H (70 meV) was smaller than that of P3HT-L (80 meV), indicating that crystalline structures are more ordered in P3HT-H than in P3HT-L.

From Figure 6-1, the free exciton bandwidth *W* was evaluated to be 100 meV for P3HT-H and 160 meV for P3HT-L. In the weak exciton coupling regime, which are typical characteristics of most

conjugated polymers, resonant exciton coupling (Coulomb coupling) between neighboring chromophores J is smaller than the vibrational relaxation energy where the free exciton bandwidth is expressed as $W = 4J$,[S4] therefore exciton coupling was estimated to be 25 for P3HT-H and 40 meV for P3HT-L. From the results of quantum chemical calculation given by Gierschner et al.,[58] an exciton coupling of 25 and 40 meV is equivalent to 30–35 and 20–25 interacting repeat units, respectively, which corresponds an interacting chain length of ~14 and ~10 nm, respectively. This is consistent with crystalline structures of P3HT films reported previously.[29–32]

6.6.2. AFM Measurement. Figure 6-A1 shows an AFM image of the P3HT-H film, which was measured with an atomic force microscope (Shimadzu, SPM-9600) in the phase mode. Crystalline fibrils with ~100 nm in length were observed on the surface of the P3HT-H film.

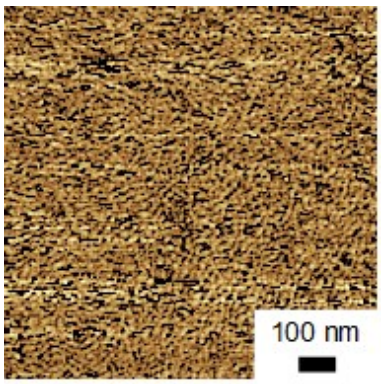

Figure 6-A1. AFM phase image of a P3HT-H film. The scale bar indicates 100 nm in length.

6.6.3. Estimation of Initial Exciton Density. As mentioned above, the transient absorption signal $\Delta\mathrm{OD}(t)$ should be converted into the exciton density $N(t)$. Here, a detailed method for the estimation of initial exciton density N_0 is described. First, the number of photons of the pump pulse within the probe beam spot is considered. Assuming the photon density distribution as a Gaussian function, the photon density z in an area element dxdy is described as

$$Z\mathrm{d}x\mathrm{d}y = A\exp\left(-\frac{x^2}{2\sigma^2}\right)\exp\left(-\frac{y^2}{2\sigma^2}\right)\mathrm{d}x\mathrm{d}y = A\,r\exp\left(-\frac{r^2}{2\sigma^2}\right)\mathrm{d}r\mathrm{d}\theta \qquad \text{(6-A3)}$$

where prefactor A is evaluated from the pump intensity measured and a pump spot radius of ~1 mm. An average excitation photon density within the probe spot N_{photon} (unit: cm^{-2}) is calculated as

$$N_{\mathrm{photon}} = \frac{1}{\pi R^2}\int_0^R\int_0^{2\pi} A\,r\exp\left(-\frac{r^2}{2\sigma^2}\right)\mathrm{d}r\mathrm{d}\theta = \frac{2A\sigma^2}{R^2}\left[1-\exp\left(-\frac{R^2}{2\sigma^2}\right)\right] \qquad \text{(6-A4)}$$

where R is the probe spot radius and is adjusted to be ~0.4 mm. From Eq. 6-A3 and 6-A4, the excitation intensity was converted into the average excitation photon density. The initial exciton density N_0 (unit: cm^{-3}) was calculated from the Beer–Lambert law as follows

$$N_0 = N_{\mathrm{photon}}(1-10^{-\mathrm{OD}})/l \qquad \text{(6-A5)}$$

where l is the film thickness. In general, crystalline polymer films consist of not only crystalline but also amorphous phases. Upon the photoexcitation of P3HT films at 620 nm, excitons were generated in only crystalline domain. In order to take into account the selective excitation of crystalline domains in films, N_0 was divided by the sample crystallinity estimated by steady-state absorption spectra as mentioned above.

6.6.4. Singlet–Singlet Annihilation Model. The modified annihilation rate equations were used as shown in Eq. 6-A6.

$$\gamma_{3D}(t) = 8\pi DR\left(1 + \frac{R}{\sqrt{2\pi Dt}}\right)$$
$$\gamma_{2D}(t) \approx 4\pi DR\left(\frac{1}{2} + \frac{R}{\sqrt{2\pi Dt}}\right) \quad \text{(6-A6)}$$
$$\gamma_{1D}(t) = 4\pi DR\frac{R}{\sqrt{2\pi Dt}}$$

Here the author briefly sketches the derivation of these equations. The derivation is based on the related problem of particle capture by an immobile quenching center. For the 3D diffusion model, a usual rate equation was used, therefore there is no need to provide further complement explanation. For the 2D diffusion model, the number density of excitons N at position r and time t was given by Eq. 6-A7.[52]

$$N(r,t) = \frac{2N_0}{\pi}\int_0^\infty \exp(-Du^2t)\frac{J_0(uR)Y_0(ur) - J_0(ur)Y_0(uR)}{J_0^2(uR) + Y_0^2(uR)}\frac{\mathrm{d}u}{u} \quad \text{(6-A7)}$$

where J_0 and Y_0 are Bessel functions of the first and second kind and zero order, respectively. Assuming a quencher shape as a cylinder with an interaction radius and height R, and an initially uniform exciton density N_0, the number of excitons passing through the curved surface of the cylinder in unit time is $2\pi DR^2(\partial N/\partial r)_{r=R}$. Therefore, the annihilation rate for the 2D system is given by

$$\begin{aligned}\gamma_{2D}(t)N_0 &= 2\pi DR^2\left(\frac{\partial N}{\partial r}\right)_{r=R} \\ &= \frac{8DRN_0}{\pi}\int_0^\infty exp(-Du^2t)\frac{\mathrm{d}u}{u[J_0^2(uR) + Y_0^2(uR)]}\end{aligned} \quad \text{(6-A8)}$$

$$\begin{aligned}\gamma_{2D}(t) &= \frac{8DR}{\pi}\int_0^\infty exp(-Du^2t)\frac{\mathrm{d}u}{u[J_0^2(uR) + Y_0^2(uR)]} \\ &= \frac{8DR}{\pi}I(\alpha)\end{aligned} \quad \text{(6-A9)}$$

A table of values of the integral term $I(\alpha)$ has been published by Jaeger et al.[11] A useful approximation is given by

$$I(\alpha) = \frac{1}{4}\pi^2\left\{(\pi\alpha)^{-\frac{1}{2}} + \frac{1}{2} - \frac{1}{4}\left(\frac{\alpha}{\pi}\right)^{\frac{1}{2}} + \frac{1}{8}\alpha - \cdots\right\} \quad (6\text{-A10})$$

for small values of α (α ≡ Dt/R^2), and the later terms in parenthesis in Eq. 6-A10 can be ignored to give

$$I(\alpha) \approx \frac{1}{4}\pi^2\left\{(\pi\alpha)^{-\frac{1}{2}} + \frac{1}{2}\right\} \quad (6\text{-A11})$$

Substituting Eq. 6-A11 into Eq. 6-A9 leads to $\gamma_{2D}(t) \approx 2\pi DR\left(\frac{1}{2} + \frac{R}{\sqrt{\pi Dt}}\right)$. Taking into account that quenchers in the exciton–exciton annihilation are also mobile excitons, therefore diffusion coefficient should be replaced by an effective diffusion coefficient $D_{\text{eff}} = D + D$, resulting in Eq. 6-A6. The value of $I(\alpha)$ for large values of α is given by

$$I(\alpha) = \frac{1}{4}\pi^2\left\{\frac{1}{y} - \frac{\gamma}{y^2} + \frac{\pi^3/6 - \gamma^2}{y^3} + \cdots\right\} \quad (6\text{-A12})$$

where γ is Euler's constant (0.57722⋯), and $y \equiv \ln 4\alpha - 2\gamma$. The later term in Eq. 6-A12 can also be ignored to give

$$I(\alpha) \approx \frac{1}{4}\pi^2(\ln 4\alpha - 2\gamma)^{-1} \quad (6\text{-A13})$$

resulting in the annihilation rate for large *t*.

$$\gamma_{2D}(t) = 2\pi DR(\ln 4\alpha - 2\gamma)^{-1} \quad (6\text{-A14})$$

For the 1D system, the number density of excitons *N* at position *x* and time *t* was given by Eq. 6-A15.[54]

$$N(x,t) = N_0\left[1 - \text{erfc}\left(\frac{x-R}{\sqrt{4Dt}}\right)\right] \quad (6\text{-A15})$$

where "erfc" denotes the complementary error function, which is defined as $\text{erfc}(t) = \frac{2}{\sqrt{\pi}}\int_x^\infty \exp(-x^2)\,dx$. Here the quencher was assumed as a cylinder with a radius and height *R*, while usually it was assumed as a cuboid. Note that it was assumed that diffusion direction is perpendicular to the base of the cylinder. In complete analogy to derivation for the 2D system, the number of excitons passing through the base of the cylinder in unit time is $2\pi DR^2(\partial N/\partial x)_{x=R}$. Therefore, the annihilation rate for the 1D system is given as Eq. 6-A6. Taking into account that

cylinder concentration n_0 is given by $n_0 = 1/\pi R^3$, substitution into Eq. 6-A6 results in the usual rate equation for the 1D system.

$$\gamma_{1D}(t) = \frac{1}{Rn_0}\sqrt{\frac{8D}{\pi t}} \tag{6-A16}$$

Figure 6-A2 shows the annihilation rate calculated by using above rate equations where diffusion coefficient and interaction radius are fixed to 5×10^{-3} cm^2 s^{-1} and 3 nm, respectively. In summary, the bimolecular rate becomes time-independent for the 3D system and $t^{-\alpha}$ ($\alpha < 0.5$) dependent for the 2D system at larger t, and is consistently $t^{-0.5}$ dependent for the 1D system over the all time domain.

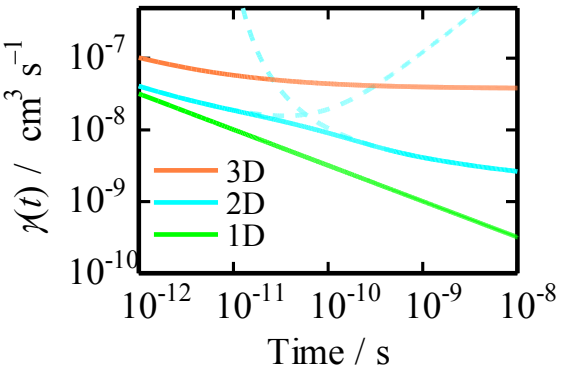

Figure 6-A2. Calculated annihilation rates by using the 3D (orange), 2D (blue), and 1D (green) diffusion models. The diffusion coefficient and interaction radius were fixed to 5×10^{-3} cm^2 s^{-1} and 3 nm, respectively. The broken and solid blue lines represent approximated annihilation rates based on Eq. 6-A6 and 6-A14, and smoothly connected curve, respectively.

6.6.3. Fitting Results for Singlet Exciton Decays. Figure 6-A3 shows the fitting results using the 3D, 2D, and 1D diffusion models from left to right. Clearly the 1D diffusion model gave the best fitting result.

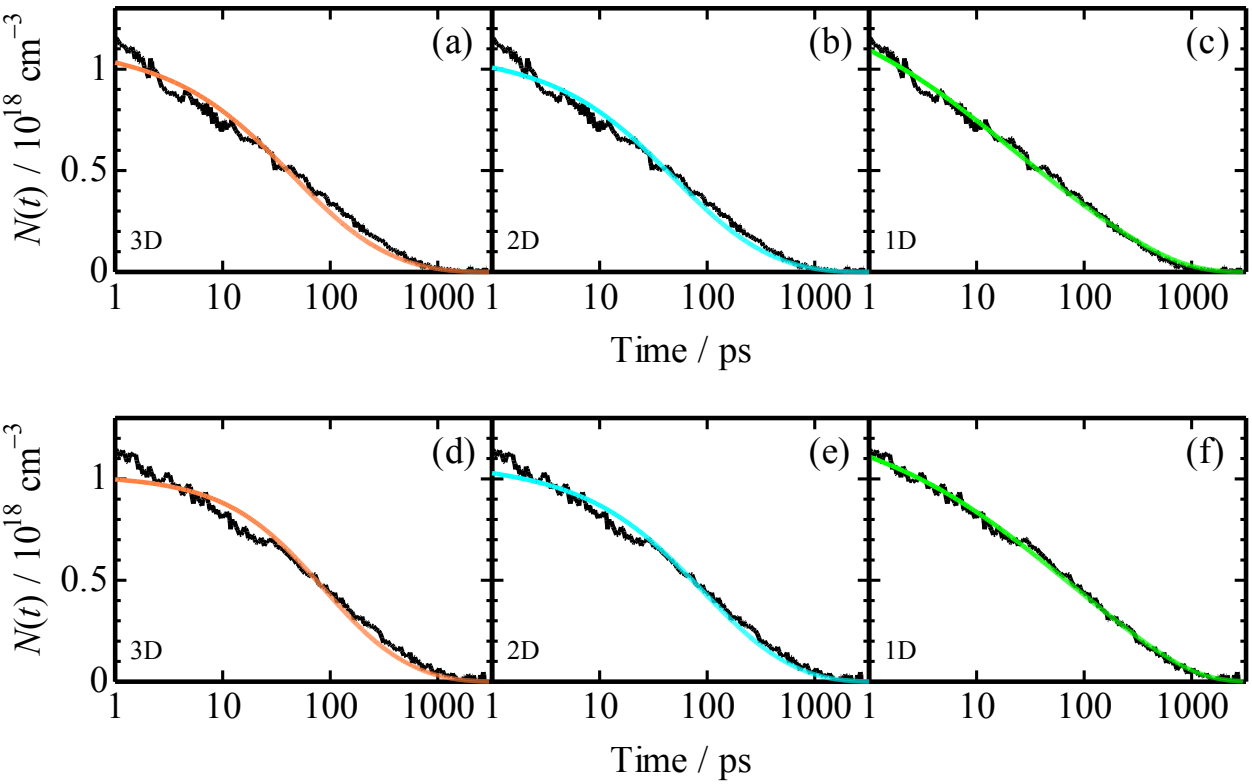

Figure 6-A3. Femtosecond transient absorption decays of (a–c) P3HT-H and (d–f) P3HT-L films excited at 620 nm (2.7 μJ cm^{-2}). The color lines represent best fitting curves by using the 3D (a, d), 2D (b, e), and 1D (c, f) diffusion models.

References

(1) Kippelen, B.; Brédas, J.-L. *Energy Environ. Sci.* **2009**, *2*, 251–261.

(2) Clarke, T. M.; Durrant, J. R. *Chem. Rev.* **2010**, *110*, 6736–6767.

(3) Deibel, C.; Dyakonov, V. *Rep. Prog. Phys.* **2010**, *73*, 096401.

(4) Heeger, A. J. *Chem. Soc. Rev.* **2010**, *39*, 2354–2371.

(5) Nelson, J. *Mater. Today* **2011**, *14*, 462–470.

(6) Ohkita, H.; Ito, S. *Polymer* **2011**, *52*, 4397–4417.

(7) Powell, R. C.; Soos, Z. D. *J. Lumin.* **1975**, *11*, 1–45.

(8) Pope, M.; Swenberg, C. E. *Electronic Processes in Organic Crystals and Polymers*; Oxford University Press: Oxford, U. K., 1999.

(9) Gulbinas, V.; Chachisvilis, M.; Valkunas, L.; Sundström, V. *J. Phys. Chem.* **1996**, *100*, 2213–2219.

(10) Donker, H.; van Hoek, A.; van Schaik, W.; Koehorst, R. B. M.; Yatskou, M. M.; Schaafsma, T. J. *J. Phys. Chem. B* **2005**, *109*, 17038–17046.

(11) Mani, A.; Schoonman, J.; Goossens, A. *J. Phys. Chem. B* **2005**, *109*, 4829–4836.

(12) Engel, E.; Leo, K.; Hoffmann, M. *Chem. Phys.* **2006**, *325*, 170–177.

(13) Kurrle, D.; Pflaum, J. *Appl. Phys. Lett.* **2008**, *92*, 133306.

(14) Huijser, A.; Savenije, T. J.; Meskers, S. C. J.; Vermeulen, M. J. W.; Siebbeles, L. D. A. *J. Am. Chem. Soc.* **2008**, *130*, 12496–12500.

(15) Yago, T.; Tamaki, Y.; Furube, A.; Katoh, R. *Phys. Chem. Chem. Phys.* **2008**, *10*, 4435–4441.

(16) Lunt, R. R.; Benziger, J. B.; Forrest, S. R. *Adv. Mater.* **2010**, *22*, 1233–1236.

(17) Marciniak, H.; Li, X.-Q.; Würthner, F.; Lochbrunner, S. *J. Phys. Chem. A* **2011**, *115*, 648–654.

(18) Markov, D. E.; Hummelen, J. C.; Blom, P. W. M. *Phys. Rev. B* **2005**, *72*, 045216.

(19) Markov, D. E.; Blom, P. W. M. *Phys. Rev. B* **2005**, *72*, 161401.

(20) Markov, D. E.; Blom, P. W. M. *Phys. Rev. B* **2006**, *74*, 085206.

(21) Scully, S. R.; McGehee, M. D. *J. Appl. Phys.* **2006**, *100*, 034907.

(22) Lewis, A. J.; Ruseckas, A.; Gaudin, O. P. M.; Webster, G. R.; Burn, P. L.; Samuel, I. D. W. *Org. Electron.* **2006**, *7*, 452–456.

(23) Mikhnenko, O. V.; Cordella, F.; Sieval, A. B.; Hummelen, J. C.; Blom, P. W. M.; Loi, M. A. *J. Phys. Chem. B* **2008**, *112*, 11601–11604.

(24) Kroeze, J. E.; Savenije, T. J.; Vermeulen, M. J. W.; Warman, J. M. *J. Phys. Chem. B* **2003**, *107*, 7696–7705.

(25) Goh, C.; Scully, S. R.; McGehee, M. D. *J. Appl. Phys.* **2007**, *101*, 114503.

(26) Huijser, A.; Savenije, T. J.; Shalav, A.; Siebbeles, L. D. A. *J. Appl. Phys.* **2008**, *104*, 034505.

(27) Shaw, P. E.; Ruseckas, A.; Samuel, I. D. W. *Adv. Matter.* **2008**, *20*, 3516–3520.

(28) Cook, S.; Liyuan, H.; Furube, A.; Katoh, R. *J. Phys. Chem. C* **2010**, *114*, 10962–10968.

(29) Grévin, B.; Rannou, R.; Payerne, R.; Pron, A.; Travers, J. P. *J. Chem. Phys.* **2003**, *118*, 7097–7102.

(30) Kim, Y.; Cook, S.; Tuladhar, S. M.; Choulis, S. A.; Nelson, J.; Durrant, J. R.; Bradley, D. D. C.; Giles, M.; Mcculloch, I.; Ha, C.-S.; Ree, M. *Nat. Mater.* **2006**, *5*, 197–203.

(31) Lim, J. A.; Liu, F.; Ferdous, S.; Muthukumar, M.; Briseno, A. L. *Mater. Today* **2010**, *13*, 14–24.

(32) Salleo, A.; Kline, R. J.; DeLongchamp, D. M.; Chabinyc, M. L. *Adv. Mater.* **2010**, *22*, 3812–3838.

(33) Padinger, F.; Rittberger, R. S.; Sariciftci, N. S. *Adv. Funct. Mater.* **2003**, *13*, 85–88.

(34) Li, G.; Shrotriya, V.; Huang, J.; Yao, Y.; Moriarty, T.; Emery, K.; Yang, Y. *Nat. Mater.* **2005**, *4*, 864–868.

(35) Jo, J.; Kim, S.-S.; Na, S.-I.; Yu, B.-K.; Kim, D.-Y. *Adv. Funct. Mater.* **2009**, *19*, 1–9.

(36) Zaushitsyn, Y.; Jespersen, K. G.; Valkunas, L.; Sundström, V.; Yartsev, A. *Phys. Rev. B* **2007**, *75*, 195201

(37) King, S. M.; Dai, D.; Rothe, C.; Monkman, A. P. *Phys. Rev. B* **2007**, *76*, 085204.

(38) Cook, S.; Furube, A.; Katoh, R.; Han, L. *Chem. Phys. Lett.* **2009**, *478*, 33–36.

(39) Shaw, P. E.; Ruseckas, A.; Peet, J.; Bazan, G. C.; Samuel, I. D. W. *Adv. Funct. Mater.* **2010**, *20*, 155–161.

(40) Spano, F. C. *J. Chem. Phys.* **2005**, *122*, 234701.

(41) Spano, F. C. *Chem. Phys.* **2006**, *325*, 22–35.

(42) Clark, J.; Chang, J.-F.; Spano, F. C.; Friend, R. H.; Silva, C. *Appl. Phys. Lett.* **2009**, *94*, 163306.

(43) Spano, F. C.; Clark, J.; Silva, C.; Friend, R. H. *J. Chem. Phys.* **2009**, *130*, 074904.

(44) Guo, J.; Ohkita, H.; Benten, H.; Ito, S. *J. Am. Chem. Soc.* **2009**, *131*, 16869–16880.

(45) Guo, J.; Ohkita, H.; Benten, H.; Ito, S. *J. Am. Chem. Soc.* **2010**, *132*, 6154–6164.

(46) Dogariu, A.; Vacar, D.; Heeger, A. J. *Phys. Rev. B* **1998**, *58*, 10218.

(47) Nguyen, T.-Q.; Martini, I. B.; Liu, J.; Schwartz, B. J. *J. Phys. Chem. B* **2000**, *104*, 237–255.

(48) Stevens, M. A.; Silva, C.; Russell, D. M.; Friend, R. H. *Phys. Rev. B* **2001**, *63*, 165213.

(49) Howard, I. A.; Hodgkiss, J. M.; Zhang, X.; Kirov, K. R.; Bronstein, H. A.; Williams, C. K.; Friend, R. H.; Westenhoff, S.; Greenham, N. C. *J. Am. Chem. Soc.* **2010**, *132*, 328–335.

(50) Hodgkiss, J. M.; Albert-Seifried, S.; Rao, A.; Barker, A. J.; Campbell, A. R.; Marsh, R. A.; Friend, R. H. *Adv. Funct. Mater.* **2012**, *22*, 1567–1577.

(51) Chandrasekhar, S. *Rev. Mod. Phys.* **1943**, *15*, 1–89.

(52) Naqvi, K. R. *Chem. Phys. Lett.* **1974**, *28*, 280–284.

(53) Jaeger, J. C.; Clarke, M. *Proc. Roy. Soc. Edinburgh A*, **1943**, *61*, 229–230.

(54) Torney, D. C.; McConnell, H. M. *J. Phys. Chem.* **1983**, *87*, 1941–1951.

(55) Although f can be set to 1/2 because only a small part of S_n states are converted into other transients as shown in Figure 6-2, the diffusion coefficients obtained in this study are their upper limits because f ranges between 1/2 and 1 to be accurate.

(56) Hennebicq, E.; Pourtois, G.; Scholes, G. D.; Herz, L. M.; Russell, D. M.; Silva, C.; Setayesh, S.; Grimsdale, A. C.; Müllen, K.; Brédas, J.-L.; Beljonne, D. *J. Am. Chem. Soc.* **2005**, *127*, 4744–4762.

(57) Barford, W. *J. Chem. Phys.* **2007**, *126*, 134905.

(58) Gierschner, J.; Huang, Y.-S.; Averbeke, B. V.; Cornil, J.; Friend, R. H.; Beljone, D. *J. Chem. Phys.* **2009**, *130*, 044105.

(59) Köse, M. E. *J. Phys. Chem. C* **2011**, *115*, 13076–13082.

(60) If *f* was assumed to unity, the diffusion coefficient and diffusion length would be estimated to be 2.0×10^{-3} cm^2 s^{-1} and 9.8 nm for P3HT-H and 0.8×10^{-3} cm^2 s^{-1} and 6.9 nm for P3HT-L, respectively, which correspond to the lower limit.

(61) These values are consistent with the results obtained by the analysis of the time evolution of the exciton density on the basis of the1D diffusion model as shown in the gray dashed lines in Figure 6-5b.

Summary

In this thesis, the photophysical dynamics relating to the excited state properties and transport in polymer systems has been studied in terms of polymer nanostructures. A summary of each chapter is described below.

In Part I (Chapter 2–4), the author focused his attention on the interchromophore interaction on a molecular scale to discuss the excited state properties in terms of the first/second order structures.

In Chapter 2, the author focused his attention on the chain conformation in ultrathin polymer films before moving on discussing photophysics in polymer systems. The conformation of a single poly(isobutyl methacrylate) (PiBMA) chain dispersed in microphase-separated structure of poly(isobutyl methacrylate)-*block*-poly(octadecyl methacrylate) (PiBMA-*b*-PODMA) monolayer was studied by scanning near-field optical microscopy (SNOM), which enables us to observe with a high spatial resolution beyond the diffraction limit of light. The conformation of the individual homo-PiBMA chains was quantitatively evaluated from the fluorescence intensity distribution. It was found that the homo-PiBMA chains are located almost at the center of the PiBMA domain. The homo-PiBMA chain was oriented depending on its location in the PiBMA domain. The homo-PiBMA chain located at the center of the PiBMA domain tended to be oriented in a direction parallel to the interface between the two microdomains. The homo-PiBMA chain located near the interface was oriented in a direction perpendicular to the interface.

In Chapter 3, solvent-polarity-induced formation dynamics of intramolecular excimer in dioxa[3.3](3,6)carbazolophane (CzOCz) was studied by time-resolved spectroscopic methods and computational calculations. In the ground state, the most stable conformer in CzOCz is the *anti*-conformation where two carbazole rings is aligned in anti-parallel. No other isomers was observed even the solution heated up to 150 °C, although three isomers were found by the molecular

mechanics calculation: the first is the *anti*-conformer, the second is the *syn*-conformer where two carbazole rings are stacked in the same direction, and the third is the *int*-conformer where two carbazole rings are rather aligned in the edge-to-face geometry. Because of the *anti*-conformation, the interchromophoric interaction in CzOCz is negligible in the ground state. Nonetheless, the intramolecular excimer in CzOCz was dynamically formed in an acetonitrile (MeCN) solution, indicating strong interchromophoric interaction and the isomerization from the *anti*- to *syn*-conformer in the excited state. The excimer formation in CzOCz was more efficient in polar solvents than in less polar solvents, suggesting the contribution of the charge transfer (CT) state to the excimer formation. The decrease in the potential barrier for the isomerization in the excited state is attributed to attractive molecular orbital interaction between two carbazole rings. The solvent-polarity-induced excimer formation is attributed to the CT character in the *int*-conformation originating from asymmetrical edge-to-face geometry.

In Chapter 4, triplet exciton dynamics was studied for two conjugated copolymers of fluorene with the aromatic amines, poly(9,9'-di-*n*-octylfluorene-*ran*-*N*,*N*'-bis(4-*n*-butylphenyl)-*N*,*N*'-diphenyl-1,4-benzenediamine) (F8-PDA) and poly(9,9'-di-*n*-octylfluorene-*ran*-*N*,*N*'-bis(4-*t*-butylphenyl)-*N*,*N*'-diphenyl-9,10-anthracenediamine) (F8-ADA) by transient absorption spectroscopy. On a time scale of nanoseconds, triplet exciton were formed through the intersystem crossing (ISC) from singlet excitons. The ISC quantum efficiency was estimated to be 0.34 for F8-PDA and <0.25 for F8-ADA. The ISC rate was estimated to be 2.0×10^8 s^{-1} for F8-PDA and $<2.2 \times 10^7$ s^{-1} for F8-ADA. The difference in the ISC rate and efficiency is attributed to the planarity of the chain conformation and energy difference between singlet and triplet excited states: a non-planar conformation and a small ΔE_{ST} would enhance the ISC rate. On a time scale of micro- to milliseconds, F8-PDA exhibited bimolecular triplet exciton decay due to triplet exciton–exciton annihilation, but the triplet–triplet annihilation was negligible in F8-ADA, indicating that triplet excitons can diffuse freely in F8-PDA while they are trapped at ADA units in F8-ADA. The difference in triplet exciton diffusion efficiency is discussed in terms of the energy level arraignment of triplet excited state of the fluorene

and aromatic amines: the triplet excited state energy of aromatic amines incorporated should be higher than that of polyfluorenes in order to achieve a large triplet exciton diffusion coefficient. On the basis of these results, the author provided a strategy for further improvement in the PLED efficiency.

In Part II (Chapter 5, 6), the author focused his attention on the dependence of the higher order structures of polymer materials on the excited state transport in nanostructured polymer systems.

In Chapter 5, the dynamics of singlet fission in poly(9,9'-di-*n*-octylfluorene) (PFO) films was studied by transient absorption spectroscopy. Under a high excitation intensity, triplet excitons were rapidly interconverted from singlet excitons on a picosecond time stage. From the excitation intensity dependence of the generation yield, the rapid triplet exciton formation in PFO films is attributed to singlet fission from a higher singlet excited state S_n formed by the singlet–singlet annihilation (singlet fusion followed by singlet fission). The triplet pair formation efficiency is about two times more efficient in amorphous PFO than in ordered β-PFO films because of a competitive relaxation pathway of the efficient charge generation in β-PFO films. On the other hand, the triplet pair dissociation efficiency is more efficient in β-PFO than in amorphous PFO films because of larger triplet exciton diffusion coefficient in ordered phase. As a result, the overall triplet generation yield was comparable in these films. For efficient singlet fission in conjugated polymers, the author proposes that low-bandgap crystalline polymers would be suitable for efficient singlet fission in conjugated polymers.

In Chapter 6, singlet exciton dynamics in crystalline domains of regioregular poly(3-hexylthiophene) (P3HT) films was observed by transient absorption spectroscopy. Upon the selective excitation of crystalline P3HT at the absorption edge, no peak shift of the singlet exciton band was observed, suggesting singlet exciton dynamics in relatively homogeneous P3HT crystalline domains without downhill relaxation in the energetic disorder. Even under such selective excitation conditions, the annihilation rate $\gamma(t)$ was still dependent on time: $\gamma(t) \propto t^{-1/2}$, which is attributed to

one-dimensional exciton diffusion in P3HT crystalline domains. From the annihilation rate, the singlet exciton diffusion coefficient D and exciton diffusion length L_D were evaluated to be 7.9×10^{-3} cm^2 s^{-1} and 20 nm, respectively, for the P3HT film with higher crystallinity and 3.3×10^{-3} cm^2 s^{-1} and 14 nm, respectively, for the P3HT film with lower crystallinity.

List of Publications

Chapter 2

"Conformation of Single Homopolymer Chain in Microphase-Separated Block Copolymer Monolayer Studied by Scanning Near-Field Optical Microscopy"

Tamai, Y.; Sekine, R.; Aoki, H.; Ito, S.

Macromolecules **2009**, *42*, 4224–4229.

Chapter 3

"Dynamical Excimer Formation in Rigid Carbazolophane via Charge Transfer State"

Tamai, Y.; Ohkita, H.; Shimada, J.; Benten, H.; Ito, S.; Yamanaka, S.; Hisada, K.; Tani, K, Kubono, K; Shinmyozu, T.

Submitted to J. Phys. Chem. A

Chapter 4

"Triplet Exciton Dynamics in Fluorene–Amine Copolymer Films"

Tamai, Y.; Ohkita, H.; Benten, H.; Ito, S.

Submitted to Chem. Mater.

Chapter 5

"Singlet Fission in Poly(9,9'-di-*n*-octylfluorene) Films"

Tamai, Y.; Ohkita, H.; Benten, H.; Ito, S.

Submitted to J. Phys. Chem. C

Chapter 6

"Selective Observation of Singlet Exciton Diffusion in Poly(3-hexylthiophene) Crystalline Domains"

Tamai, Y.; Matsuura, Y.; Ohkita, H.; Benten, H.; Ito, S.

Submitted to J. Am. Chem. Soc.

Other Publication

"Poly(methacrylate)s Labeled by Perylene Diimide: Synthesis and Applications in Single Chain Detection Studies"

Aoki, H.; Takahashi, T.; Tamai, Y.; Sekine, R.; Aoki, S.; Tani, K.; Ito, S.

Polym. J. **2009**, *41*, 778–783.

"Non-Diffusion Limited Singlet Exciton Annihilation in Fluorene–Amine Copolymer Films"

Tamai, Y.; Ohkita, H.; Benten, H.; Ito, S.

To be submitted.

Acknowledgements

The present thesis is based on the studies that the author and his co-workers have carried out at Department of Polymer Chemistry, Graduate School of Engineering, Kyoto University, Japan, from 2007 to 2013, under the guidance of Professor Shinzaburo Ito. The author sincerely expresses his gratitude to Professor Shinzaburo Ito for his kind guidance, valuable advices and heartful encouragement throughout this work, and for giving this opportunity to do a PhD's work in his Lab. The author is deeply and heartily grateful to Associate Professor Hideo Ohkita for his kind supports, advices, and continuous discussions throughout this work. So many ideas in this thesis were born from these fruitful discussions. The author is also indebted to Associate Professor Hiroyuki Aoki and Assistant Professor Hiroaki Benten for their valuable suggestions and discussions.

The author is sincerely grateful to Professor Kenji Hisada, Fiber Amenity Engineering Course, Graduate School of Engineering, University of Fukui, for his valuable suggestion and discussions on Chapter 3. The author is sincerely grateful to Dr. Jiro Shimada, researcher of Kyoto University, for his valuable support on computational studies in Chapter 3. The author would like to thank Professor Keita Tani, Division of Natural Sciences, Osaka Kyoiku University, for providing the valuable samples of CzOCz and CzOMe used in Chapter 3. The author would like to thank Sumitomo Chemical Co., Ltd. for providing the valuable samples of F8-F6, F8-PDA and F8-ADA used in Chapter 4.

The author is in acknowledgement of the Grobal COE program (International Center for Integrated Research and Advanced Education in Materials Science) from the Ministry of Education, Culture, Sports, Science, and Technology, Japan, JST PRESTO program (Photoenergy and Conversion Systems and Materials for the Next-Generation Solar Cells), and Research Fellowships of the Japan Society for the Promotion of Science for Young Scientists.

The author also thanks the previous and present members of Ito Lab. for their instruction, collaboration, and encouragement.

Finally, the author expresses his heartful thanks to his parents, Mr. Etsuro Tamai and Mrs. Setsue Tamai, his brother, Mr. Yuta Tamai, and his grandparents, Mr. Yoshio Tamai and Mrs. Takako Tamai, Mr. Shukichi Yamada and Mrs. Junko Yamada, for their constant financial support, hearty assistance and encouragement.

March 2013

Yasunari TAMAI